Precise Measurement of Neutron Decay Parameters

The $abBA$ Experiment

Beam Time Request to SNS FNPB Proposal Review Advisory Committee.

R. Alarcon and S. Balascuta

Arizona State University

S. Baeßler, E. Frlež and D. Počanić

University of Virginia

L. Barrón Palos

Universidad Nacional Autónoma de México

J.D. Bowman (Spokesman), T.V. Cianciolo, S.I. Penttilä, K.P. Rykaczewski, and G.R. Young

Oak Ridge National Laboratory

J.R. Calarco and F.W. Hersmann

University of New Hampshire

V. Cirigliano, A. Danagoulian, T. Ito, A. Klein, J. Ramsey and W.S. Wilburn (Spokesman)

Los Alamos National Laboratory

T.E. Chupp and M. Sharma

University of Michigan

C. Crawford

University of Kentucky

T.R. Gentile

National Institute of Standards and Technology

M. Gericke, A. Micherdzinska, S. Page

University of Manitoba

G.L. Greene and R.K. Grzywacz

University of Tennessee

V.Gudkov

University of South Carolina

G.L. Jones

Hamilton College

J. Martin

University of Winnipeg

P.N. Seo

Triangle Universities Nuclear Laboratory

November 9, 2007

Contents

1 Executive Summary

As the simplest nuclear beta decay, the free neutron provides an extremely attractive laboratory for the study of the charged-current sector of the weak interaction. Because free neutron decay is unencumbered by the many-nucleon effects present in all other nuclear decays, measurements of the parameters that describe neutron decay can be related to the fundamental weak couplings in a straightforward fashion. Within the framework of the Standard Model, neutron decay can be used to determine the weak vector coupling constant g_V in a fashion that is relatively free of theoretical uncertainties. The vector coupling constant g_V has been and continues to be an important theoretical "tie point" between many precision measurements in weak interaction physics ($0^+ \to 0^+$ decays, pion decay). In combination with measurements of the weak coupling constant in muon decay, g_V provides a value for V_{ud} which can be compared with high energy experiments in the strange sector to provide important information regarding the completeness of the three-family picture of the Standard Model through a test of the unitarity of the CKM matrix. Such a comparison provides a powerful and quite general test of the Standard Model. We note that while the experimental consistency among measurements of g_V *and* V_{ud} currently show reasonable consistency, significant inconsistencies have been quite common in the past. Reliable and redundant information from multiple systems is critical if we expect to use this system as a test of fundamental theories. It should be noted that neutron decay is the only system that offers the prospect of a significant improvement in our knowledge of g_V and in the direct determination of V_{ud}.

We propose to perform a measurement of the correlations in neutron decay employing a new method which provides a substantive advance over previous measurements. Unlike previous measurements which are capable of measuring only one correlation coefficient (such as A, the correlation between the neutron spin σ_n and the decay electron momentum $\vec{p}_e$), our experiment will provide a "complete set" of correlations including not only A, but also B (the correlation between the neutron spin $\vec{\sigma}_n$ and the decay neutrino momentum $\vec{p}_\nu$), a (the correlation between the neutrino momentum $\vec{p}_\nu$ and the decay electron momentum $\vec{p}_e$), and the electron energy spectral distortion term b, also known as the Fierz interference term.. Sensitivity estimates based on existing neutron source technology (the Spallation Neutron Source) indicate that we can expect up to an order of magnitude improvement in each of these coefficients and in the case of b, the first measurement ever.

In the Standard Model, the four correlations a, b, B, and A are highly covariant, depending on only one free parameter $\lambda = g_A/g_V$, the ratio of the axial over vector neutron form factors. If physics beyond the standard model is included, the relationship between these coefficients is more complex and depends upon the details of the "new" physics (For example, in the standard $V - A$ interaction, b is exactly zero; the inclusion of scalar and tensor coupling implies $b \neq 0$). One approach to the interpretation of the results of our proposed measurements is to analyze the set of four coefficients with and without the inclusion of new physics. In this approach the self consistency of the coefficients provides a probe for new physics.

Of course, this is a familiar approach that can be employed with any set of covariant data. The challenge, in the face of an inconsistency, is to determine if it truly arises from new physics, or simply reflects unknown systematic errors in the data.

The proposed measurements address this dilemma directly. Because all the measurements are done in the same apparatus, most of the important systematic effects affect all of the coefficients. However, the relative dependencies of the different coefficients on a given systematic effect are very different. More significantly, these different dependencies are well understood, calculable, and furthermore can be determined experimentally. Thus, this over-determined experimental set can be analyzed for systematic covariance to provide a powerful self-check for systematic effects. This is critical in neutron beta decay where the systematic effects are known to present a challenge.

The new experiment includes a number of novel features. Several of these address known problems in previous neutron decay correlation experiments.

- Neutrons will be polarized using a nuclear spin polarized ^{3}He transmission cell. (The use of pulsed neutrons with such a cell has been shown to provide an exceedingly robust determination of the neutron polarization.)
- Decay electrons and protons will be detected in coincidence. (Realistic tests have shown that this will significantly reduce backgrounds.)
- Both electrons and protons will be detected in the same silicon detectors. (The use of a strong magnetic field makes this a 4π detector for both electrons and protons.)
- Proton time of flight will be exploited to provide information about the axial component of the proton momentum. (This greatly enhances the experimental sensitivity to a and provides an important check on systematic effects.)
- The neutron decay volume is defined by magnetic fields. (The neutrons do not interact with any matter in the decay volume.)
- The decay particles (e and p) do not interact with apertures or windows. (They see only $\vec{E}$ and $\vec{B}$ fields and the silicon detectors.)

All of the technologies required for the proposed experiment have been demonstrated. With the exception of the silicon detectors, all components of the apparatus are either in hand, commercially available, or are a straightforward extension of existing technology. All of the silicon detector requirements have been demonstrated in commercial products. Their integration into a single device represents the only significant R&D in the project. Such integration is underway by commercial suppliers.

The experimental collaboration includes members with extensive experience in all of the technologies required for the proposed measurements. Many are acknowledged leaders in their field. The collaboration includes a combined experience of more than 100 person-years in fundamental neutron physics.

2 Present Status of the Electroweak Standard Model

The Standard Model of the electroweak interaction represents a triumph of modern physics. Its successes are wide ranging and well documented in literature. In particular, the radiative and loop corrections are so well controlled that precision of 0.1% is typical for a broad class of calculated observables. Furthermore, this theoretical accuracy is matched by the measurement precision in numerous experimental tests, providing accurate input for the theoretical predictions. These tests span a remarkable range of physical systems, energy and distance scales, from atomic parity violation measurements at the low end, to collider experiments at the high energy end.

The combination of experimental and theoretical precision gives the SM considerable predictive ability in probing the empirically untested sector, at present not accessible directly by the available means. This has meant, for example, that global fits to the measured electroweak observables including radiative corrections constrained the mass of the t quark below 200 GeV almost a decade before the experimental value, currently $m_t = 174.2 \pm 3.3$ GeV, was determined by direct measurement. At present similarly stringent limits have been set, for example, on the yet unobserved Higgs mass from global fits.

As successful as the SM is in describing the known electroweak phenomenology, it represents only a subset of a full theory capable of accounting for the apparently arbitrary set of the basic SM masses and couplings that are simply not addressed by the current (minimal) Standard Model. The need to find a broader theory encompassing the SM has been present from the outset, and has motivated much, if not most, of the effort in the field of elementary particle physics, spilling over into certain precision studies in nuclear and atomic physics. The proposed program of measurements fits into the broad effort to determine the precise limits of validity of the current SM, and thus to infer limits on the possible extensions of the SM.

2.1 Role of Neutron Beta Decay in Standard Model Tests

By far most of the constraints on the Standard Model parameters, as well as on the physics beyond the SM, come from high energy measurements, especially from collider experiments. In the past, however, precision measurements in neutron and nuclear beta decay have been used to constrain certain SM extensions in the charged-current sector with comparable or superior sensitivity. Examples include new beta decay interactions in left-right symmetric models, exotic fermion models, models with leptoquarks and extended Higgs sectors, and contact interactions [1].

This is not too surprising, since beta decay proceeds via an intermediate virtual state (W boson) of mass ~ 80 GeV, and so precision measurements of amplitudes with vector or axial vector character and/or searches for other amplitudes which can interfere with vector or axial vector interactions can reach sensitivities for interactions at and beyond the TeV scale. Indeed historically the unitarity test $V_{ud}^2 + V_{us}^2 + V_{ub}^2 = 1$ was the first important example in which radiative corrections to the weak interaction in the Standard Model (from $\gamma - Z$ and $\gamma - W$ vertex and box diagrams in this case) were experimentally tested [2], and this test was done before the W and Z bosons were produced directly in colliders.

A convenient point of departure for the discussion of the physics of neutron decay is the expression for the polarized neutron decay rate in the tree approximation (neglecting recoil corrections and radiative corrections) as a function of electron energy E_e, given by [3]

$$dW \propto \frac{1}{\tau_n} F(E_e) \left[1 + a\frac{\vec{p}_e \cdot \vec{p}_\nu}{E_e E_\nu} + b\frac{m_e}{E_e} + A\frac{\vec{\sigma}_n \cdot \vec{p}_e}{E_e} + B\frac{\vec{\sigma}_n \cdot \vec{p}_\nu}{E_\nu} \right], \tag{1}$$

where $\vec{p}_e$ and $\vec{p}_\nu$ are the outgoing electron and neutrino momenta, $\vec{\sigma}_n$ is the neutron spin, and E_ν is the neutrino energy. $F(E_e)$ in the familiar beta energy spectrum. The correlation coefficients A, B, a, and b (as well as the neutron lifetime τ_n) are experimentally accessible quantities. In the standard model framework of a pure $V - A$ weak interaction, the experimental quantities are related to the vector and axial vector coupling constants G_V and G_A, respectively, by the following relationships:

$$
\begin{aligned}
a &= \frac{1-\lambda^2}{1+3\lambda^2}, && (2)\\
b &= 0, && (3)\\
A &= -2\frac{\lambda^2-\lambda}{1+3\lambda^2}, && (4)\\
B &= 2\frac{\lambda^2+\lambda}{1+3\lambda^2}, && (5)
\end{aligned}
$$

where $\lambda = g_A/g_V$ is the ratio of the axial vector and vector neutron form factors. Due to the low momentum transfer in neutron decay, the form factors are equal to the coupling constants, i.e., $\lambda = g_A(q=0)/g_V(q=0) = G_A/G_V$. Because the neutron lifetime depends on a linearly independent combination of g_A and g_V, a determination of λ and τ_n provide the means to extract g_A and g_V separately.

Since the coefficients a, b, B, and A depend only on λ, they provide a highly redundant data set. Thus the internal consistency of these data provides a test of the standard model. For example, for a pure $V-A$ interaction, the following relationships must hold exactly:

$$
\begin{aligned}
F_1 &= 1+A-B-a=0, && (6)\\
F_2 &= aB-A-A^2=0. && (7)
\end{aligned}
$$

We note that the current recommended values for a, A, and B yield:

$$
\begin{aligned}
F_1 &= 0.0047 \pm 0.0058, && (8)\\
F_2 &= 0.0025 \pm 0.0059, && (9)
\end{aligned}
$$

consistent with the Standard Model. The errors above are totally dominated by the uncertainty in a. A substantial improvement in the knowledge of all four coefficients thus directly offers a very interesting *new* test of the Standard Model.

A cornerstone of electroweak unification is conservation of the vector current. This implies a unique vector coupling constant G_V for all nuclear beta decays. By contrast, because the axial current is only partially conserved, G_A will vary from nuclei to nuclei. The methods for the determination of g_V ($0^+ \to 0^+$ nuclear decays, π decay, and neutron decay) depend upon quite different detailed nuclear and radiative corrections and thus a comparison between these methods provides a useful consistency test.

The vector coupling constant, G_V, can be connected to the fundamental Fermi coupling constant $G_V = V_{ud}G_F$ where V_{ud} is the first element of the Cabbibo-Kobayashi-Maskawa (CKM) quark mixing matrix [2]. Because G_F is well known from muon decay, a measurement of G_V directly provides a determination of V_{ud}. Such a determination can be combined with measurements of V_{us} and V_{ub} to provide a sensitive test of the unitarity of the CKM matrix. Because $|V_{ud}| > |V_{us}| >> |V_{ub}|$, the uncertainty in the unitarity sum $\Delta = 1 - V_{ud}^2 - V_{us}^2 - V_{ub}^2$ is dominated by the uncertainty in V_{ud}. The unitarity of the CKM matrix is central to the Standard Model since it preserves the concept of the universality of the weak interaction by allowing for a difference between the quark mass eigenstates and the quark weak interaction eigenstates. Finally, a precision determination of V_{ud} should be also viewed in the context of the overall effort in high energy physics at beauty and charm factories to determine with high precision all the parameters of the CKM matrix. With the recently-approved CLEO-c project, for example, it should be possible in the next few years to measure the CKM matrix element V_{cd} to $\sim 1\%$ accuracy if lattice gauge theory calculations of the required form factors can improve to match the precision of the data [4]. This would make possible an independent check of unitarity using the first column: $\Delta' = 1 - V_{ud}^2 - V_{cd}^2 - V_{td}^2$. Therefore a precision measurement of V_{ud} figures prominently in two separate checks of CKM unitarity. In addition, assuming unitarity condition of the upper row of the CKM matrix in the Wolfenstein parametrization, a precise determination of V_{ud} can be used to infer the Wolfenstein parameter $\lambda_W = V_{us}$, which is needed for the tests of the unitarity triangles at B factories. A violation of unitarity might result from right-handed currents, from other non-standard couplings, from coupling to additional quark generations, from supersymmetry, and in any case it requires new physics.

Currently the measurements of λ in neutron decay with the smallest quoted errors come from measurements of the polarized neutron beta asymmetry A. Unfortunately the measurements of A with the lowest quoted errors are in disagreement [5] with $\chi^2 = 10.5$ for four degrees of freedom. The origin of this discrepancy is unknown. We do note, however, that some of these measurements have undergone significant *post factum* adjustments to account for imperfect knowledge of the neutron polarization.

The 2006 Particle Data Group recommended value for $V_{ud} = 0.97377 \pm 0.00027$ is dominated by data from $0^+ \to 0^+$ nuclear decays [6] . When combined with the recommended values for V_{us} and V_{ub}, V_{ud} provides a unitarity sum on the first row of the CKM matrix. This gives:

$$\Delta = 1 - V_{ud}^2 - V_{us}^2 - V_{ub}^2 = 0.0008 \pm 0.0011 \qquad (10)$$

It was shown recently [7, 8] that observation of a deviation from unitarity could be evidence of contributions from SUSY models through radiative corrections, both with and without R-parity violation. This fact could lead to improved constraints on SUSY models using data from the precise measurement of neutron decay. Since similar contributions from SUSY will also modify the weak charge for parity violating neutral current processes [7, 9], it could relate results of neutron decay experiment and the study of parity violation in lepton scattering experiments at the Thomas Jefferson National Accelerator Facility, and make them complementary for the low energy SUSY analysis. Moreover, the possible constrains on SUSY with R-parity violation would have important implications for the validity of SUSY for the explanation of the origin of dark matter (see [10] and references therein).

We note that while the sum in Equation 10 is dominated by V_{ud}^2 the contribution of V_{us}^2 is significant. Recently the currently accepted value of V_{us} and its quoted uncertainty have been put in question by the findings of the BNL E865 experiment which has obtained a value of the K_{e3}^+ branching ratio 2.3σ higher than the old measurements. This result alone would suffice to bring the value of Δ in line with zero. Efforts are underway to clarify this situation through new analyses and measurements from KLOE, CMD-2 and NA48.

Notwithstanding the current level of agreement between different methods for the determination of g_V, or the currently "fashionable" theoretical notions that are thought to be tested by the universality of the vector current, a robust and accurate determination of g_V will remain an important parameter in our understanding of the charged current weak interaction. The neutron system provides a unique opportunity for a significant improvement in our knowledge of g_V.

Perhaps more importantly, the different coefficients have greatly different sensitivities both to the possible signals from new physics [11] as well as to systematic effects. For example, measurement of A or B requires knowledge of the neutron polarization while measurement of a or b does not. Similarly, the measurement of A or a requires knowledge of the beta energy while that of B does not. This differing sensitivity provides a very powerful tool for the identification and elimination of systematic effects. A consistency among a complete set of correlation coefficients, taken with the same experimental apparatus, will provide a compelling case that the resulting value for λ is credible. Given the long standing problems encountered in measurements of A, we believe this approach to have great value, particularly if one hopes to robustly confront theory at ever increasing levels of accuracy.

Measurements of angular coefficients a, A and B have been done before, however the Fierz interference term b has never been measured in neutron decay. b is equal to zero in the Standard Model. A nonzero b can be generated by interference of the vector current with a possible scalar current (b_F) or the axial vector current with a possible tensor current (b_{GT}). From $0^+ \to 0^+$ nuclear beta decay measurement Towner and Hardy have extracted an upper limit of $|b_F| \leq 0.0077$ (at 90% c.l.)[12], while Deutsch and Quin have extracted $b_{GT} = -0.0056(51)$, i.e., consistent with zero, from Gamow-Teller nuclear decay data [13].

A recent analysis of high-statistics radiative pion decay data $\pi^+ \to e^+\nu\gamma$ by the PIBETA collaboration has found a nonzero value for the pion tensor form factor, $F_T \simeq 0.0016(3)$ [14]. While this result may ultimately prove to be due to insufficiently accurate SM description of the decay (radiative corrections may be the first suspect), taken at face value it would imply a nonzero Fierz interference term in neutron decay, on the order of a few times 10^{-3}. Such a large tensor interaction would have to come either from leptoquarks or non-SM contact tensor interactions.

Clearly a measurement of b in neutron decay with the sensitivity of $\sim 10^{-3}$ would be of interest as a valuable Standard Model consistency check, as there are very few physical systems available for similar experimental tests.

2.2 Current Status of Neutron Experiments

Previously, coefficients a, A, and B have been measured to quoted precisions of $\delta a \sim 5 \times 10^{-3}$ ($\delta a/a \sim 5 \times 10^{-2}$) [15, 16], $\delta A = 7 \times 10^{-4}$ ($\delta A/A \sim 6 \times 10^{-3}$) [17], and $\delta B \sim 5 \times 10^{-3}$ ($\delta B/B \sim 5 \times 10^{-3}$) [18, 19]. Although a and A have similar sensitivities to λ, so far the extraction of λ comes mostly from the determination of A. (B is not sensitive to λ). There are currently four measurements of sufficient accuracy to enter significantly into a weighted average [17, 119, 118, 22]. As noted previously, these measurements are quite discrepant with $\chi^2 = 15.4$ for four degrees of freedom. Finally we note that no measurement of b in neutron decay has been attempted.

Appendix B provides a brief review of previous neutron decay correlation measurements (a, B, and A). In this section we will restrict our attention to two topics. The first concerns the determination of neutron polarization, which is critical in the determination of A. The second concerns the most recent and most accurate measurement, PERKEO II [17]. PERKEO II is particularly pertinent to the discussion at hand because: 1) PERKEO II represents the culmination of approximately 20 years of development and in some ways represents the limits of the current approach to the measurement of A, 2) there are important similarities between PERKEO II the proposed experiment, and 3) Many of the design features of the current experiment were specifically designed based on lessons learned from PERKEO II.

In PERKEO II, neutrons are polarized by mirror reflection from multilayer magnetic "supermirror" devices [23]. Such devices are simple to use, are highly reliable and can attain polarizations approaching 99%. However because the polarization mechanism is quite complex, the polarization cannot be accurately deduced from first principles. Additionally the polarization will vary across the neutron beam area and as a function of the beam divergence [1].

All measurements of A to date have determined the beam polarization in an auxiliary experiment. Such determinations face several challenges: 1) they must be highly accurate, 2) they must measure precisely the same beam phase space as the decay detector, and 3) the stability of the polarization system (and the neutron) source must be such that temporally separated measurements can be compared with sufficient accuracy. A great deal of effort has been devoted to these problems, and an extensive literature has developed [25, 26]. Nonetheless, the absolute determination of the neutron polarization remains one of the most important systematic issues in the determination of A and there is a suspicion that it may, in part, be responsible for the current discrepant situation. We note that one of the 4 measurements mentioned above [118] reflects an *a posteriori* correction for an error in the polarization of 1.4σ [117]. Prior to this correction, the discrepancy among measurements of A was even worse.

The PERKEO II experiment provides the most accurate determination of A. The essential features of the PERKEO II experiment were:

- The experiment employed cold neutrons from a steady state reactor (the ILL).
- The neutrons were polarized by passage through a multi-channel supermirror. Neutron polarization was perpendicular to the neutron beam direction. Neutron polarization was determined in an auxiliary experiment.
- The neutron spin was reversed periodically every 8 s [28] using a DC spin flipper. The flipper efficiency could be measured using the same method as the polarization measurement.
- The spectrometer consisted of two plastic scintillators oriented perpendicular to the neutron beam. Decays were detected as electron singles only.
- The decay volume was in a high magnetic field. Because the same magnetic field defined the neutron spin and the (2π) acceptance of each detector, no detailed knowledge of the detector geometry was required.
- Back scattered electrons were detected in the opposite detector. The original direction was determined by timing. Total energy was determined by summing.
- The magnetic field is quite uniform across the decay volume, and diverges toward the detectors. This geometry prevents the reversal of electron by "Θ-pinch" magnetic mirror effects.

PERKEO II was represented a very thorough and professional effort. While there is no reason whatsoever to question the result at the quoted error, one may, nonetheless, identify one issues which would be of considerable concern if a significantly lower error were required. Singles detection of electrons in a gamma concern. In fact, they had to subtract as much as 15% of the total detected counts as background. Finally we note that PERKEO II measured the coefficients, A B and C, but not b or a.

Another noteworthy project, which, is currently in progress will employ trapped ultra cold neutrons to determine A [29]. This experiment will employ a novel "super-thermal" UCN source and

[1] Note, however, since the last publication [17], the polarization has been greatly improved for the current PERKEO II, using a crossed geometry. See Ref [24].

employ the special characteristics of UCN to obtain a neutron polarization that approaches 100%. If this new method successfully provides an accurate determination of A, it will be particularly interesting because it will have somewhat different systematic corrections than previous measurements. The "UCNA" experiment is discussed in Appendix B.

3 Experimental Approach

The goal of the proposed work is the accurate measurement of *all* of the T-even neutron beta decay correlation coefficients (a, b, A, and B) that do not require the determination of the decay product polarization. A measurement of these coefficients in a *single apparatus* provides a high degree of redundancy which will allow multiple cross-checks of possible systematic effects as well as the extraction of theoretically important quantities (such as λ, or non-standard coupling constants) in a highly over-constrained way.

We propose to measure a, b, A, and B, using polarized neutrons from the Fundamental Neutron Physics Beamline(FnPB) at the SNS. This set of measurements will provide an extremely robust, and accurate determination of λ, as well as a range of new tests of physics beyond the Standard Model. Details of the expected sensitivities in these two phases is discussed in Section 4.

There are three main components to our apparatus: 1) the decay spectrometer, 2) the neutron polarizer, and 3) the neutron source.

Our experimental approach introduces two, quite new, techniques to the neutron decay arena. The first is a method of polarization (using nuclear spin polarized ^{3}He) that is based on well understood physics and allows the neutron polarization to be accurately determined *in situ* and without the need for any ancillary experiments. This directly addresses one of the historically most troublesome systematic effects in the measurement of A. The second new technique exploits the measurement of the proton drift time-of-flight to provide a rough determination of the axial component of the decay proton momentum. This information can be used to significantly improve the sensitivity of the determination of a, offering the prospect of a highly competitive value of λ that is totally independent of A and does not require polarized neutrons.

B can be obtained from the proton asymmetry at low electron energy, in which case the proton recoils against the neutrino. We also get a second determination of A from the proton asymmetry at high electron energy, where the proton recoils against the electron, but with a statistical error approximately $\sqrt{2}$ greater than from the electron asymmetry.

3.1 Decay Spectrometer

The decay spectrometer is a highly efficient 4π neutron decay detector sensitive to electron-proton coincidences. A schematic of the detector is shown in Figure 1 The essential components of the detector are:

The neutron beam passes through the decay volume of the spectrometer transverse to the magnetic field. In decay region there is a strong, homogeneous magnetic field ($\sim$ 4 T) and the decay particles drift along the magnetic field lines with cyclotron orbit radii that will depend on their energies but will typically be on the order of a millimeter. (Note that although the characteristic energies of the protons and electrons differ by three orders of magnitude, their momenta, and thus their cyclotron radii have comparable scales.) Because the decay region is well within the tubular HV electrode, the electric field in the decay region is very small ($<$ 1 mV/cm).

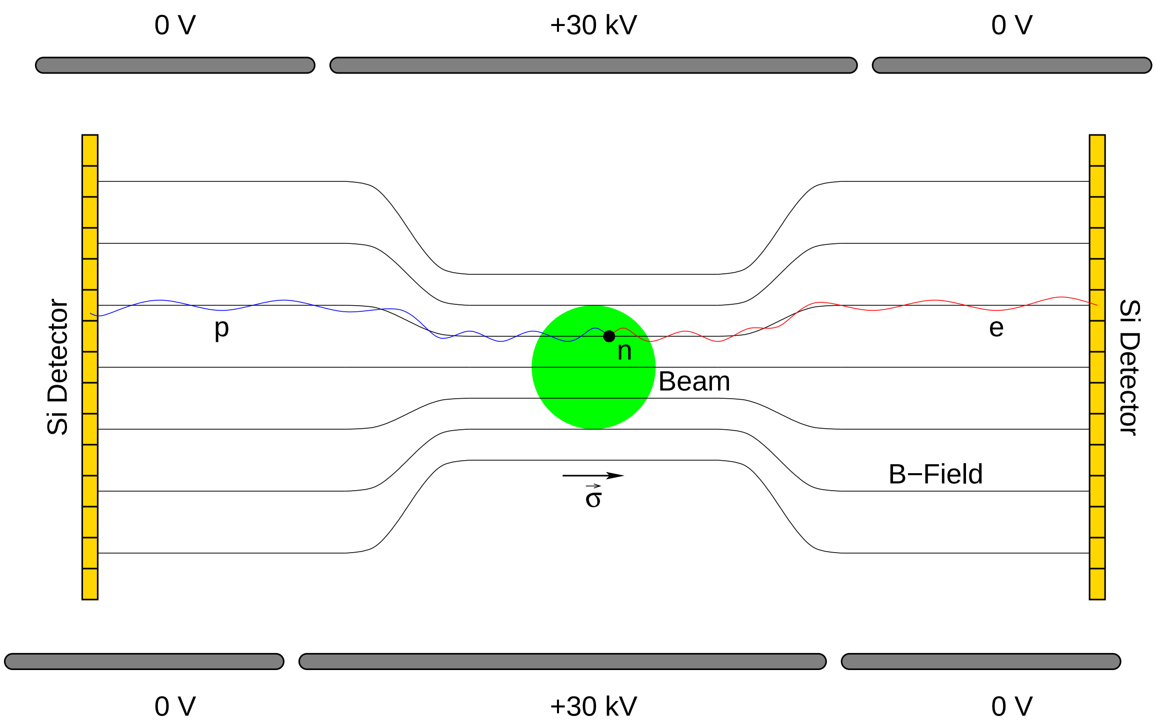

Figure 1: The conceptual design for the spectrometer showing the most important elements (not to scale). The beam direction is into the page.

As the particle drift from the decay region they pass through a region where the magnetic field decreases to 1 T. While this is a significant change in the magnetic of the field, the change, in the frame of the decay particle is slow compared with the cyclotron frequency so the charged particle transport is “adiabatic.” This implies that the cyclotron radii increases, particle’s transverse component of momentum is reduced, and the axial component is increased. This “longitudinalization” of the electron momentum greatly reduces the number of electrons that are Penning trapped and provides for 100% acceptance of electrons with total energy above 50keV. The “longitudinalization” of the electron momentum also implies that the electrons will hit the silicon detector more normal to the surface than they would otherwise. This reduces the probability of backscattering. We also note that this field expansion serves a critical function in the identification of back scattered events

Superconducting Magnet The decay volume (60 cm^3) is in a very uniform magnetic field of 4 T. The axis of the field determines the axis of neutron polarization as well as the projection axis for the decay particle detectors. Charged decay particles follow the magnetic field lines in helical orbits. Beyond the decay region, the field decreases to 1 T. This field decrease serves to longitudinalize the charged particle trajectories and thus significantly reduce the systematic effects of electron Penning trapping. This field change also serves as a Θ-pinch magnetic mirror to mitigate the effects of electron backscattering from the detectors. As shown in Figure 2, note that the Θ-pinch occurs before the electric field.

High Voltage Electrodes Because the maximum proton energy is only $\approx$ 750 eV, the decay volume is within a tubular electrode held at $\sim$ 30 kV. As the protons drift toward the end of the tube they are accelerated to 30keV and gain enough energy to be detected in a silicon detector. The aspect ratio of the tube is selected to insure that the E-field in the decay volume is sufficiently small so that systematic effects are not important. The neutrons enter the electrode through long tubular arms to allow a windowless system. A schematic of the fields of the magnet and the HV electrodes is presented in Figure 1.

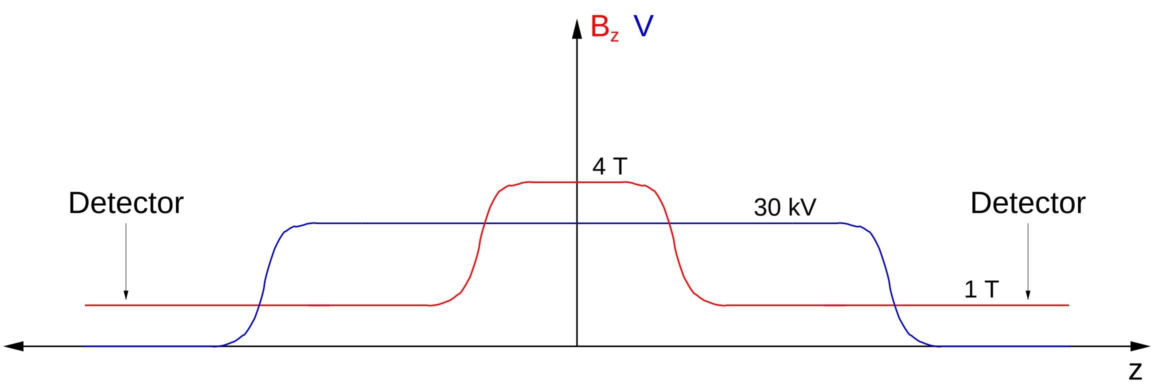

Figure 2: Configuration of the electric and magnetic fields along the spectrometer axis.

Silicon Detectors Electrons *and* protons are detected in the *same segmented silicon detectors.* There are no apertures and no secondary emission foils. The strong magnetic field insures that the only low energy particles that can strike the detector come from the decay volume which is at ultra-high-vacuum. Detection efficiency is essentially 4π. The detectors have an active thickness of ~ 2 mm which is sufficient to insure 100% electron energy deposit. The detectors will have thin entrance windows (dead layer) to insure the proton energy loss is small (~ 10 keV). The detectors will be ~ 10 cm diameter wafers with approximately 100 active pixels on each detector. Detectors and preamps will be cooled to cryogenic temperature and pixel area will be 0.7 cm^2. This will allow a trigger threshold of ~ 5 keV. We note that each of the above detector requirements has been individually met in prototypes and we are working with a supplier for the fabrication of the full detector.

Detector Electronics and DAQ The identification of backscattered electrons requires relatively fast timing (approximately few nanoseconds). Because the energy deposit of a single particle can span more than one pixel, we require detector electronics that can provide flexible event identification. Our DAQ will be based on a 12 bit, 100 MHz Digital Signal Processor. Proof-of-principle tests indicate that this system will have a time resolution of ~ 1 ns. Each channel has its own Field Programmable Gate Array with memory that corresponds to a depth of ~ 100 μs. This allows great flexibility in the choice of a specific data collection strategy. A prototype 16 channel module based on a 32 bit/33 MHz PCI bus has been ordered and is under construction by the vendor.

A decay event is identified by a delayed coincidence between a "fast" electron (TOF ≈ 10 ns) and a slow proton (TOF on the order of 10's of μs). Note that in the strong field, the decay particles drift along the magnetic field lines with cyclotron orbit radii (≤ 5 mm) that are smaller than the pixel size. This means that a true coincidence can only occur in the same pixel, in adjacent pixels, or in conjugate pixels on the two detectors. This greatly reduces the probability of a false coincidence. (In tests at NIST, using cold neutrons and a detector with a size comparable to a single pixel, it was observed that the coincidence background for such events was very small.) The apparatus provides a number of redundant methods by which this small background can be accurately measured. For each decay event, the following information can be determined (of course, for each, there are some corrections required for systematic effects, these are discussed in Section 4.2. As shown in Figure 2, the magnetic field expansion lies within the region where the electric potential is constant. After leaving the field expansion region the decay particles enter a region of relatively strong electric field (i.e. at this point they are near the end of the tubular HV electrode. See section 3.3 for a detailed discussion of the electric field geometry). In this region the protons (which initially have an energy ≤ 750 eV) are accelerated to an energy of 30 keV. At this energy the protons can be detected well above the noise in the silicon detector. The electrons that exit the HV electrode will, of course, lose this much energy. However, *every* electron that arrives at the Silicon detector will have its energy reduced by an amount that corresponds *exactly* to the acceleration potential. Of course, some low energy electrons will be Penning "trapped". However, as noted above, the presence of the magnetic expansion ensures that every electron with a total energy that exceeds a threshold (50 keV for the a 4/1 field expansion and a 30 kV potential will reach the detector. Thus the electron spectrum above this threshold will exactly reflect the decay spectrum with only a fixed (and precisely known) offset.

Because the decay particles follow helical cyclotron orbits around the magnetic field line that passes through the location of the decay, they will hit the detector within two cyclotron radii (typically ≤ 1 cm) of the point where that flux line passes through the detector. If both the decay electron and proton go toward the same detector, they will hit within ~ 1 cm of each other. If the electron and proton go towards different detectors, they will both hit close to "conjugate" points on the two detectors. This fact is quite useful and we exploit it by using a pixilated silicon with a pixel size of about 0.7 cm^2.

With such pixilation, a “true” coincidence can only occur in the same pixel, in adjacent pixels, or in conjugate pixels on the two detectors. This greatly reduces the probability of a false coincidence. This procedure also provides a number of redundant methods by which this small false coincidence background can be accurately measured. In addition to the usual procedures involving adding time delays, one can look for false coincidences in non-adjacent pixels. Finally we note that the combination of the high magnetic field and pixilated detector provide a virtual (i.e. aperture free) collimation of the decay particles. Only those pixels whose magnetic field line passes through the neutron beam “see” any decays.

If a decay electron is completly stopped in the detector, its energy is either entirely deposited in a single pixel, or is shared between adjacent pixels. Each time there is a candidate event, the charge collected in every pixel that indicates an energy deposit above the noise threshold will be saved. A “real” event will show an energy deposit in only one, two, or three pixels (for hexagonal tiling). The total electron energy will be the sum. If an electron is backscattered from the Si (probability of $\sim 20\%$) it will either be reflected back (probability $\sim 85\%$) to the same (or adjacent) pixel by the Θ-pinch magnetic mirror, or it will escape (probability $\sim 15\%$) and strike the conjugate pixel on the opposite detector. Summing over adjacent and conjugate detectors gives the total electron energy.

Approximately 97% of the decay electrons deposit all of their energy in the first detector that they hit, either by stopping, or by backscattering and being reflected by the Θ-pinch. For such electron it is trivial to determine the initial direction (up-down) of the decay electron. The remaining 3% will split their energy between the two detectors. To determine the initial electron direction one must be able determine which detector was hit first. This implies that the detectors require a time resolution of comparable to the electron time-of-flight between the two detectors (typically a few to several ns). The issue of electron timing is discussed in detail in section 4.2.15.

Decay protons with ~ 30 keV of energy are detected with high efficiency in the first detector they hit (The probability for back scattering of protons is of order $\leq 1\%$ and the effects of proton backscattering are negligible (see section 4.2.9). Note that the energy deposit for all proton hits will be essentially the same (the variation in initial energies of ~ 100’s of eV is below the detector resolution of 1–2 keV. Thus while the energy deposited by the protons is much smaller than electron, a true proton event is identifiable by a nearly unique energy signal.

Because the decay region is in an electric field-free region, the proton initially drifts along the magnetic field lines with its original axial momentum. After this drift, the proton momentum is longitudinalized by the field expansion and the proton is then accelerated to ~ 30 keV. The magnet and electrode structure are designed so that the flight time in the field free region is much greater than the time of flight after longitudinalization and acceleration the total proton time of flight will be approximately proportional to $1/p_z$, where p_z is the axial component of the proton’s initial momentum. Thus the apparatus serves as simple proton spectrometer. The resolution of this spectrometer is limited to ~ 10 %. Nonetheless, even this rather rough resolution provides important information about the kinematics of the decay. The inclusion of this information increase the overall sensitivity of the measurement of a by a factor of ~ 2.3.

To summarize, using coincident detection of decay electrons and protons, the spectrometer provides, with high efficiency and low (well understood) background, the following reconstruction of each decay event:

1. Total electron energy — If the decay electron stops in a detector, its energy is either entirely deposited in a single pixel, or is shared between adjacent pixels. Each time there is a candidate event, the charge accumulated in every pixel that indicates an energy deposition above thresh-

old will be saved. The total energy can be later summed. If an electron is backscattered from the Si (probability of $\sim 20\%$) it will either be reflected back (probability $\sim 85\%$) to the same (or adjacent) pixel by the "Θ-pinch" magnetic mirror, or it will escape (probability $\sim 15\%$) and strike the conjugate pixel on the opposite detector. Summing over adjacent and conjugate detectors gives the total energy.

2. Sign of axial component of the electron momentum (electron up or down?) — Approximately 97% of the decay electrons deposit all of their energy in the first detector that they hit, either by stopping, or by backscattering and being reflected by the Θ-pinch. For such electron it is trivial to determine the initial sign of their momentum. The remaining $\sim 3\%$ will split their energy between the two detectors. The detector which was hit first gives this information. For such events one must time resolve the hits on the two detectors.

3. Sign of axial component of the proton momentum (proton up or down?) — The probability for back scattering of protons is of order $\sim 1\%$. Like electrons, protons will be reflected back to the original detector with high probability. With rather high probability the initial sign of the proton axial momentum is given by the detector showing a ~ 30 keV energy deposit.

4. Magnitude the axial component of the proton momentum — The decay region is in an electric field-free region and thus the proton drifts along the magnetic field lines with its initial axial momentum while undergoing transverse cyclotron orbits. The proton is then accelerated (to ~ 30 keV) into the silicon detector. Because the flight time in the field free region is much greater than the time of flight after acceleration (and because the TOF for the electron is far greater than that for the proton), the time delay between the electron and proton hits reflects the axial momentum of the decay proton. The resolution of this spectroscopic tool is limited by a number of effects to ~ 5–10%. This information substantially improves the sensitivity of the measurement to a.

3.2 Magnet Design

In this section we describe the new design of the spectrometer magnet addressing the recommendations of the Proposal Review and Advisory Committee (PRAC) from September 8–9, 2005. The PRAC key recommendation reads, *We strongly encourage the three efforts to investigate the option of a common magnet which could be tuned to provide the different field profiles needed for the three experiments...*

A common magnet has been modeled which can be tuned to generate different field profiles. The abBA profiles are presented here for three general regions of space: decay, drift, and detector regions. For a detailed description of the design parameters for all three experiments see [30]. The design parameters and criteria for the magnet are summarized in the next subsection 3.2.1. The spectrometer magnetic field is discussed in section 3.2.2. The magnetic field profile for the decay region is presented in 3.2.3 and a bief discussion of magnetic shielding is given in section 3.2.4. The transport of the polarized neutron beam through the magnet is discussed 3.2.5, while 3.3 deals with the design of the spectrometer electric field configuration.

3.2.1 Design Parameters and Criteria

The main functional requirements and design criteria for the magnet that were considered in the present design can be summarized as follows:

Magnetic Field Strength This experiment requires an expanding magnetic field. The field expansion parameter is defined as the ratio of the decay to the drift magnetic field strengths. The field strength in the decay and detector regions should be large enough so that the radii of the trajectories are contained within the acceptance of the pixilated charged particle detector. Table 3.2.1 summarizes the different magnetic field strength requirements.

B(T)	Decay	Drift	Detector
abBA	4.0	1.0	1.0

Table 1: Magnetic field strengths in the decay, drift, and detector regions.

Magnetic Field Homogeneity A homogeneity $dB/B < 10^{-2}$ is required in the decay region to minimize the effects of pinch reflection of the electron trajectories.

Electric Field A High Voltage Electrode configuration held at approximately 30 kV is required because the maximum proton energy is only $\sim$ 750 eV. This ensures that the protons are accelerated and gain enough energy to be detected.

Silicon Detectors The magnet must accommodate the operation of a pair of segmented silicon detectors to detect electrons and protons in coincidence mode. The strong magnetic field insures that the only low energy particles that can strike the detector come from the decay volume, which is at ultra-high-vacuum. Detection efficiency must be essentially 4π.

Magnet Length The length of the magnet should be at least 2 m on each side of the decay region. This requirement is driven by the following considerations:

1. Detector timing resolution to reconstruct electron backscatter events where both detectors are struck, and
2. a proton time of flight measurement that will give a statistical measurement of the coefficient a that is close to the theoretical limit of $2.4/\sqrt{N}$, where N is the total number of decays.

Magnet Diameter The magnet diameter should be at least 20 cm in the drift and detector regions. This requirement is driven by the following considerations:

1. The size of the detectors that fit inside the magnet. The detector package has an OD of 16.4 cm and additional space should be allowed for engineering the final mountings and HV electrodes.
2. Charged particles trajectories in field expansions of 10:1 (required for other field configurations) and greater require this space to reach the detector region.
3. Physical requirements to fit the HV electrode structure.

Neutron Beam Access The spectrometer must permit an approximate 8–10 cm gap to allow for the transmission of the neutron beam.

Spin Transport The magnetic field must allow the transmission of a polarized neutron beam in and out of the decay region without a significant loss of polarization. The requirement is that the loss of polarization should be $< 0.15\%$.

Fringe Magnetic Field According to the SNS magnetic field policy “Policy on Magnetic Interference,” which sets limits on stray magnetic field variations on the sample location, the stray field from the spectrometer magnet on the dividing line between neighbors should be less than 50 mG.

Mechanical Stability The magnet support structure must provide stability to minimize coil movement when energized to the different power considerations.

Thermal Stability The magnet field requirements demand the use of superconducting technology.

Affordability The magnet should be built using conventional superconducting technology and optimize dimensions to reduce cost.

3.2.2 Spectrometer Magnetic Field

A 3-D model of the spectrometer conceptual design is shown in Figure 3. It consists of a split pair superconducting solenoid followed by a transport solenoid. The separation of the split pair conductors as shown here is 10 cm and the diameters are 20 cm each, i.e., the geometry of a Helmholtz coil. Each transport solenoid is also 20 cm in diameter and about 2 m long. The choice of a common diameter (20 cm) is driven by the practical consideration of having a common bore for the transport solenoid and the split pair. The possibility of relaxing this constraint should be evaluated in terms of operations and costs. Considerations of the electric field configuration and of cryogenics seem to favor a common diameter throughout the magnet.

The configuration of Figure 3 has been modeled using the code Opera-3d from Vector Fields. The coordinate system is such that the z-axis is along the axis of the spectrometer. The neutron beam can propagate in either the x or y direction.

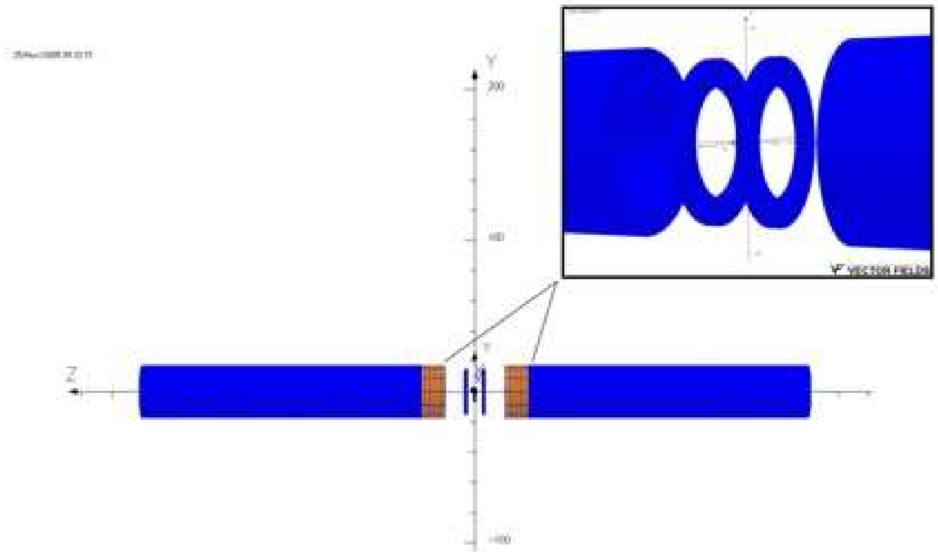

Figure 3: The magnetic spectrometer showing the split pair and transport solenoid. Dimensions are in cm.

The choice of the split pair is driven by the field strength and homogeneity requirements. The separation between the split pair conductors is driven by the transport the neutron beam and by allowances for hardware. We have studied separations ranging from 5 to 10 cm. The strength and homogeneity requirements can be met for diameters of 20 cm. This is our present choice and is driven by practical considerations like physical requirements to fit the HV electrode structure. Diameters > 20 cm for the split pair are not practical for maximum fields of 4 T because the fields at the position of the conductors would exceed the quenching field (9 T) for standard NbTi wires.

The transport solenoid has been modeled by a series of 2.5 cm long adjacent conductors instead of a long, single current solenoid. This permits current adjustments necessary to produce the required magnetic field configurations. The 20 cm diameter is driven by the space requirements and the particle trajectories in field expansions of 10:1. Field expansions > 10:1 will require a larger diameter, i.e., a 25 cm diameter will accommodate field expansions up to about 18:1. In the present model the transport solenoid starts at $z = \pm 15$ cm and extends to $z = \pm 220$ cm.

The magnetic field on the spectrometer axis for the abBA configuration is shown in Figure 4. The maximum field is 4 T followed by a 4:1 expansion directly into the drift and detector regions. The transport solenoid is powered starting at $z = \pm 22.5$ cm. The uniformity of the field in the drift region can be optimized by small current adjustments. To achieve a uniform field at the detector positions ($z = \pm 200$ cm) the current has to increase by about 50% for $z > 200$ cm with respect to the almost constant drift-region current. Figure 5 shows the current used in each of the 2.5 cm long segments that make up the model of the transport solenoid

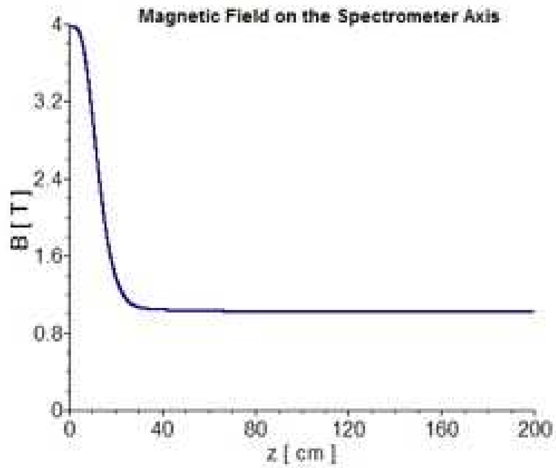

Figure 4: The magnetic field on the spectrometer axis for the abBA experiment.

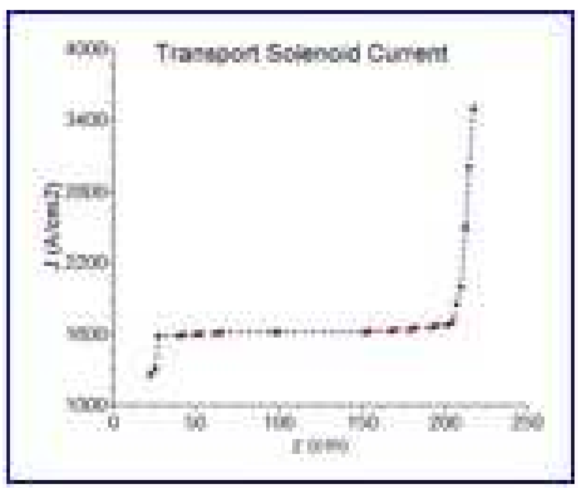

Figure 5: This figure shows the current used in each of the 2.5 cm long segments that make up the model of the transport solenoid.

We have simulated electron trajectories through the abBA configuration. As an example we have chosen electrons with perpendicular momentum close to the maximum value, 1200 keV/c. These trajectories are the ones with maximum radius of gyration. Figure 6 shows a sample of trajectories originating at a radial distance from the spectrometer axis as a function of distance along the z-axis. As expected the charged particles spiral around magnetic field lines. After the field expansion the radius of curvature is larger and consistent with $r_f = r_i\sqrt{\frac{B_0}{B_f}} = 2r_i$, the adiabatic condition.

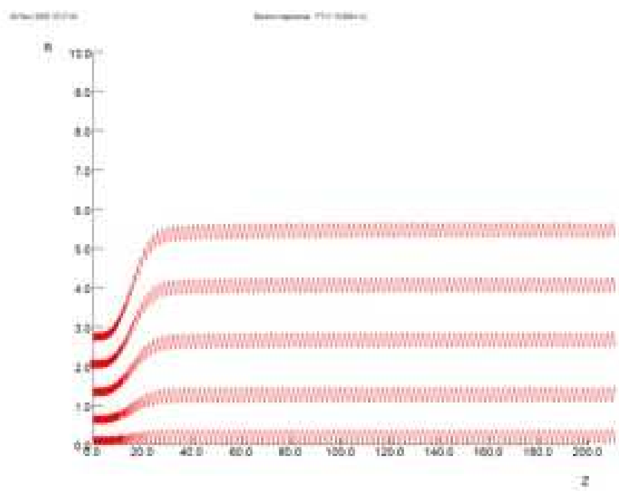

Figure 6: Electron trajectories for the abBA configuration. The radial distance from the spectrometer axis is plotted as a function of distance along the z-axis.

3.2.3 Magnetic Field in the Decay Region

We present results for the magnetic field profiles in the decay region for two split coil separation distances, namely 8 and 5 cm. The results are summarized in Figures 7 and 8, respectively. The overall consideration here is that to avoid pinching (trapping) of the particles in the field, the magnetic field for z = 0 has to be greater or equal than the field for $z > 0$ or $z < 0$, along a direction parallel with the spectrometer axis.

Figure 7 shows the field profiles along the spectrometer axis in the decay region, from $z = -4$ cm to $z = 4$ cm, for different values of the variables x and y which are perpendicular to the z. The decay region can be approximated as a volume $\Delta x \Delta y \Delta z$. The results of Figure 7 show that if the distance between the superconducting coils is $D = 8$ cm then a decay volume that will avoid increasing fields in the z-direction will be constrained by either $\Delta x < 6$ cm, $\Delta y < 2$ cm, or $\Delta x < 4$ cm, $\Delta y < 2$ cm. Figure 8 shows the results for a distance between the superconducting coils of $D = 5$ cm. In this case the decay volume can be chosen as large as practically possible.

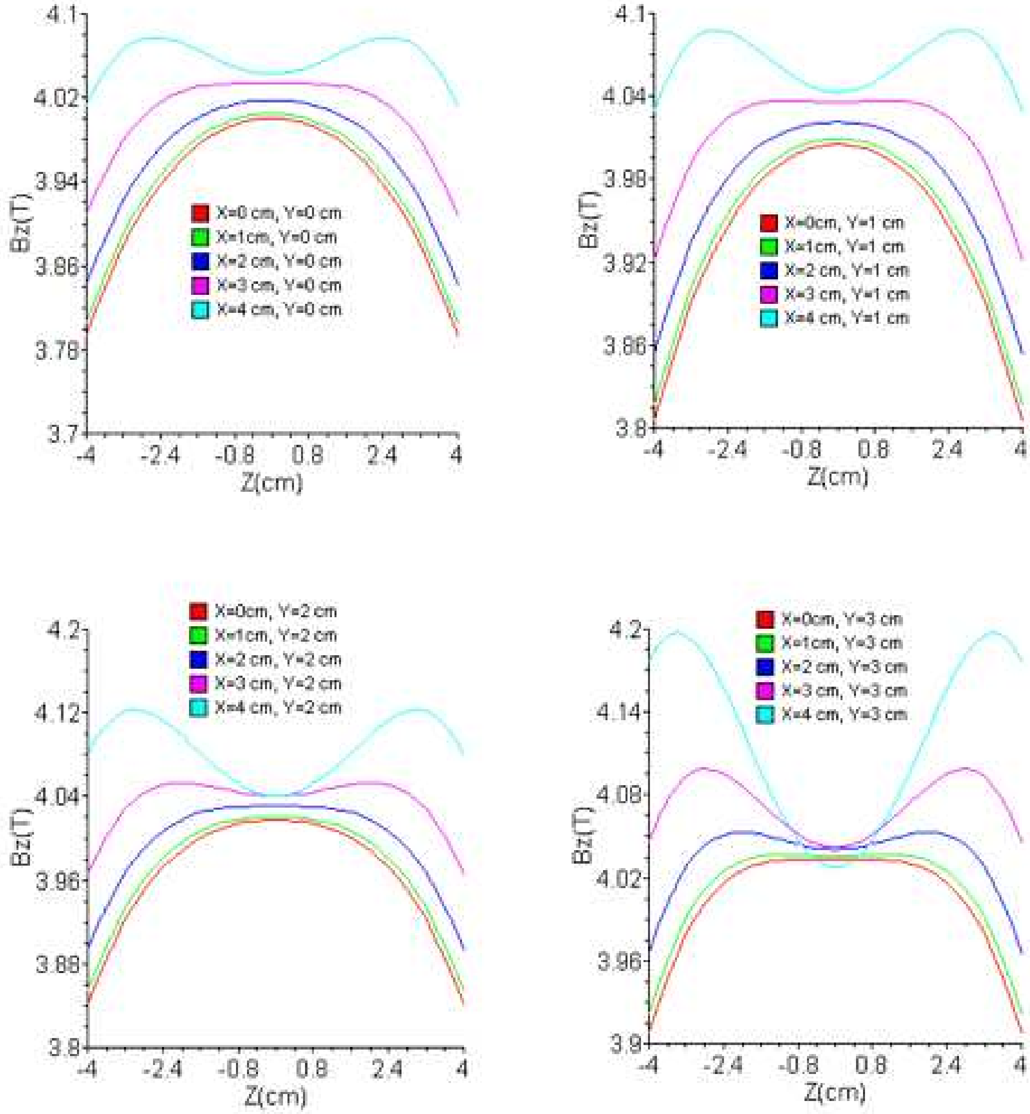

Figure 7: Magnetic field profiles in the decay region. The split pair separation is 8 cm. The figures show the field as a function of z for different values of the variables x and y in the decay region. The requirement that particles experience only a field of decreasing magnitude renders this configuration unacceptable.

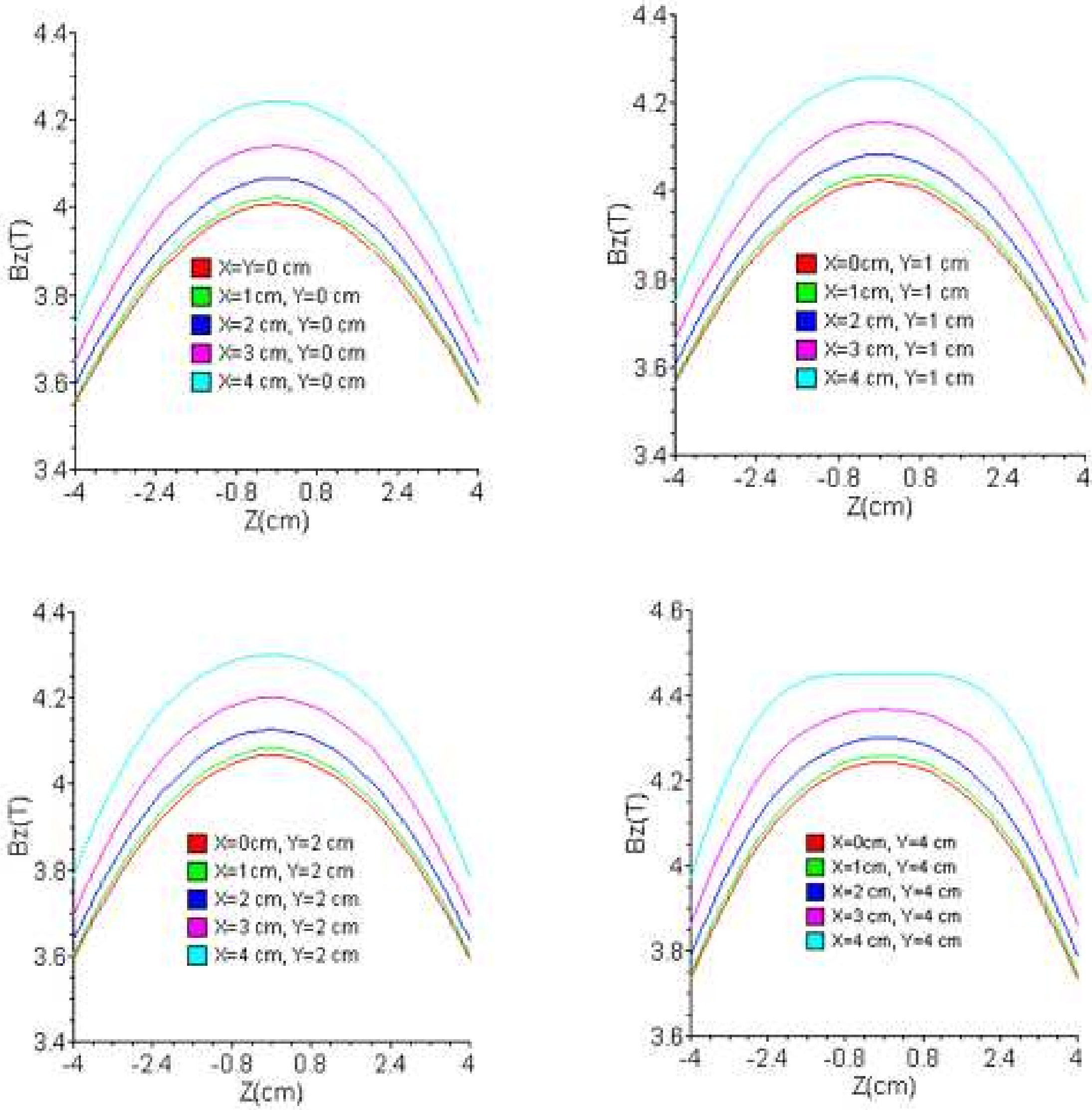

Figure 8: Magnetic field profiles in the decay region. The split pair separation is 5 cm. The figures show the field as a function of z for different values of the variables x and y in the decay region.

3.2.4 Magnetic Field Shielding

According to the SNS magnetic field policy "Policy on Magnetic Interference," which sets stray magnetic field variations on the sample location, the stray field from the spectrometer magnet on the dividing line between neighbors should be less than 50 mG. The present magnet will be vertical so it is located approximately 1.8 m away from the dividing line between neighboring beam lines.

We have evaluated the fields away from the magnet. They are shown in Figure 9 and 10. The Figure 9 shows the field in the x-direction, perpendicular to the magnet axis, while Figure 10 shows a field profile of 2 m by 2 m at a distance $x = 1.5$ m.

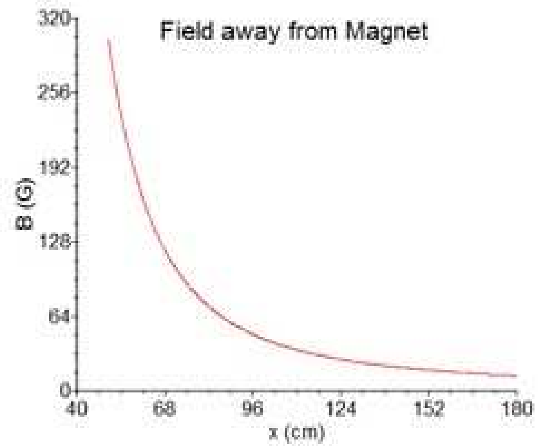

Figure 9: Magnetic field away from the magnet center in a direction perpendicular to the magnet axis.

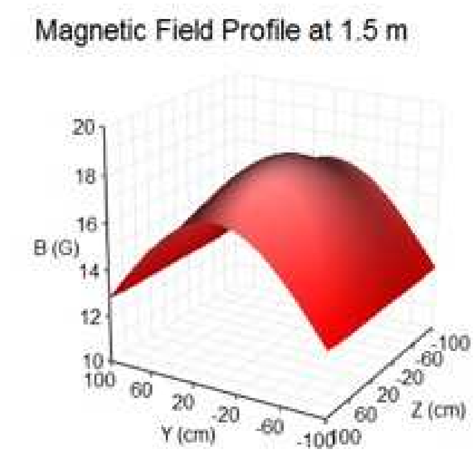

Figure 10: Profile at $x = 1.5$ m.

The fields need to drop by about 10^3 to be within the requirements of the SNS policy. We are in the process of evaluating the shielding of these fields with an iron-type enclosure around the spectrometer.

3.2.5 Spin Transport Through Magnet

Neutrons depolarize when the magnetic field through which they move changes faster than Larmor precession. In the present design the magnetic field of the split pair changes signs in the mid-plane at about 16 cm away from the origin and it would cause significant depolarization. An estimate of the field needed to maintain the polarization is given by the following adiabaticity parameter

$$\lambda = \frac{\mu B^2}{2\hbar \frac{dB}{dz} \nu} \tag{11}$$

and the following expression for depolarization:

$$D = \frac{\pi}{6} e^{\frac{4}{3} - \frac{\pi\lambda}{2}},$$

which gives fields of about 500–1000 G to preserve polarization.

We have performed preliminary modeling by performing Monte Carlo calculations. For this a new coordinate system is used where the z-axis goes along the neutron beam and the spectrometer axis is the y-axis.

We have studied two possible configurations: a solenoid along the path of the neutron centered on the field zero crossing and a couple of short solenoids with axes perpendicular to the direction of the neutron beam. We have found that the latter configuration requires a smaller canceling field than the longitudinal solenoid and that it does not introduce additional gradients. This configuration of symmetric coils has been added to the magnet model as shown in Figure 11. This configuration can also be accomplished with a $\cos\theta$-type of coil. In this case the coil axis will along be the neutron beam but the field will be perpendicular to it.

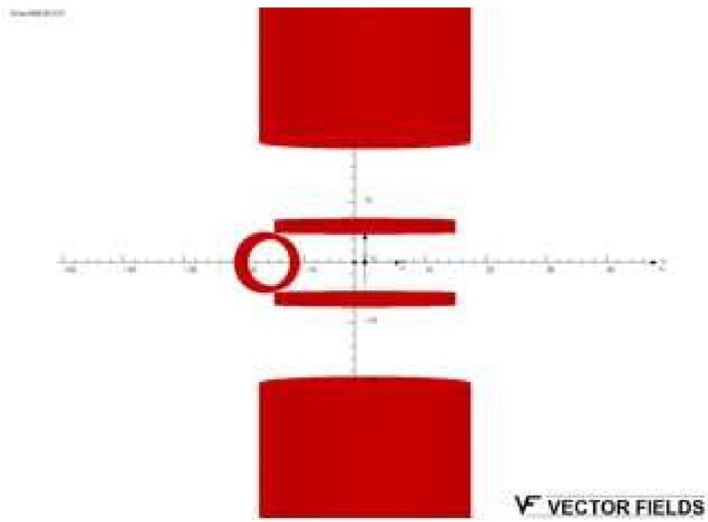

Figure 11: Coils used to transport the polarized neutron beam.

Simulations have been carried for different field strengths. The ratio of the transmitted polarization to the incoming polarization is plotted in Figure 12 and 13 as a function of the incoming neutron energy for both configurations. These results are preliminary and optimization is underway.

3.3 Electric Potential

Because the decay protons have a maximum kinetic energy of < 1 keV, they must be accelerated to at least a few $\times 10$ keV to be detectable above the electronic noise of the Si detectors. This acceleration is accomplished by maintaining a potential difference between the neutron decay volume and the Si detectors. One may establish this potential difference by either 1) establishing the decay region at ground and holding the detectors at $-V$, or 2) establishing the decay region at $+V$ and holding the detectors at ground. Although method 1 has been successfully employed in the NIST Penning trap lifetime experiment and the emiT experiment it presents the practical problem of extracting the fast detector signals to a DAQ at ground. In practice this method has experienced problems related to detector failure following breakdown. Method 2 is conceptually simpler, but, in a configuration with a strong magnetic field, it can establish a Penning trap for electrons which may be susceptible to HV breakdown. Because of the complexity, expense, and potential fragility of our DAQ we have elected to utilize method 2.

Our electric fields are maintained by three cylindrically symmetric electrodes as shown schematically in Figure 14. The central electrode is maintained positive with a potential of $\sim$ 20–50 kV while the end electrodes are at ground. Our anticipated detector noise levels as well as extensive experience in previous decay experiments indicate that such a potential difference is more than ample to allow efficient detection of the protons above the detector noise. In practice, our HV system is designed for operation at up to 50 keV. Because variation of the potential provides a useful systematic check, decay data will be taken at a variety of potentials.

Our baseline electrode design was selected to satisfy four criteria: uniformity of the electric field

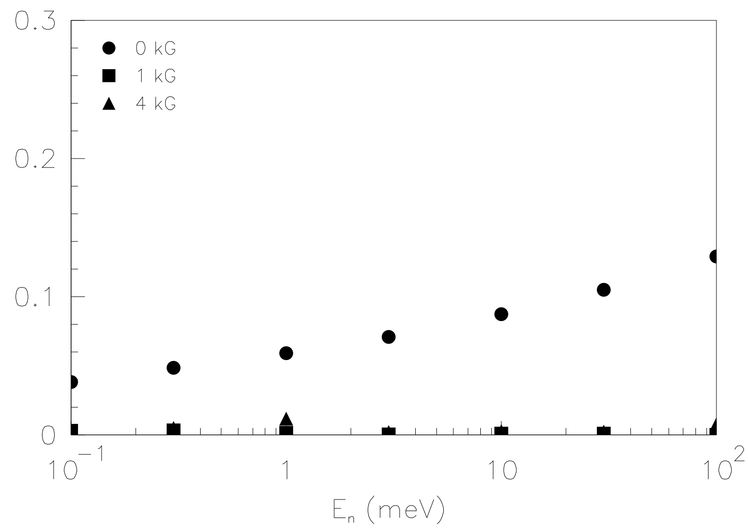

Figure 12: The ratio of the transmitted to the incoming neutron polarization as a function of the neutron energy with perpendicular pair of solenoids as in Figure 11.

over the neutron decay volume, tracking of particle orbits in the electric filed acceleration volume, stability against breakdown, and engineering soundness.

1. Uniformity of the electric field over the neutron decay volume. The symmetry of the electrode structure implies that the highest potential will lie at the mid-plane of the central cylinder. A decay proton created above mid-plane with a very small downward longitudinal velocity would be reversed if its "longitudinal kinetic energy" were insufficient to overcome the potential barrier created by the field maximum at the mid-plane. Thus, the detection of such protons must be considered as possible systematic effect in the measurement of the a correlation. In principle, this effect is calculable, but it is desirable that the electric field from the HV electrode structure is sufficiently uniform that this effect is negligible.

2. Tracking of particle orbits in the electric field acceleration volume. An underlying assumption of the proposed experimental method is that centroid of the cyclotron orbit of any decay electron or proton trajectory closely follows the magnetic field lines. If this assumption is satisfied, the electron-proton coincidences will occur in the same (or adjacent) detector pixels or will occur in conjugate pixels on opposite ends of the apparatus. Similarly, backscattered electrons from the silicon detectors will hit adjacent or conjugate pixels. This condition is, of course trivially met in the case of a uniform magnetic field. However, the addition of an electric field that has a component perpendicular to the magnetic field will cause the orbit centroids to drift from the magnetic field lines. This drift will be small if the magnetic forces are much larger than the electric forces. This condition is verified by direct calculation of the fields and particle energies as well as by detailed orbital calculations.

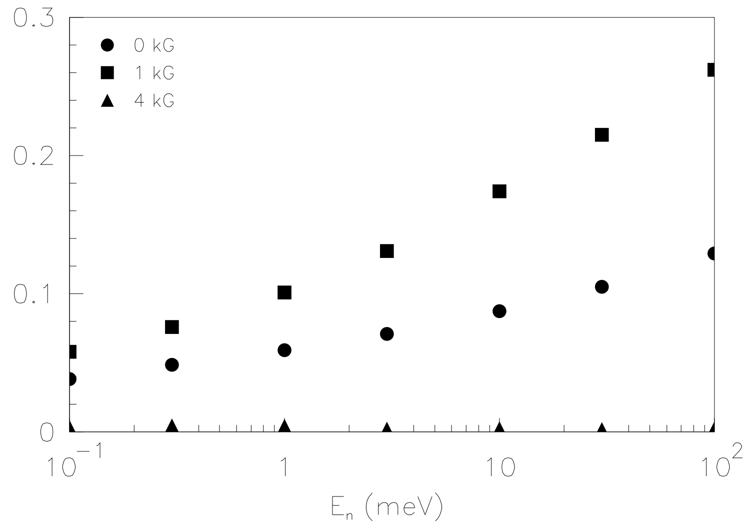

Figure 13: Same as Figure 12 but with correction solenoid along the neutron beam direction.

3. Stability against breakdown. Maintaining high electric potential in vacuum in a high magnetic field is notoriously difficult. Our HV systems is designed in accordance with standard HV practices (i.e. minimization of E fields at surface, electro-polished surfaces, etc.) and additionally uses lessons learned in other HV application including experience with previous beta decay experiments and other applications (i.e. judicious placement of insulators, TiN coatings, etc.).

4. Engineering soundness, HV system, and safety. In addition to producing a suitable electric field configuration, the electrode configuration must be structurally sound, compatible with the rest of the apparatus, and capable of being aligned and positioned with appropriate accuracy. Furthermore the system must be configured in such a way as to ensure that there is no personal risk associated with the applied high voltage.

Uniformity of the electric field over the neutron decay volume In the geometry of Figure 14, the center of the HV electrode is the maximum of electrostatic potential. This implies that for a proton emitted in a decay above or below the center the proton would be reversed if its initial velocity were toward the center and its kinetic energy was sufficiently small so that it could not “get over” the potential maximum at the center. Such a proton will be detected by the “wrong” silicon detector. While the overall symmetry of the system is such that this effect will not contribute to an error in the spin dependent correlations A and B, the detection of such “reversed” protons will contribute to an error in the unpolarized correlation coefficient a. The design of the experiment, and particularly the electrodes, must be such that the effect of such events will be sufficiently small so as not to contribute an appreciable error in the measurement of a.

This situation will be satisfied if the uniformity of the electric field in the decay region is suf-

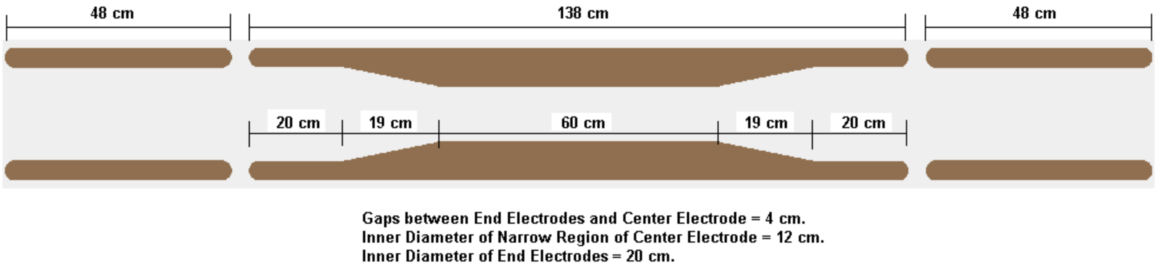

Figure 14: Schematic of Cylindrically Symmetric Electrodes.

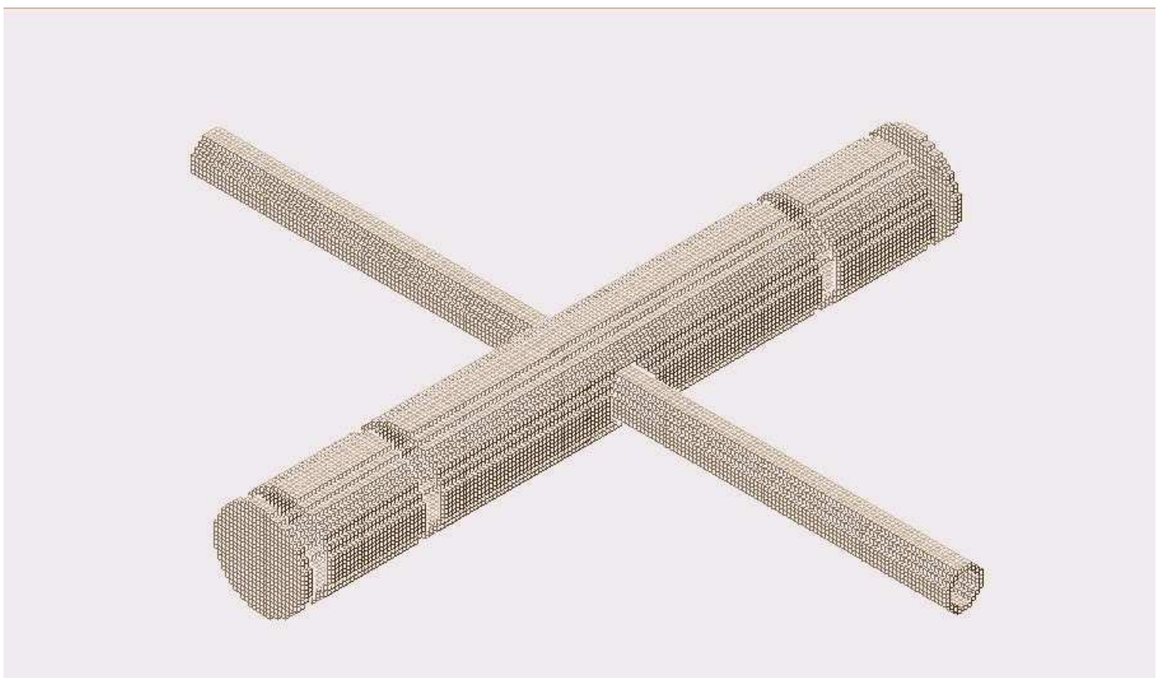

Figure 15: Schematic of electrode structure showing input/output tubes which maintain field uniformity at the decay region and allow neutrons to enter the cryostat. Also shown is the position of the silicon detectors.

ficiently small that only a negligible fraction of the decay events are reversed. This fraction may be estimated by noting that the probability that a proton will be created with a z-component of velocity $v < v_z < v + dv$, where v_z is the axial component of the velocity, is approximately constant for $v << v_{\max}$. This probability is given by $dP \approx g(0)dv$, where $g(0)$ is the value of the single component velocity distribution at $v = 0$. For any reasonable distribution, $g(0) \approx 2/v_{\max}$, which implies that for decay protons $g(0) \approx 5 \times 10^{-6}$ (m/s). If our goal is the measurement of a with an error $\Delta a/a \approx 10^{-3}$, and note that $a \approx 0.1$, we conclude that we want $< 10^{-4}$ of the events to have an incorrect determination of the proton's initial direction. This implies that the inhomogeneity of the electric field must be such that it will not reverse a proton with an initial z component of velocity of $\sim$ 20 m/s. The kinetic energy associated with such a velocity is $\sim$ 2 μeV. Thus we conclude that a field design based on this criterion would require a field uniformity of on the order of a few micro-volts in the neutron decay volume.

As a coincidence experiment, the proposed measurement will only count events in which a proton is detected in a finite time "window" following the detection of a (much faster) electron. Decays in which the proton time of flight is longer than this window will not be recorded in the DAQ. Such "lingering" protons will contribute to a very small false coincidence rate which can be accounted for in the usual fashion. It is important to realize that the protons which undergo reversals require a comparatively long time to reach the silicon detectors. If this time is longer than the coincidence timing window, no incorrectly identified protons will be recorded in the DAQ. As we will show below, for the selected geometry, the time of flight for protons that undergo a reversal is much longer than the coincidence time window. In the following we shall assume that the longest reasonable decay windows will be < 100 μs.

The time of flight for a proton from creation in a neutron decay event to impact on the detector will be determined by the location of the decay, the energy of the decay proton and the direction of the proton's initial momentum.

Figure 16 is the TOF plot of a simulated proton with energy ranging from 0 to 3 μeV. The simulated proton is created on the central axis of the spectrometer some set distance (0.5, 1.0, 1.5 and 2.0 cm) from the mid-plane of the central cylinder. Initially, the proton is traveling in the direction of increasing (negative) potential, and the velocity of the proton is entirely in the direction of the central axis of the cylinder. As can be seen from the plot, the TOF of the proton increases asymptotically with increasing energy. The energy corresponding to the peak of the asymptote is the minimum energy needed to overcome the potential barrier between the location at which the proton was created and the mid-plane of the cylinder. A proton with energy less than the minimum energy will be reversed and will strike the "wrong" silicon detector, whereas a proton with energy greater than the minimum energy will overcome the potential barrier and will hit the "correct" silicon detector. As an example, the curve in Figure 16 for a proton created 1 cm away from the mid-plane of the central cylinder indicates an asymptotic energy of 0.4 μeV. The asymptotic energy of 0.4 μeV also represents the voltage drop between the mid-plane of the cylinder and a point 1 cm away.

The discussion above is based on an assumption that the electrodes are "perfect" conductors. At the required field uniformity (a few $\mu V/cm$), the imperfect nature of real metallic conductors must be considered. It is well known that the orientation dependent work function of individual metallic grains ("patch" effect) can give rise to local electric field variations of order mV's very close to a metallic surface (In this context, "very close" means on the order of the dimensions of an individual

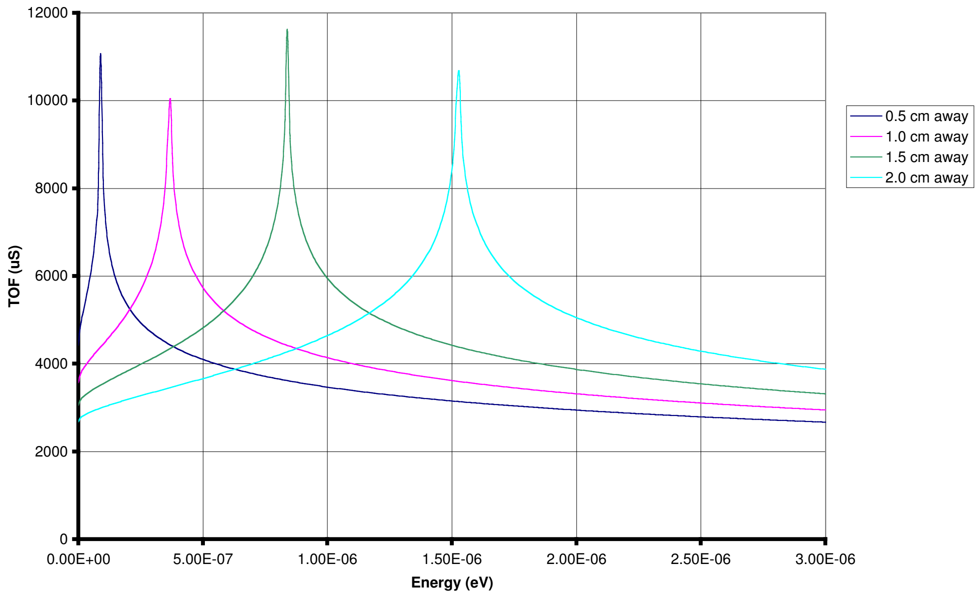

Figure 16: Proton time-of-flight versus energy

grain). The hope is that the patch effect averages to zero when the distance to the surface becomes large, but experience from the aSPECT experiment [31] shows that this is not necessarily the case for technical surfaces. The reasons are not yet understood, impurities in or on the surface coating might be responsible of their finding, which is a variation of the work function 100 mV over a distance of 5 cm. In addition, in [32] surface charging on metallic conductors due to radiation is found and discussed. The effect can be as big as several Volts, but at radiation levels which are many orders of magnitude higher than in abBA. Our strategy is as follows: We will test our surfaces with a Kelvin Probe, with which the level of local variations of surface charges and the work function can be measured with an accuracy of several mV. We can minimize the effect by considering different surface materials and treatments. We will coat the inside of the electrode, at least in the vicinity of the decay region, with evaporated gold, colloidal gold, colloidal carbon or similar material which has been shown to significantly reduce the work function inhomogeneities. Furthermore, we can test at the neutron beam if the radiation level there makes a difference. And finally, as we will not be able to measure inhomogeneities directly if their amplitude is below a meV, we will use the effect that protons that can be reflected by such small electric potentials arrive at the very end of the time of flight spectrum of the protons, and can thus be identified and removed, if necessary.

In addition, the electric potential of the detectors (0 V, to be compared to the 30 kV of the decay volume region) can give rise to electron reflections. This is unavoidable for electrons with an energy around or below 30 keV. The magnetic expansion of 4:1 turns the electron momentum to have an angle relative to the magnetic field which is $\theta = 45^o$ [33] at maximum, since $\sin^2\theta/B$ is an adiabatic invariant of the electron motion. Every electron with a kinetic energy of at least 30 keV $/\cos^2\theta = 60$ keV can get to the proton detector.

Tracking of particle orbits in the electric field acceleration volume The proposed experimental method assumes that the centroid of the cyclotron orbit of any decay electron or proton trajectory closely follows the magnetic field lines. If this assumption is satisfied, the electron-proton coincidences will occur in the same (or adjacent) detector pixels or will occur in conjugate pixels on opposite ends of the apparatus. Similarly, backscattered electrons will hit adjacent or conjugate pixels. This condition is, of course trivially met in the case of a uniform magnetic field. However, the addition of an electric field that has a component perpendicular to the magnetic field will cause the orbit centroids to drift from the magnetic field lines. If the electric field is sufficiently large, the particle orbits could in principle never reach the detectors. Roughly speaking, the condition that our field configuration must meet is that the magnetic forces dominate rather than the electric forces.

We demonstrate the suitability of our field configuration in two ways. The first method is based on a scaling argument which demonstrates that, in general, the particle velocities and the fields satisfy a “tracking” condition which implies that the centroids of the cyclotron motion follow the magnetic field lines. The second method involves a detailed simulation of the entire range of particle trajectories in the actual field geometry. The simulation shows that for all initial particle energies and momenta propagated from the neutron decay region, the resulting trajectories reach the detector very close to the projection of the magnetic field line at which they began.

In the acceleration region between the electrodes, the magnetic field is uniform and in the z direction. We may define a characteristic velocity $v_{EB} = E_r/B$, where E_r is the radial component of the electric field. The specific condition which we wish to satisfy is that for all points on its trajectory, the particle velocity fulfills $v >> v_{EB}$. A rough scaling argument indicates that we expect $v_{EB} \approx Vr/Bd^2$ where V is the acceleration potential, d is the electrode diameter, and r is the off-axis distance of the trajectory in the acceleration region, and B is the magnetic field. For the reference geometry, $v_{EB} \approx 5 \times 10^3$ m/s. The proton will have gained some energy before reaching the region of peak electric field and may be assumed to have a velocity (at an energy of order 1 keV) of $v \geq 5 \times 10^5$ m/s.

This condition can be verified through a direct calculation of the fields and particle velocities. Figure 17 plots the quantity $v/(E_r/B)$ for an off-axis proton with an orbit going through the region where E_r is maximal. As can be seen from the plot the adiabatic condition is well satisfied everywhere along the particle trajectory.

A more detailed way of demonstrating that the tracking condition is met is by calculating the particle trajectories and demonstrating that all particles reach the detector close to the point at which the magnetic field line on which they started intersects the detector. In this context, “close” means less than, or comparable, to the typical cyclotron orbit size and certainly smaller than the anticipated pixel size of ~ 1 cm.

Figures 18, 19, and 20 show the arrival location distributions of simulated protons with energies of 5, 300, and 700 eV, respectively (Note: Each plot represents 5000 simulated protons). These protons originate from the center of the mid-plane along the central axis ($y = 0$, $z = 0$) and are ejected randomly in a cone of 0° to 90°. For a given energy, as the initial angle increases, the protons strike the detector farther from the center.

In comparison, Figures 21, 22, and 23 show the arrival location distributions of off-center simulated protons with energies of 5, 300, and 700 eV, respectively. These simulated protons originate in the mid-plane a distance 25 mm from the central axis ($y = 25$, $z = 0$) and are ejected randomly in a cone of 0° to 90°. Due to the magnetic field expansion, the arrival locations of these protons are shifted in the y direction with respect to the initial position. In addition, the magnetic force $F_B = q\vec{v} \times \vec{B}$ creates a small shift in the z direction.

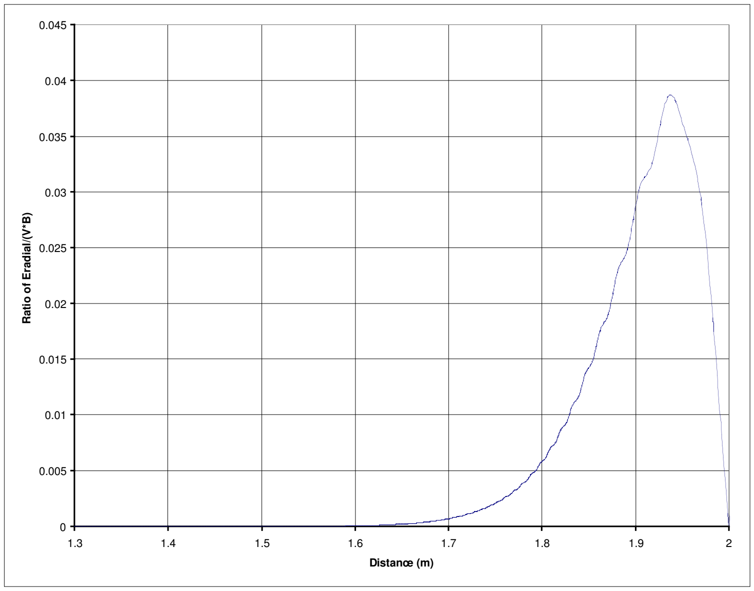

Figure 17: Plot of $E_r/(vB)$ versus distance for a 300 eV 45° proton.

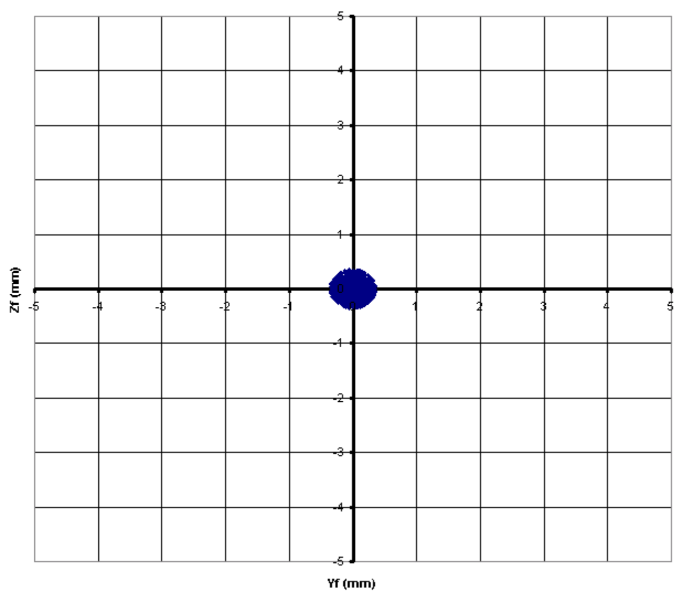

Figure 18: Plot of the final positions of 5 eV protons with initial position $y = 0$, $z = 0$.

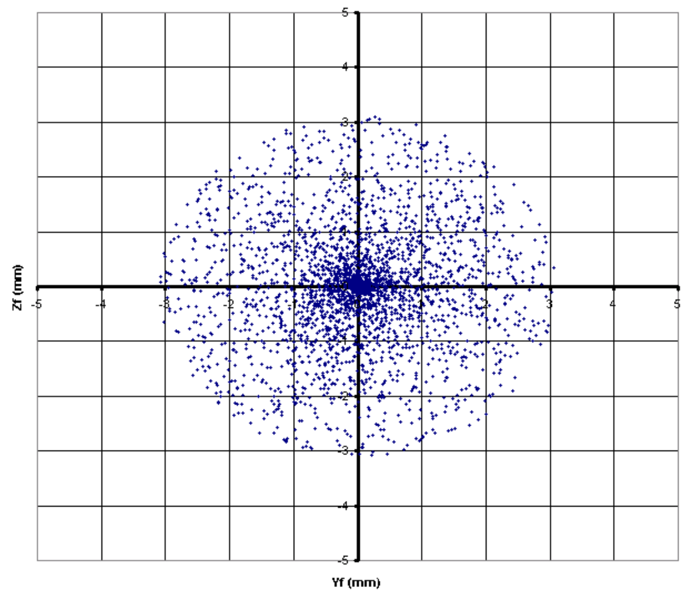

Figure 19: Plot of the final positions of 300 eV protons with initial position $y = 0$, $z = 0$.

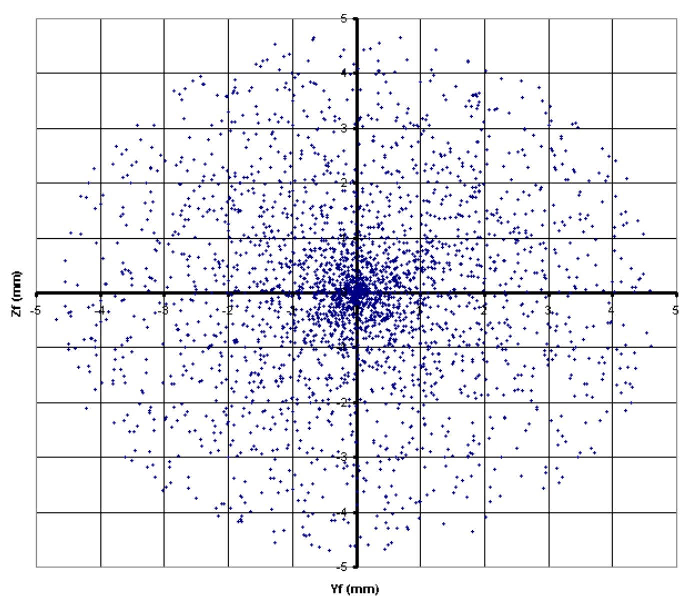

Figure 20: Plot of the final positions of 700 eV protons with initial position $y = 0$, $z = 0$.

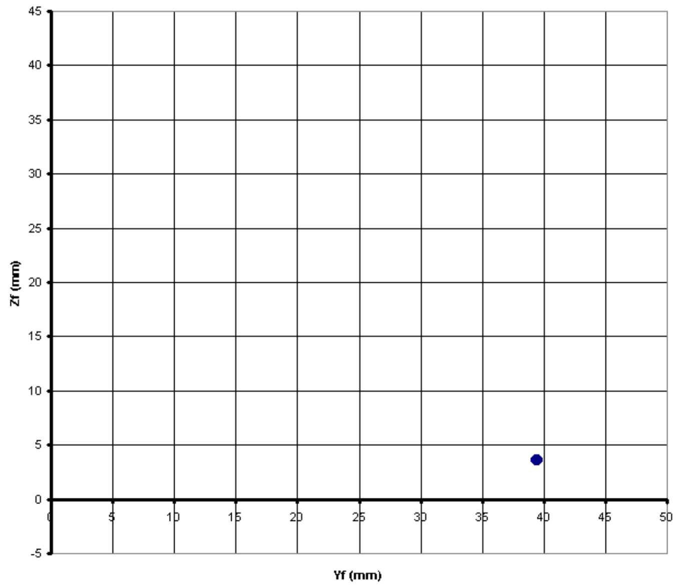

Figure 21: Plot of the final positions of 5 eV protons with initial position $y = 25$, $z = 0$.

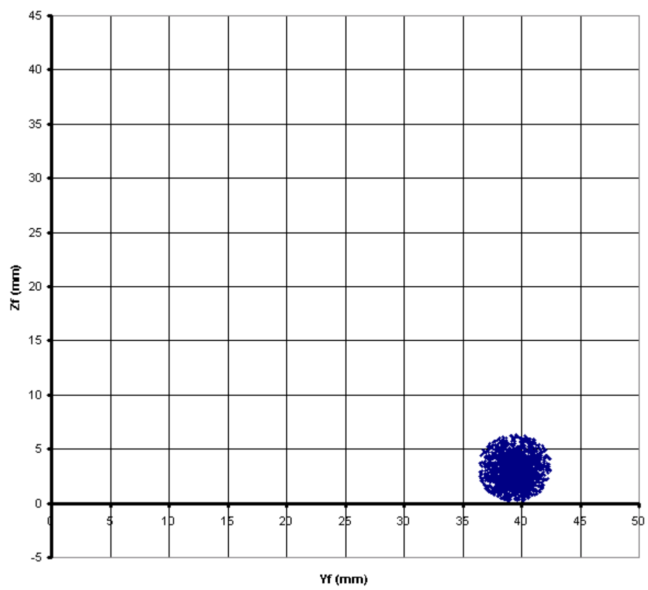

Figure 22: Plot of the final positions of 300 eV protons with initial position $y = 25$, $z = 0$.

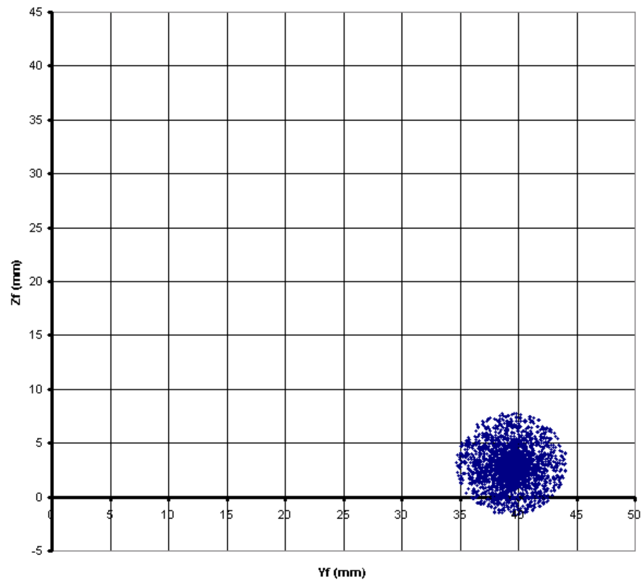

Figure 23: Plot of the final positions of 700 eV protons with initial position $y = 25$, $z = 0$.

The calculations and simulations above show that the baseline electrode design will satisfy the homogeneity and particle tracking requirements.

Stability against breakdown The maximum electric field in the electrode geometry of Figure 14 is approximately 8 kV/cm if the center electrode is kept at the nominal 30 kV. Maintaining such a field would pose no problem for breakdown in vacuum were it not for the presence of the high magnetic field. However, experience has shown that even such relatively modest fields can be quite unstable in the presence of several Tesla magnetic fields. Our design addresses this problem through the following well established features:

Shape No sharp corners or edges are present. The minimum radius of curvature is 1.0 cm.

Surface Finish All surfaces of the electrodes will be mechanically polished and then electropolished to eliminate surface imperfections that could induce local field maxima.

Surface Coating Electrode surfaces in regions where the electric field is significant.will be coated with TiN coatings. Such coatings are known to significantly reduce secondary electron emission, which is thought to be related to breakdown in strong magnetic fields.

Insulators Wherever possible, and particularly in the regions of high local fields, the space between the electrodes will be filled with insulating material (high density alumina or similar) with high resistance to electric field breakdown. Figure 24 shows the setting of the insulators relative to the electrodes.

We note that the maximum electric and magnetic fields in the baseline design are substantially lower, and the geometries are more favorable, compared to the NIST Penning trap experiment which ran at voltages of $\sim$ 30 kV and at $\sim$ 4 T. We also note that in the NIST experiment, not all the HV surfaces were electro polished, none were TiN coated, and the high voltage components were not surrounded by insulators. We are confident that our baseline design will allow operation up to our design goal of 50 kV.

Engineering soundness, HV system, and safety In addition to the performance requirements described above, the electrode system must be structurally sound, compatible with the rest of the apparatus, and capable of be aligned and positioned with appropriate accuracy. In addition, the electrodes must be designed to allow the entrance of the neutron beam to the decay region. Finally, it is critically important that the system must be configured in such a way as to ensure that there is no personal risk associated with the applied high voltage. See Figure 25 shows the general layout of the electrodes.

Figure 24: A close up of the electrodes, showing the insulators in between.

3.4 Charged Particle Detectors

The measurement of the parameters a, b, A, and B requires that both electron and proton resulting from the decay must be detected. Since the determination of A and a also requires knowledge of the

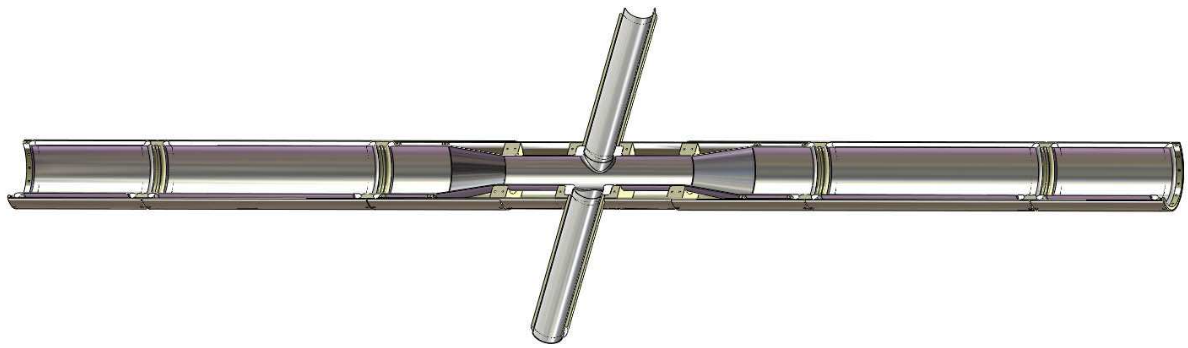

Figure 25: A drawing of the general layout of the electrodes.

electron velocity β, the electron total energy must be accurately measured. Since a non-negligible fraction of electrons backscatter from one detector and deposit the remaining energy in the opposite detector, the timing of electron hits must be resolved with sufficient resolution to determine which detector was struck first. Finally, because the neutron densities are relatively low in the spectrometer, the detectors must be large enough to achieve a sufficient counting rate. The requirements for the detector are:

1. accurate calorimetry for electrons with energies 50–800 keV,
2. detection of protons with energies of 30 keV,
3. large area (≈ 100 cm^2),
4. position sensitivity,
5. small and position-independent reflection probability for electrons,
6. accurate (few nanosecond) timing,
7. high and stable electron detection efficiency,
8. position-independent detection efficiency,
9. and energy-independent detection efficiency.

Silicon detectors can meet all of these criteria. They have inherently good energy resolution and almost unity efficiency, independent of position and energy. They can be made large in area with position sensitivity without the introduction of dead areas. Thin dead layer technology can be employed to allow low energy proton detection and adequate timing has been demonstrated. It is important to note that *all* of the required characteristics have been demonstrated in commercial detectors.

The charged-particle detectors for the spectrometer will be made from 15 cm diameter, 2 mm thick silicon wafers. Charged particles will enter the detector through the junction side. Charge deposited by the particles will be collected on the ohmic side. The active area of the detector will be segmented into 127 individual elements. The detector will be mounted to a ceramic support, suitable for cooling to cryogenic temperatures. Behind the ceramic support will be a circuit board with individual FETs, as well as feedback resistors and capacitors for each detector channel. Since the range of 752 keV electrons in silicon is approximately 1.7 mm, a 2 mm thickness is sufficient to stop the highest energy decay electrons. The range of the protons in silicon is much shorter, 0.3 μm.

The junction side of the detector will be formed by a thin p-implant. The total thickness of implant and metal will be equivalent to less than 100 nm of Si, resulting in < 10 keV of energy loss for 30 keV protons. The junction side will be featureless (see Figure 26) and will be held at ground potential. A very fine grid, consisting of 10 μm wide and 400 nm thick Al and with a spacing of 4mm, is created by photo lithography techniques to increase the conductivity of this side of the detector. The ohmic side of the detector will be segmented to form the indiviual detector elements. The design for the segmentation consists of an array of 127 hexagonal elements, each approximately 1 cm^2 in area, as shown in Figure 27. The active area of the detector extends to within 5 mm of the detector edge. In this boundary region are approximately 20 guard rings that step down the applied bias voltage evenly, grading the electric field and reducing the probability of surface breakdown.

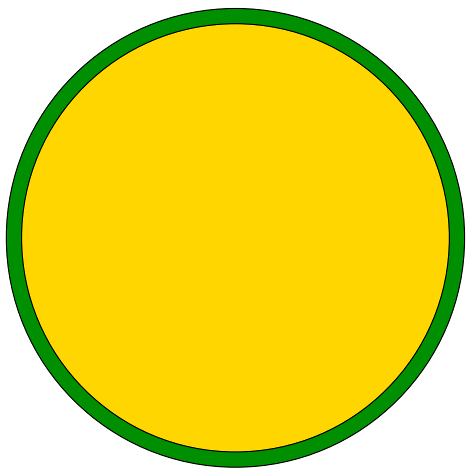

Figure 26: Design for the junction side of the detector detector. The gold area represents the thin entrance window. The green area is the electrical contact for the window, which is held at ground potential.

A hexagonal array of detector elements is chosen for several reasons.

1. Hexagons efficiently fill the circular area of the detector,
2. they match the rectangular image of the decay volume well,
3. only three detector elements meet at a vertex, reducing the number of elements involved in a charge-sharing event, and

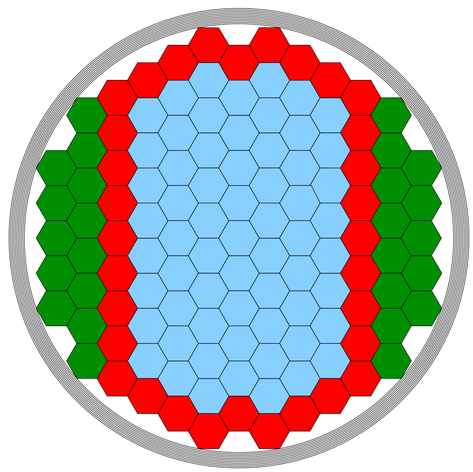

Figure 27: Design of the ohmic side of the detector. The 127 hexagons represent individual detector elements (pixels). Proton events in the interior pixels (blue) generate a valid trigger. The associated electrons are detected additionally in the surrounding pixels (red), allowing for spatial separation between the particles due to their motion in the magnetic field. The pixels to the extreme left and right (green) see only background events. The concentric circles represent the guard ring structure. Electrical contact is made to each pixel to provide the bias voltage and collect the charge deposited by incident particles. The areas between the outer most pixels and guard rings are electrically connected to form one additional channel.

4. the number of adjacent elements that must be searched for the partner particle or reflected electron events is minimized.

The hexagonal detector elements in the preliminary design have sides of length $s = 5.2$ mm and areas of $a = 0.70$ cm^2 There are several reasons for this choice. First, the maximum radius of gyration at the detector is 2.2 mm for the electrons and 2.3 mm for the protons. Therefore, the electron-proton separation on the detector can never be more than 4.5 mm. Our choice of $s = 5.2$ mm guarantees the electron is never more than one detector element away from the proton. This means that only 14 detector elements (including conjugate elements on the opposing detector) need to be considered in constructing a coincidence event. Similarly, only 14 elements need be considered in searching for an event where an electron reflects from a detector and then stops, either in the same detector or the opposing detector. The case of multiple electron reflections is discussed further in Section 4.2.8. Second, the noise gain of the preamplifier increases with detector capacitance, while the speed decreases. With our choice of $a = 0.7$ cm^2, the parallel plate capacitance of one element is approximately 6 pF. Inter-pixel capacitance and contributions from the electrical interconnects will bring the total capacitance to approximately 10 pF, which is acceptably small. Finally, the number of detector elements, 127 per detector, does not require an unacceptably large number of electronic channels.

It is important to note that, though the detector is segmented, there are no dead spaces between the detector elements. Even though there is a gap of 100 μm between the metal pads for adjacent elements, *all* charge deposited in the active volume of the detector is collected, though it may be shared among adjacent elements. This property guarantees that if a proton hits within the interior hexagons in Figure 27, the corresponding electron must hit within the active area (interior plus perimeter hexagons) of the same (or opposing) detector. This allows the use of the proton hit as a trigger. Since the protons start with a very small energy, less than 750 eV, and are accelerated to a much higher energy, 30 keV, this trigger is much less sensitive to the kinematics of the decay than an electron trigger. This technique is only practical with large-area detectors so that there are no dead areas that can spoil the coincidence efficiency, as would exist in a tiled scheme where several smaller detectors cover the same area.

A prototype detector has been constructed by Micron Semiconductor [34] that fufills all of the design criteria, with the exception of thickness. The prototype detector is 0.5 mm thick rather than the required 2 mm. The prototype is currently being tested and plans for acquiring prototypes with thicknesses of 1.0, 1.5, and 2.0 mm are in progress. Front and back photos of the prototype detector can be seen in Figure 28.

Because the magnet bore will be at 4 K, a load-lock mechanism is necessary at each end of the magnet to remove the detectors for servicing. Figure 29 shows a preliminary design for such a mechanism. The detector package, including front end electronics and cabling, is mounted to the end of a shaft driven by a linear positioner. In the extended position, the detector is correctly located within the magnet bore at its operating position. For servicing, the linear position is retracted placing the detector within a service chamber. A gate valve is closed to isolate the magnet vacuum and the detector can then be accessed or removed through a flange on the service chamber. The linear positioner ensures reproducible positioning of the detector. All components of the load-lock are non-magnetic.

Background events are an important consideration in the experiment. Background rates are difficult to estimate *a priori* as they arise from the very intense primary neutron beam, but having a low probability of producing detectable particles in the detectors. In addition, the rates depend

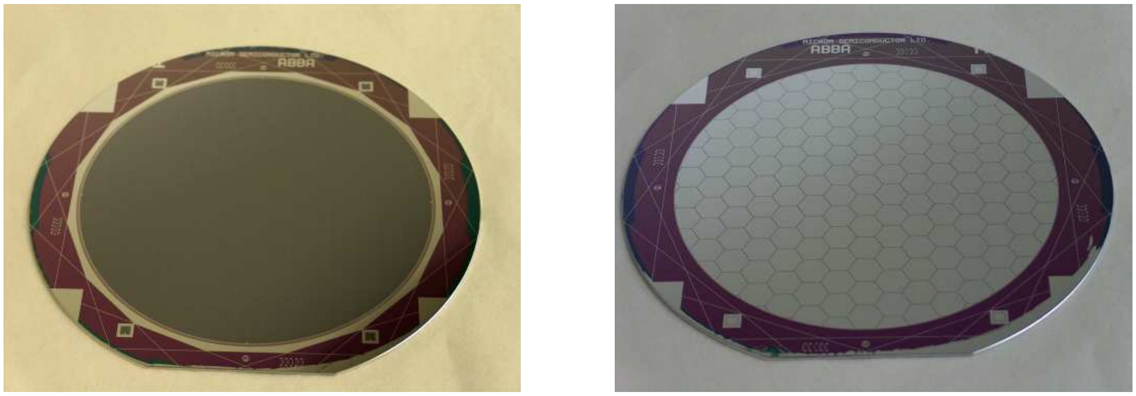

Figure 28: Photographs of the prototype abBA detector, before cutting from the 6 inch diameter silicon wafer and packaging. Charged particles enter through the junction side (left) and signals are read out from the ohmic side(right).

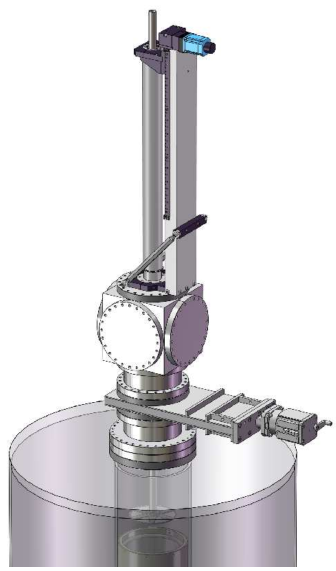

Figure 29: Prelinimary design for a detector load-lock mechanism, shown attached to the spectrometer magnet.

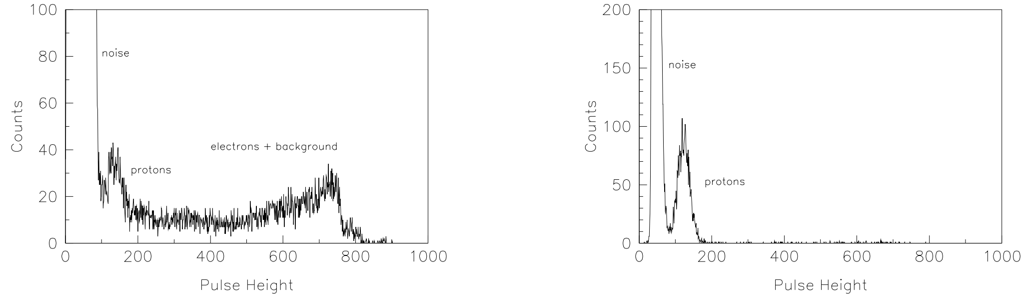

Figure 30: Plots of protons from neutron decay in singles (left) and coincidence from a test measurement at NIST. See the text for details.

sensitively on the design of the experiment, in particular the collimation system, shielding, and beam stop. These aspects of the experiment will have to be carefully optimized to reduce background. For the purposes of estimating the detector background rates, we take the experience of the NIST in-beam neutron lifetime experiment, where background rates were approximately equal to actual decay events [35].

An important feature of the abBA experiment is the detection of both proton and electron from the neutron decay in coincidence. We conducted a demonstration of this technique by observing electron-proton coincidences from neutron decay using a silicon surface-barrier detector coupled to the NIST lifetime apparatus. A 30 keV potential was used to accelerate protons. The detector area was approximately the size of one pixel of the abBA detector. The geometry was less ideal than the abBA configuration, as the detector is much closer to the neutron beam and the final collimator ($\sim$ 10 cm). Since the NIST lifetime experiment was designed to count decay protons after the neutron been was shut off, this was not a limitation for their experiment. Figure 30 illustrates the effect of coincidence on suppressing backgrounds. The left-hand plot shows the observed singles spectrum. The 30 keV proton peak can be clearly seen, as well as electronic noise, the (distorted) electron spectrum, and background events. The electron spectrum is distorted because the detector was only 300 μm thick, too thin to stop all of the electrons. The right-hand plot shows a spectrum of proton energy in coincidence with decay electrons, greatly suppressing backgrounds. Section 4.2.11 estimates the rates of false coincidences due to these backgrounds.

3.5 Data Aquisition System (DAQ)

3.5.1 Introduction

We are planning to use a DAQ based on the digital processing of the Si signals (DSP) which is described in more detail below:

A DSP based systems has been proven to have equivalent or superior functionalities to analog systems for energy and time measurements [36]. There are important advantages and unique features characterising a fully digital DAQ system:

- Digital DAQs are very stable. The signal digitizing is done early on, resulting in less noise influence.

- A Digital DAQ allows storing more complete information about the pulse as well as real time analysis.
- A Digital DAQ is much more flexible in terms of varying requirements.

The proposed experiment requires a DAQ system which does not introduce any systematical bias in the data and offers low electronic threshold and good timing resolution for 256 synchronized channels. A practical DSP expertise has been acquired recently at the ORNL Physics Division by the decay spectroscopy group running a 20-board (80-channels) system of Digital Gamma Finder modules [37]. These universal boards produced by X-ray Instrumentation Associates (XIA) have been routinely used in charge-particle and gamma spectroscopy [36], at ORNL and other laboratories. Recent results achieved thanks to the digital processing of detector signals include the discovery of new type of radioactivity (two-proton decay of ^{45}Fe [38, 39]), rare observations of fine structure in one-proton emission [40, 41] and studies of "superallowed" alpha decay of ^{105}Te [42].

3.5.2 The PIXIE-16 system

We are currently evaluating the PIXIE-16 board which is manufactured by XIA and is a improved and enhanced version of the successful PIXIE-4 system.

PIXIE-16 has the following charcteristics:

- 100 MHz, 12 bit digitizing ADC for each channel,
- 16 channels on one board, using 1 FPGA for every four channels,
- fixed, low-noise analog conditioning (selectable amplification and offset adjustment for each channel),
- FIFO memory to store pulse shapes, up to 80 μs long,
- multichannel trigger bus line, and
- based on PCI architecture which allows very high data transfer at 100 Mbytes/s

Each channel features real time processing algorithms to determine amplitude and arrival time. This analysis is using fixed width trapezoidal filters (moving average filter) with continuous baseline monitoring and correction for exponential pulse decay. On-board storage capacity will allow us to record up to 80 μs long pulses for pile-up correction and precise timing/pulse shape analysis. To instrument 256 channels of the pixelated silicon detector sixteen boards of 16-channel PIXIE-16 are needed. Additional channels will be used to digitize the reference pulses from the SNS accelerator and signals fromthe neutron beam line (eg. neutron monitors, SF signals etc).

With a predicted rate of up to 500 Hz of detected neutron decays, the amount of transferred data will be moderate (around 0.6 MB/sec), however a large amount of storage will be required.

The readout and data storage is managed by a host computer installed in the PCI chassis. The role of this central CPU will be to organize data buffers from individual cards and send the data to the storage. Additional CPUs will analyze a fraction of the data online.

The data stream consists of time stamped energies and 256 channel long traces containing a 2.56 μs section of the pulse around its rising edge. The energies will be computed with real time processing algorithms using trapezoidal filter, on the PIXIE-16.

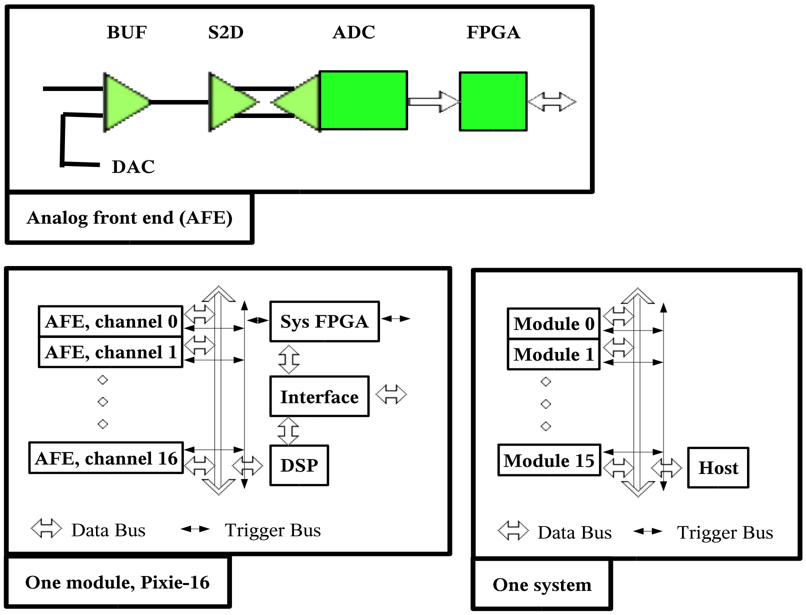

Figure 31: Overall architecture of the PIXIE-16 front-end electronics and data acquisition system. A single analog front-end channel is shown at the top of the graph. It consists of a fixed-gain two-stage amplifier, which presents the incoming signal to the waveform digitizing ADC. Each channel has its own private offset adjustment, indicated by the DAC line. An FPGA receives the data stream from the ADC and all data processing is performed digitally. The lower left panel shows how 16 channels are combined into a single-card module. A digital signal processor is used to collect and post-process data from all the FPGAs, and to format them for read out by the host computer. A fast trigger bus largely bypasses the DSP and connects the channel FPGAs to a system FPGA, which is responsible for managing triggers on board and across modules. The lower right panel shows a complete system. The host computer accesses the DSPs and possibly on board memory via the system data bus, which in the baseline implementation will be a 32 bit 33 MHz PCI bus. The fast trigger and synchronization bus interconnects the modules and requires no external electronics.

The data acquisition system will be connected to a LINUX machine with several RAID array of disks.

A simple triggering scheme based on 128 words deep FIFO has been developed. In this scheme a trigger filter of 1.28 μs length is feasible. This allows to use large integration times for triggering. The individual channel based trigger will detect preamplifier signals of very low amplitude,and the pulse shape will be recorded for the precise timing analysis, which can be done either on-board in real time or offline using more sophisticated algorithms. This triggering scheme is very simple and robust, which is an essential requirement for the proposed experiment.

Good timing resolution is necessary for the proper determination if the electron pulse was induced by a backscattered electron, or a direct electron. This is crucial for the proper angular electron-proton correlation.

There are two scenarios which we need to distinguish:

- the electron and proton hit two different detectors, and
- the electron and the proton hit the same detector.

The first case leads to the requirement for a system time resolution of better than 20 ns.

The second case does not cause any ambiguity in pixel assignment but may cause a slight degradation in the energy determination. The storage of the pulse shape will enable us to handle both scenarios.

Our studies have shown that a timing resolution of 5 ns was achieved with a 40 MHz sampling system, leading us to conlude that the 100 MHz systrem will achieve a 2 ns time resolution. Recently the time resolution tests for PIXIE-4 and PIXIE-16 [43] has been performed. The intrinsic channel to channel timing resolution has been measured to be 150 ps for PIXIE-16 board. The subnanosecond resolution has been achieved for real detector signals (fast scintillators LSO and $LaBr_3$).

In case of two interactions in the same pixel, the energy correction can be easily computed from the stored pulse shape.

3.5.3 Status of the present system

Six PIXIE-16 modules and two chassis have been acquired from XIA by UT and ORNL. A fully operating single chassis data acquisition system has been developed to be used in experiments, see Figures 32 and 31. The current development status, done mostly at UT, is as follws:

- Several problems with hardware have been identified and corrected by XIA.
- A new control system has been written using the CERN ROOT environment.
- PCI readout has been tested and DMA access has been developed allowing currently about 25 Mbyte/s transfer throughput.
- Readout software for Linux (kernel 2.4 and 2.6) using XIA libraries and PLX drivers has been written. Data read out by the front-end linux machine are tranferred over ethernet network to the analysis and storage computer.
- A complete software package has been written, which includes event builder, pulse shape analysis, correlator and histogramming.

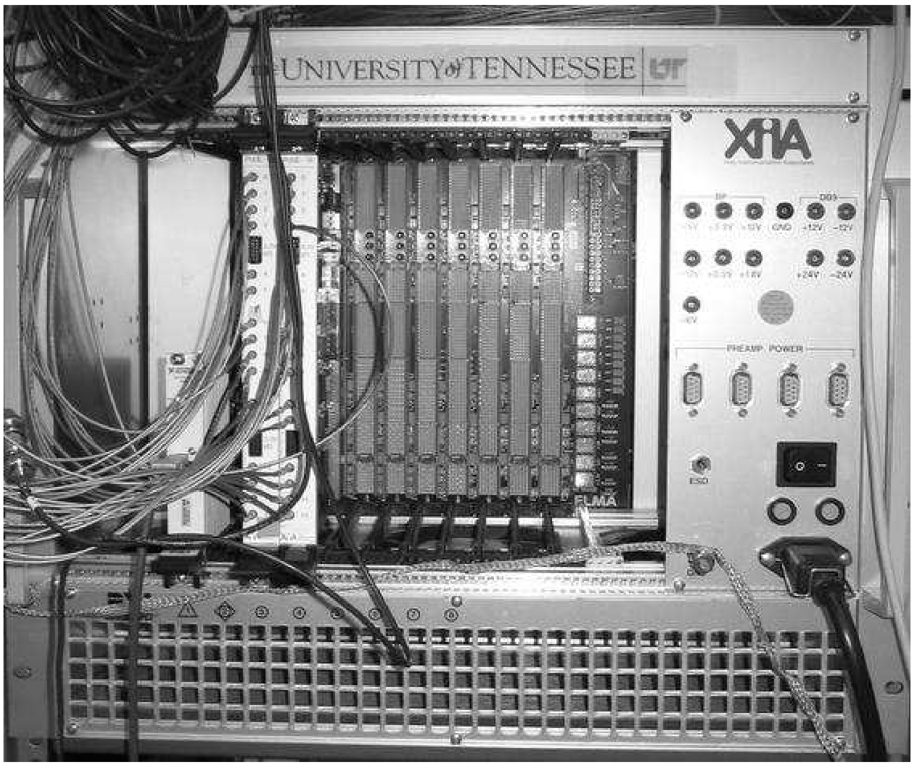

Figure 32: Two PIXIE-16 modules in the chassis during the tests at University of Tennessee.

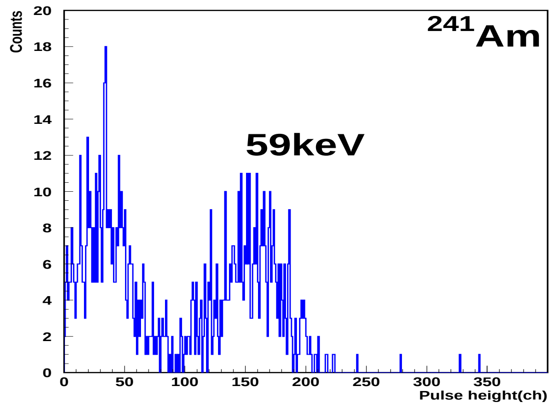

Figure 33: Gamma ray of 59 keV from ^{241}Am decay, detected in 1.5 mm silicon detector at room temperature .

- A system with 6 modules has been succesfully used at NSCL MSU for the experiment, lasting about two weeks.
- A low threshold triggering scheme has been developed at XIA and tested at UT with Double-Sided Silicon Strip Detectors and pulser and sources. The system allowed to detect 59 keV ^{241}Am gamma line in 1.5 mm room-temperature silicon detector, see Figure 33.

3.5.4 Outlook

We have shown that we have a viable DAQ solution, which will allow us to do the experiment. However, because of the time frame of this proposal, higher resolutin and faster digitizers will become available. We will continue to study alternative solutions, like a VME based data aquisition system and will make a decision about the final system based on performance, price and effort needed.

3.6 Neutron Beam

The observed rate of neutron depends upon the average number of neutrons in the decay volume of the detector. Hence, one desires a neutron beam with a very high average density. Beams of cold neutrons from high flux reactors and spallation sources provide the highest time averaged neutron densities available at any source.[2]

Our method of absolute neutron polarimetry using ^{3}He requires access to a pulsed neutron source. Currently Flight Path 12 (FP12) at the Manuel Lujan Center at Los Alamos is the only cold, pulsed, neutron beam in the world that is available for neutron nuclear physics. In $\sim$ 2008 a new beamline,

[2]Even with recent advances in UCN source technology the density of neutrons in a cold beam is more that 2 orders of magnitude higher.

the FnPB, at the SNS will become operational and be available for nuclear physics experiments. Except for the much higher power of the SNS, and the concomitant increase in cold source brightness, the beam characteristics of the SNS will be quite similar to those of the Lujan Center, which has recently been measured quite precisely [44]. Section 3.6.1 gives a detailed estimate of the decay rate expected. This estimate includes a number of effects which are not relevant to the unpolarized experiment such as transmission through the ^{3}He cell, divergence losses during passage through the spin flipper as well as several window losses. A conceptual plan view of the experimental apparatus at the SNS Flight Path 13 facility is shown in Figure 34.

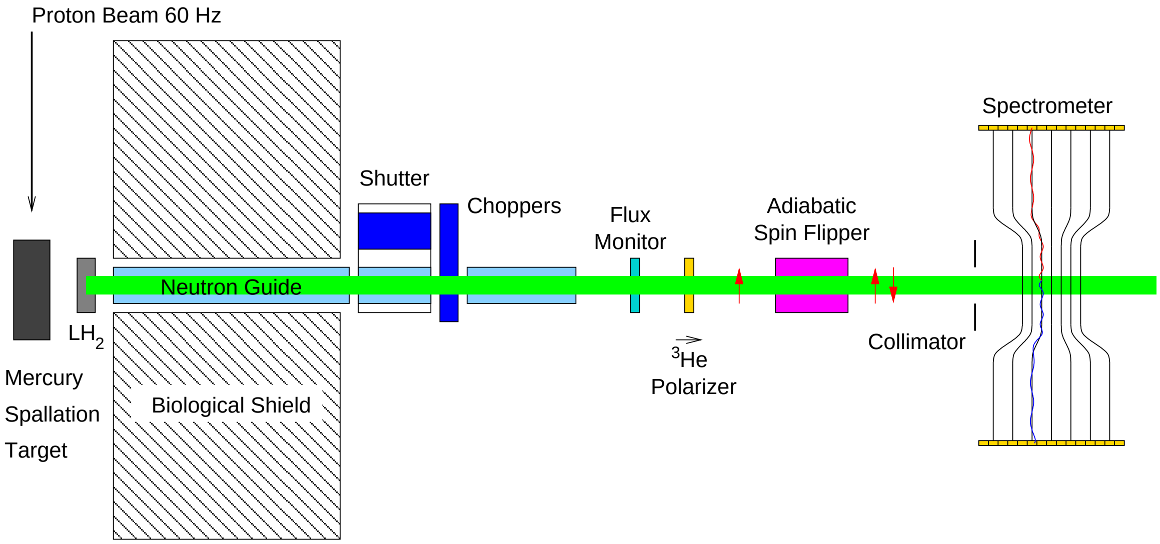

Figure 34: Conceptual plan view of the SNS Flight Path 13, showing the proposed experimental apparatus.

3.6.1 Neutron Beam Layout

The preliminary layout of the apparatus is shown in Figure 34. The beam from the FnPB neutron guide is polarized by a ^{3}He polarizer, and then passes through a spin flipper before entering the spectrometer. Magnetic field coils provide holding fields for the polarized ^{3}He and transport the neutron spins into the spectrometer. A flux monitor provides continuous monitoring of the neutron flux exiting the guide.

Much of the geometry is determined by the end of the FnPB neutron guide and the location of the magnetic spectrometer pit. The fiducial decay volume is determined by the image area on the silicon detectors, equivalent to an area of 9.7 cm^2 in the decay region, and an estimate of the neutron beam height (extent in the vertical direction) in the spectrometer. The beam height was estimated by comparing magnetic field profiles as a function of coil separation at the extreme edges of the fiducial area, and requiring that the field drop monotonically from the midplane. This procedure established a maximum coil gap, which allows a 6 cm high neutron beam to pass. This value will have to be refined by careful calculation of the correction required due to electron reflection by field

P_3	nl (atm·cm)	λ ($\mathring{A}$)	N_0 (Hz)	N (Hz)	P_n
55%	12.89	2.11–5.75	26.0	19.2	95.4%
70%	9.36	2.33–5.96	53.2	40.5	96.1%
85%	7.27	2.54–6.16	74.6	56.9	96.3%
No Polarizer	0.	1.798–5.436	230.1	187.3	0.

Table 2: Calculated neutron decay rates for three values of ^{3}He polarization P_3 and corresponding thicknes nl. λ is the range of neutron wavelengths transmitted by the choppers. N_0 and N are the neutron decay rates from the fiducial volume without and with beam collimation. P_n is the average neutron polarization.

gradients, but is not expected to change much. The fiducial volume is then taken to be 58 cm^3 for the counting rate estimates.

The decay rates were calculated using the MCSTAS neutron transport code. Two neutron choppers were assumed, at locations indicated on the figure. Calculations were performed for three values of ^{3}He polarization, with ^{3}He thickness adjusted to give approximately 95% average neutron polarization. For each calculation, chopper phases were chosen to optimize a figure-of-merit $P_n^2 N$, where P_n is the average neutron polarization and N is the decay rate. A collimator is placed 10 cm before the center of the spectrometer and its size is adjusted to keep the fraction of neutrons outside of the desired fiducial volume less than 10^{-4}. Although such a conservative collimation is not required, the range of counting rates given in that limit N and the limit of no collimation N_0 gives a reasonable estimate of achievable decay rates. Table 2 shows the estimated neutron decay rates for these conditions. A ^{3}He polarization of 55% has been demonstrated in the NPDGamma experiment [45]. Further improvements in achievable ^{3}He are being pursued. We assume 70% will be obtained for abBA and use 40 Hz as estimate for the decay rate in the sections that follow.

3.6.2 Neutron Beam Choppers

The phasing of the choppers and selection of the neutron energy range was optimized using a Monte Carlo calculation based on the McStas neutron optics code, as explained in Ref. [46]. Neutrons were generated in the liquid hydrogen moderator source and propagated ballistically through the end of the guide, resulting in a ROOT ntuple of weighted neutron events specifying the complete state $(t, \vec{x}, \vec{v})$ at the end of the guide, as phase information where it crossed each chopper. This ntuple was analyzed repeatedly to simulate the figure of merit of the experiment, $P^2 \cdot N$, as a function of chopper, collimator, ^{3}He cell parameters, to find the optimal values.

Two backgrounds were monitored to ensure acceptable levels: a) wrap- around neutrons, which would produce an error in the measurement of the polarization P, and b) neutrons making it outside of the decay volume which produce background radiation. The chopper and collimator settings were adjusted to keep each of these at the level of 10^{-4} [47].

3.7 Neutron Polarization

To reach the goal precisions in the correlations A and B, the experiment requires the highest available fluence of cold neutrons with high polarization, which has to be determined with the uncertainty of less than 10^{-3}.

For neutron polarization we are using polarized ^{3}He spin filters which is a well established technology. However, the requirements for the abBA experiment are approaching the present limits of this technology and therefore some development is needed as compared for instance to the performance achieved with spin filters in the NPDGamma experiment, which had a long production run in 2006 in the 1FP12 at LANSCE. In addition of the NPDGamma the members of the collaboration have used ^{3}He spin filters in numerous other experiments and some of the members are leading experts in this field [48, 49, 50]. Although the ^{3}He spin filters are planned to be used for the abBA experiment, we are also following the development of the supermirror polarizer technology, which has made some progress lately with remanent and cross supermirror polarizers [51].

The ^{3}He spin filters are based on the large spin-dependent neutron absorption cross section $\sigma(v)$ on ^{3}He, which has a well known $1/v$ behavior with $\sigma(v) = \sigma(v_0)(v_0/v)$ [52]. Since the only open channel in capture is $J^\pi = 0^+$ (the singlet spin state) thus a polarized ^{3}He cell filters the neutron spin state which is opposite to the ^{3}He polarization direction. The well known energy dependence of the absorption cross section and a possibility to define accurately the neutron energy through a time of flight (TOF) measurement enables the determination of the absolute neutron beam polarization [49].

The polarization of a neutron beam transmitted through a polarized ^{3}He gas cell is

$$P_{\mathrm{n}}(v) = \tanh\left(P_3 nl\sigma(v)\right) = \tanh\left(\frac{P_3 nl\sigma(v_0)v_0}{L}t\right) = \tanh\left(\frac{t}{\tau}\right), \tag{12}$$

where $P_{\mathrm{n}}(v)$ is the neutron polarization, P_3 is the ^{3}He polarization, n is the ^{3}He number density in the cell, l is the thickness of the ^{3}He gas in the cell, $\sigma(v_0) = 5333 \pm 7$ barn is the spin averaged capture cross section at neutron velocity $v_0 = 2200$ m/s (corresponding to the neutron energy of 25.3 meV) [53, 54], L is the distance from the source to the experiment and t is the TOF.

Neutron transmission of a polarized ^{3}He cell is

$$T(v) = T_0(v)\cosh\left(\frac{t}{\tau}\right), \tag{13}$$

where $T_0(v)$ is the transmission of the unpolarized ^{3}He. A measurement of the ratio $T(v)/T_0(v)$ determines the single instrumental parameter τ which is then used to extract a beam polarization from Equation 12.

3.7.1 Neutron Beam Polarizer

The figure-of-merit (FOM) of the ^{3}He spin filter in the neutron β- decay experiment is $T_{\mathrm{n}}(v)P_{\mathrm{n}}^2(v)f(v)\Phi(v)$ where $f(v)$ is the neutron decay probability in the spectrometer and $\Phi(v)$ is the normalized shape of the neutron pulse. The maximum of the FOM defines a value of the τ-parameter which determines an optimum ^{3}He thickness for a given ^{3}He polarization. Since the measurements of the A and B correlations are statistics limited, the diameter of the ^{3}He spin filter cell is selected to fully match the phase space (position and angle) of the 10×12 cm^2 neutron guide in the FnPB and thus gives maximum illumination on the decay volume. This requires the cell diameter to be 10-12 cm, which is the size of the cells that were used in the NPDGamma experiment at LANSCE. After the spin filter the beam will be gradually collimated for the decay volume by a carefully designed collimation system that minimizes backgrounds.

The polarizer will be operated next to the strong spectrometer magnet at a field of 50–100 G , which is higher than the 10–40 G fields used typically within polarized ^{3}He systems. A strong field can reduce the polarization relaxation time of ^{3}He in a cell [55], however, preliminary tests indicate that the relaxation may be affected only at fields of a few hundred gauss and therefore, polarization relaxation time is not expected to be an issue for the less than 100 G field in which the abBA polarizer will reside. Investigation of the strong field effect on the ^{3}He polarization is in progress at NIST [56].

The NPDGamma experiment observed a loss of the ^{3}He polarization as a function of the neutron beam during its production run in 2006. Further studies of this phenomenon were performed in a dedicated experiment in 1FP12 at LANSCE in the summer of 2007. Preliminary results indicate that there are two kind of effects that cause a reduction in ^{3}He polarization, a difference is the response time to beam. The short-term effect is related to the optically pumped Rb polarization reduction with neutron beam intensity. The ^{3}He polarization is effected since Rb polarizes the ^{3}He through spin exchange. The long-term effect is due to a slow build up on the inside walls of the cell that prevents the transmission of laser light and thus reduces the Rb polarization [57, 58]. The long-term effect depends on time integrated beam on the cell. Since the beam intensity in the FnPB is expected to be about 10 times higher than in 1FP12, the reduction of the ^{3}He polarization by beam would be a serious problem and has to be addressed. One of the possible solutions is to have a spin filter system where the spin exchange optical pumping (SEOP) cell and the neutron spin filter cell are separated. In the double cell geometry a several inches long glass tube connects the two cells and the ^{3}He polarization from the SEOP cell is driven to the filter cell by spin diffusion. SEOP double cells have been intensively operated at SLAC and lately at JLab with high intense electron beams [59, 60].

Our collaboration has also experience with SEOP double cell spin filters since originally it was planned to use double cells for the NPDGamma experiment as well. Indeed, NIST pursued an extensive program of developing such double cells and a few of them were constructed and tested in a beam at LANSCE.

An alternative approach for the double cell geometry would be to apply a gas polarizing platform originally developed for medical ^{3}He imaging [61]. In this system ^{3}He gas is continuously polarized by strong lasers in the SEOP volume of the platform and circulated between SEOP cell and a spin filter cell by a pump.

The accuracy of the polarization in the abBA experiment requires that the ^{3}He thickness in the spin filter cells is uniform and thus the cells cannot be of the blown type such as the ones used by the NPDGamma experiment. However, the relaxation times obtained in flat-windowed cells constructed lately at NIST are typically lower than in blown cells, limiting the achievable polarization. NIST is further investigating techniques to reliably obtain long lifetimes in flat-windowed cells. An interesting possibility is to use silicon windows which have been successfully employed at the ILL [62]. Compared to glass windows, silicon exhibits much less neutron scattering, leading to lower backgrounds and higher neutron transmission. NIST is also working with Si window cells.

Other interesting technologies for the abBA experiment which are under investigation and development, are optical pumping with spectrally narrowed lasers and use of mixtures of K/Rb in SEOP cell instead of pure Rb. At NIST, ^{3}He polarizations up to 75% have been achieved with spectrally narrowed lasers [50, 63, 64]. In fact, a single bar spectrally narrowed diode laser was used in the NPDGamma experiment to polarize the analyzer cell up to 60% [65]. The use of the "hybrid" Rb/K mixture approach to SEOP provides a substantial increase in the efficiency to reach the highest possible polarization, especially if the double cell geometry is used [63].

3.7.2 Precision Neutron Polarization

One of the largest systematic error in the previous polarized neutron β- decay experiments has been the neutron beam polarization [66]. Only with auxiliary measurements the previous experiments have achieved the necessary accuracies in the polarization. We aim to determine the polarization of the decaying neutrons to the level of $\Delta P_n/P_n \leq 1 \times 10^{-3}$. This high accuracy can be achieved by using ^{3}He spin filters, determining accurately the neutron energy by TOF measurement, and studying sources of systematic errors in dedicated experiments. The collaboration has initiated a program to study precision polarimetry in 1FP12 at LANSCE to establish techniques and define the upper limit for the neutron polarization accuracy with ^{3}He spin filters (section 4.2.12).

A unique advantage of the pulsed spallation neutron source for studies of correlations in neutron β-decay is that the neutron polarization produced by a ^{3}He spin filter can be measured, in at least, three different ways, with high precision and simultaneously with the correlation coefficient asymmetry measurements.

A conceptual design of the setup for the experiment utilizing ^{3}He spin filters is shown in Figure 35. The ion chamber beam monitors (M1 and M2) allow the measurement of the relative neutron transmission $T(v)/T_0(v)$ through the polarized and unpolarized ^{3}He spin filter cell as a function of TOF, from where the parameter τ of Equation 13 can be obtained from a fit and then the beam polarization is obtained from Equation 12. A limiting factor of this method has turned out to be the accuracy of the fit of the $\cosh(\tau/t)$ to the measured $T(v)/T_0(v)$ data set. The ratio is sensitive to monitor backgrounds and system drifts especially when the polarized and unpolarized transmission measurements can be several days apart. These effects will distort the shape of the ratio and prevent an accurate determination of τ [49].

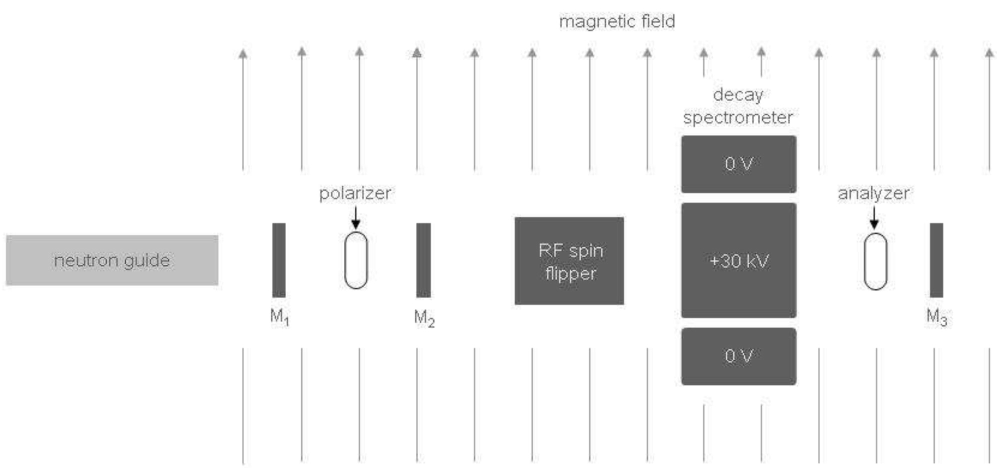

Figure 35: Setup of the abBA experiment with ^{3}He spin filter polarizer and analyzer.

The relative transmission method has been used earlier to measure absolute neutron polarization in a dedicated but statistics limited measurement to an accuracy of 0.3% at neutron energies from 40 meV to 10 eV [48]. Present knowledge of the $n-{}^3$He interaction indicates that the velocity dependence of the absorption cross section holds to the 10^{-4} level at lower energies and can thus be used for a precision neutron polarimetry technique at cold (<25 meV) neutron energies to achieve the accuracy level of 10^{-3} or better in polarization.

The second independent method to determine the beam polarization is the use of the adiabatic RF spin-flipper and the analyzer cell in combination with the third monitor M3 [67].

A third method to determine the polarization of the decay neutrons in the abBA experiment is making use of the fact that since the spin-dependent β-decay correlations A and B do not depend on neutron energy, the TOF dependence observed in the experimental asymmetries ϵ_A and ϵ_B is due entirely to the TOF dependence on the neutron polarization. Performing a two parameter fit to the experimental asymmetry ϵ_B, allows extraction of both B and τ. The extracted value of τ can then be used to analyze the asymmetry ϵ_A to obtain A. Since $B \sim 1$ is larger than $A \sim -0.1$, neutron statistics are optimized in this procedure [68]. In addition, the neutrons used in this polarization determination method are *the same neutrons* used in the correlations measurement, which is a significant advantage over the polarization determination by relative transmission measurements or use of an analyzer.

Sources of systematic effects in the determination of the beam polarization are discussed in section 4.2.12.

3.7.3 Adiabatic RF Neutron Spin Flipper

In all previous cold neutron asymmetry experiments, the neutron spin has had only one method of modulation, namely by virtue of a spin flipper, between spin-up and spin-down. The use of the ^{3}He spin filter offers an additional spin reversal, since the ^{3}He polarization direction can be simply reversed by adiabatic fast passage (AFP). This spin reversal gives an extra handle for studying systematic effects in the experiment.

Since the two flight paths of the spectrometer and the Si detectors cannot be absolutely symmetric, we need to switch their positions with respect to the beam polarization by frequently (60 Hz) reversing the polarization direction. For near 100% spin reversal at all neutron energies we will use an adiabatic RF spin flipper which has a longitudinal RF field $\vec{B}(z,t) = \hat{z}B_1(z)\sin(\omega t)$ with amplitude distribution along the oscillating field $B_1(z) = A\sin(\pi\frac{z}{d})$, $0 \le z \le d$. The RF field is perpendicular to a vertical static field with a small gradient, $\vec{B}_0(z) = \hat{y}\left[B_0 + A\cos(-\pi\frac{z}{d})\right]$. Here B_0 is the strength of the field at $z = d/2$ when d is the length of the RF field. The amplitude of the modulation is selected so that $A = B_0(0) - B_0(z = d/2)$. Within this sine-cosine modulation the amplitude of the effective field in the rotating coordinate system is constant

$$\left|\vec{B}_{\text{eff}}(z)\right| = \left|\hat{y}\left(\vec{B}_0(z) - \frac{\hbar\omega}{\mu_{\text{n}}}\right) + \hat{z}\vec{B}(t)\right| = A \tag{14}$$

when the neutron passage through the flipper. Also this harmonic modulation allows an analog solution for the precession equation:

$$\frac{\mathrm{d}\vec{\sigma}}{\mathrm{d}t} = \frac{\mu_{\text{n}}}{\hbar}[\vec{\sigma} \times \vec{B_{\text{eff}}}(z)]. \tag{15}$$

In the rotating frame the neutron spin precesses about the local effective field $\vec{B_{\text{eff}}}$ which, as seen by the neutron spin, slowly varies from transverse up $+\hat{y}$-direction as the beam enters the flipper to longitudinal in the middle of the flipper and finally transverse down at the exit of the flipper. If the polarization direction of the ^{3}He is reversed also the sign of the gradient has to be changed. As long as the precession frequency ω_0 of the neutron spin in this rotating frame about this slowly-varying effective field is fast compared to the rate of change of the direction of the effective field, then the projection of the neutron spin onto the effective field is an adiabatic invariant and the spin follows the effective field with high accuracy.

For the spin reversal the RF frequency ω has to be selected so that in the middle of the flipper the neutron spin will have the resonance condition $\omega = \omega_0 = (\mu_{\rm n}/\hbar)B_0$. Every neutron traveling through the spin flipper will meet this condition independently if they are moving on or off axis because of the gradient field. In addition of the resonance condition, the neutron spin has also to fulfill the adiabaticity condition $\lambda = \omega_0/\omega_{\rm B} >> 1$, where $\omega_{\rm B}$ corresponds to the rotation rate of the effective field when the neutron spin passes the spin flipper. The derivation of λ is given in section 4.2.1.

The spin flipper has two states: 1) flipper off-state, where the RF field is off and the neutron polarization direction is not changed and 2) flipper on-state, where the RF field is on and the beam polarization direction is adiabatically reversed. The right selection of the field gradient keeps depolarization negligible level (see section 4.2.1). For the flipper on-state, the adiabaticity parameter λ is constant for neutrons with velocity v,

$$\lambda = \omega_0/\omega_{\rm B} = \frac{\left(\frac{\mu_{\rm n}}{\hbar}A\right)}{\left(\frac{\pi v}{d}\right)}. \tag{16}$$

In a general case the adiabaticity parameter $\lambda(z, v)$ is given in Equation 58. The neutron spin depolarization in the spin flipper when the RF field is on, is discussed in section 4.2.1. In the context of the spin reversal, 1-depolarization gives the spin flip efficiency. According to the section 4.2.1, if $\lambda = 6$ or larger the depolarization is less than 1.6×10^{-4} and the the spin flip efficiency is larger than 99.98%.

The adiabaticity condition is not difficult to meet at slow neutron energies and such a spin flipper is relatively easy to realize [69, 70, 71].

Since the adiabatic RF flipper by necessity possesses a static magnetic field gradient, the Stern-Gerlach steering will deflect the neutron beam in slightly different directions for the two spin states, however this will not affect the neutron polarization determination (section 4.2.12). Finally, depending on the sign of $\vec{\mu}_{\rm n} \cdot \vec{B}_0$, the kinetic energy of the neutron passing through the spin flipper is slightly decreased or increased by the gradient in the level of $\Delta v/v \sim 10^{-8}$ and because of the size the effect can be ignored.

3.8 Decay Event Simulation

The abBA/Nab magnetic spectrometer Monte Carlo (MC) simulation uses the industry-standard GEANT4 detector simulation toolkit [72]. We have installed the latest version of the code (GEANT 4.9.0) on a 30-node Linux cluster running CentOS operating system. These computers use quad Xeon 3 GHz processors.

The high voltage electrodes potential is calculated with the SIMION-3D [73], while the common abBA/Nab magnet is modelled with OPERA-3D [74]. The electromagnetic field in GEANT4 is specified as the six-dimensional array with field map step sizes of 1 mm. In charged particle tracking the field values at the current particle position are calculated by the linear interpolation from eight neighboring field values.

Our program can simulate an arbitrary polarized neutron beam with user-defined beam profiles. The calculation also handles a spin procession of cold neutrons in the apparatus. The neutron beta decays with a nucleon recoil are generated for the matrix element with correlation parameters a, b, A, B, and D. We are planning to include the radiative corrections soon.

The passive parts of the spectrometer are: (i) an iron solenoid magnet producing the non-uniform magnetic field, (ii) one inner and two outer electrodes producing the accelerating electric field, and (iii) 10^{-8} torr Hydrogen vacuum. We have defined two sensitive silicon detectors, 2 mm thick and 162 mm in diameter.

In the electromagnetic field the maximum propagation step size of e^-/p's is limited by user to 0.1 mm. The precision of the integration driver is set to be better then 0.01 mm.

For each simulated neutron beta decay event we record: (i) neutron decay vertex coordinates, (ii) neutron spin, (iii) momenta components of the final state electron, proton and neutrino, (iv) first timing, energy deposition and hit coordinates of the proton in Si detector, (v) up to three timings, energy depositions and hit coordinates for original/back-scattered electron in Si detectors, and (vi) any energy depositions in the passive detector elements. The simulated data are stored as ROOT Trees in the root files [75].

In the simulation "replay" analysis timing hits and the detector energy depositions are converted into the TDC/ADC pairs. The hit coordinates are converted into hit detector pixels. The timing is smeared with energy-dependent rms timing resolution (1 ns at 100 keV). The energy deposition values are smeared by the 2 keV rms resolution of the Si detectors. We are planning to include the precise time structure of the cold neutron beam, incorporating the accidental backgrounds into the simulated data soon.

4 Experimental Uncertainties

4.1 Statistical Sensitivity

In the following, we express all statistical error estimates in terms of the standard deviation σ. As is common in high count rate experiments, σ will be proportional to $N^{1/2}$, where N is the total number of counts. We define a sensitivity factor k by $\sigma = kN^{1/2}$. In an experiment where statistical correlation between two kinematic vectors is to be determined (e.g. a, A, or B), k will depend sensitively on the degree to which the experimental method provide complete kinematic information about each event. In the limit where this information is perfect, and where the correlation is of order unity, one expects $k \approx 1$. Imperfection in the kinematic information (due, for example, to finite detector resolution or solid angle detection) will imply that $k > 1$.

The addition of knowledge of the neutron polarization not only provides for the determination A and B, it also slightly improves the sensitivity factor for a. As one would expect, the sensitivity factors depend on the neutron polarization. For an assumed average neutron polarization of 96%, the statistical sensitivity factors are:

$$\sigma_a\sqrt{N} = 2.4, \quad (17)$$
$$\sigma_A\sqrt{N} = 2.8, \quad (18)$$
$$\sigma_B\sqrt{N} = 3.2, \quad (19)$$
$$\sigma_b\sqrt{N} = 7.5, \quad (20)$$

It is important to recognize that these measurements are slightly correlated. Including this correlation and assuming the Standard Model dependences on λ, one obtains an overall sensitivity factor of:

$$\sigma_\lambda\sqrt{N} = 7.4. \quad (21)$$

With the anticipated count rate of $\sim$ 40 polarized neutron decays per second at the SNS , and assuming a DF of 90 % for each the machine and the experiment t his will result in 32 Hz effective rate, one will obtain $\sim 5.8\times10^8$ decays in 5000 hours (one run cycle) of data collection. This implies the following statistical errors:

(22)

Uncertainty	Design Goal	PDG 2006 value	PDG 2006 error
$\sigma_a \approx 1\times10^{-4}$	$\sigma_a/a \approx 1\times10^{-3}$	-1.03	4×10^{-2}
$\sigma_A \approx 1.2\times10^{-4}$	$\sigma_A/A \approx 0.8\times10^{-3}$	$-.1173$	1.1×10^{-2}
$\sigma_B \approx 1.3\times10^{-4}$	$\sigma_B/B \approx 1.4\times10^{-4}$	.981	4.1×10^{-3}

In these estimates, it is assumed that a and b are measured at the same time as A and B. That is, the ^{3}He polarizer is in place, even though a and b don't require a polarized beam. As discussed in Section 3.6.1, substantially higher counting rates can be achieved with the polarizer removed.

These statistical errors are all substantially less than the *total errors* quoted by the PDG. Assuming the Standard Model relations and included the effects of correlations we find that such a measurement would give a (statistical only) error on $\lambda = g_A/g_V$ of:

(23)

Uncertainty σ_λ	Design Goal σ_λ/λ	PDG 2006 value	PDG 2006 σ_λ/λ
$\approx 3.1\times10^{-4}$	$\approx 2.4\times10^{-4}$	-1.2695	2.3×10^{-3}

Again, we emphasize that the total error will include systematic effects. We conclude from this analysis that, not only do we expect that counting time will not be a serious issue, but also that the statistical reach of the experiment will allow the opportunity to fully explore possible systematic effects.

4.2 Summary of Systematic Effects

Table 4.2 gives a summary of systematic effects. These effects are described and considered in more detail in the following sections. The estimated size of the correction is given, as well as the estimated contribution to the total uncertainty for each measured decay parameter. In cases where the correction varies among decay parameters, the largest case is given. When the contribution to the uncertainty is estimated to be $< 10^{-4}$, it is simply listed as such. In two cases, marked by †, the listed correction is a goal for the experiment. We believe this goal is achievable, but requires further

		Contribution to Uncertainty			
Systematic	Correction	δa	δb	δA	δB
n depolarization (B fields)	2×10^{-4}	0	0	$< 10^{-4}$	$< 10^{-4}$
n depolarization (windows)	3×10^{-7}	0	0	$< 10^{-4}$	$< 10^{-4}$
n pulse width	2×10^{-3}	0	0	$< 10^{-4}$	1×10^{-4}
β-delayed n's	1×10^{-4}	0	0	$< 10^{-4}$	$< 10^{-4}$
B field inhomogeneity	3×10^{-3}	$< 10^{-4}$	0	3×10^{-4}	3×10^{-4}
E field inhomogeneity †	1×10^{-4}	$< 10^{-4}$	0	0	$< 10^{-4}$
Misalignment	‡				
e backscatter	‡				
p backscatter	7×10^{-4}	$< 10^{-4}$	0	0	0
p TOF	‡				
Rate effects	7×10^{-5}	$< 10^{-4}$	$< 10^{-4}$	$< 10^{-4}$	$< 10^{-4}$
n polarization	4×10^{-2}	0	0	5×10^{-5}	5×10^{-4}
SF efficiency	2×10^{-4}	0	0	$< 10^{-4}$	$< 10^{-4}$
Detector efficiency	$< 10^{-4}$	$< 10^{-4}$	$< 10^{-4}$	$< 10^{-4}$	$< 10^{-4}$
Detector timing	‡				
Detector E resolution	$< 10^{-4}$	$< 10^{-4}$	$< 10^{-4}$	$< 10^{-4}$	$< 10^{-4}$
Residual gas scattering	‡				
Stern Gerlach	3×10^{-4}	$< 10^{-4}$	$< 10^{-4}$	$< 10^{-4}$	$< 10^{-4}$
Detector E calibration	$< 10^{-3}$	$< 10^{-4}$	$< 10^{-4}$	$< 10^{-4}$	$< 10^{-4}$
Particle trapping †	$< 10^{-4}$	$< 10^{-4}$	$< 10^{-4}$	$< 10^{-4}$	$< 10^{-4}$

Table 3: Estimated corrections from systematic effects and their contributions to the total uncertainties for each decay parameter.

R&D to demonstrate. In a few cases, marked by ‡, the correction depends sensitively on the actual experimental conditions and must be calculated in a detailed simulation. We believe these effects to be small (see the corresponding sections that follow), and are pursuing the required simulations. In addition, experimental verification will be performed.

4.2.1 Neutron Depolarization in Magnetic Fields

In this section we derive a formula describing the depolarization of a neutron that passes through an inhomogeneous magnetic field. We then use the formula to estimate the depolarization of neutrons in the fringe field of the spectrometer magnet and in a radio frequency adiabatic spin flipper. We are interested in calculating the polarization of a neutron that initially has its spin pointing along the direction a magnetic field. As the neutron moves through space, the field direction and magnitude may change. We develop approximate expressions for the spin wave function and the projection of the neutron spin on the field after the neutron position has changed.

Schrodinger's equation for the neutron spin wave function ψ is

$$i\hbar \frac{d\psi}{dt} = -\frac{\mu}{2} \left(\vec{B} \cdot \vec{\sigma} \right) \psi \tag{24}$$

Apply a rotation of the coordinate system R to Schrodinger's equation such that the new z, z''' is along $\vec{B}$

$$\left(R\frac{d\psi}{dt}+\frac{dR}{dt}\psi\right)-\frac{dR}{dt}R^\dagger R\psi=\frac{i\mu}{2\hbar}R\left(\vec{B}\cdot\vec{\sigma}\right)R^\dagger R\psi, \tag{25}$$

$$R\left(\vec{B}\cdot\vec{\sigma}\right)=B\sigma_z. \tag{26}$$

$\chi=R\psi$ is the spin wave function in the rotating coordinate system and

$$\frac{d\chi}{dt} = R\frac{d\chi}{dt}+\frac{dR}{dt}\psi \tag{27}$$

$$= \frac{i\mu B}{2\hbar}\sigma_z\chi+\frac{dR}{dt}R^\dagger\chi. \tag{28}$$

The last term comes from the time dependence of R.

Next we construct the operator R. Representing the magnetic field in polar coordinates

$$B_x = B\sin\theta\cos\phi, \tag{29}$$

$$B_y = B\sin\theta\sin\phi, \tag{30}$$

$$B_z = B\cos\theta. \tag{31}$$

The most general transformation that aligns z along $\vec{B}$ can be written using the Euler angles ϕ, θ, and λ. The transformation is

$$R = UTS, \tag{32}$$

$$S = e^{-i\phi\sigma_x/2}, \tag{33}$$

$$T = e^{-i\theta\sigma_y/2}, \tag{34}$$

$$U = e^{-i\lambda\sigma_z/2}. \tag{35}$$

The transformation R is not unique. The product of the first two transformations aligns z'' along $\vec{B}$. Any value of λ can be chosen and z''' will be along $\vec{B}$. A convenient choice for λ is given by the requirement that the precession rate about z''' be the Larmor frequency $\omega=\mu B/\hbar$, then

$$\frac{dR}{dt}R^\dagger=i\frac{\sigma_x}{2}\left(\frac{d\theta}{dt}\cos\lambda-\frac{d\phi}{dt}\sin\lambda\sin\theta\right)+ \tag{36}$$
$$i\frac{\sigma_y}{2}\left(\frac{d\theta}{dt}\sin\lambda+\frac{d\phi}{dt}\cos\lambda\sin\theta\right)+i\frac{\sigma_z}{2}\left(-\frac{d\lambda}{dt}+\frac{d\phi}{dt}\cos\theta\right).$$

In order that the precession rate about z''' be ω,

$$\lambda=\int\frac{d\phi}{dt}\cos\phi\,dt. \tag{37}$$

Schrodinger's equation in the new coordinate system is

$$\frac{d\chi}{dt} = \frac{i}{2}\left(\omega\sigma_z+\sigma_x\delta+\sigma_y\epsilon\right)\chi \tag{38}$$

$$\epsilon = \frac{d\theta}{dt}\cos\lambda-\frac{d\phi}{dt}\sin\lambda\sin\theta \tag{39}$$

$$\delta = \frac{d\theta}{dt}\sin\lambda+\frac{d\phi}{dt}\cos\lambda\sin\theta \tag{40}$$

This equation describes the motion of the neutron spin in a coordinate system for which the z''' axis points along the field direction. In this system the spin processes about an axis, which points along the direction

$$\frac{1}{\sqrt{\delta^2+\epsilon^2+\omega^2}}\left(\delta\hat{x}+\epsilon\hat{y}+\omega\hat{z}\right). \tag{41}$$

δ and ϵ are linear combinations of the rates of change of the field direction. If the rate of change of the field direction is small compared to the Larmor frequency, then the projection of the spin on the field direction is approximately conserved. In this sense, the projection of the neutron spin on the field direction is an adiabatic invariant. Much more can be deduced concerning the degree to which the projection is conserved.

Next we solve Schrodinger's equation using first order time dependent perturbation theory and investigate the degree to which the projection of the spin is conserved. Not only the smallness of δ and ϵ is important, the continuity or smoothness of these quantities and their time derivatives is important. If the first n derivatives of the time rate of change of the Euler angles are continuous then the projection of the spin is conserved to order $1/\omega^{2(n+1)}$. If all derivatives are continuous, then the deviation of the projection from unity is exponentially small in ω. Solution of Schrodinger's equation for and

If $\delta << \omega$ and $\epsilon << \omega$, Schrodinger's equation can be solved perturbatively. We are interested in a situation in which the neutron spin is initially fully polarized with respect to the field direction. We want to calculate the projection of the spin on the field direction at some later time. We write the wave function as

$$\chi=\begin{pmatrix} p \\ q \end{pmatrix}, \tag{42}$$

with $|p|^2+|q|^2=1$. Then $\chi^\dagger\sigma_z\chi=1-2|q|^2$ and Schrodinger's equation is

$$\frac{dp}{dt} = +\frac{i\omega}{2}p+\left[\frac{1}{2}\delta-\frac{i}{2}\epsilon\right]q \tag{43}$$

$$\frac{dq}{dt} = -\frac{i\omega}{2}q+\left[\frac{1}{2}\delta+\frac{i}{2}\epsilon\right]p. \tag{44}$$

The initial condition is $p(t_0)=1$ and $q(t_0)=0$. We obtain the first approximation, P_0 and q_0, by neglecting the δ and ϵ terms. The solution is

$$p_0(t) = p(t_0)e^{+\frac{i}{2}[\xi(t)-\xi(t_0)]}, \tag{45}$$

$$q_0(t) = q(t_0)e^{-\frac{i}{2}[\xi(t)-\xi(t_0)]}, \tag{46}$$

where

$$\xi(t)=\int_0^t \omega\, ds. \tag{47}$$

The first approximation for q is $q_0=0$. To obtain the next approximation q_1 we insert the first approximation q_0 into the Schrodinger equation for q as an inhomogeneous term. The solution is

$$q_1 = \int_{t_0}^t \frac{\eta}{2}p_0(s)q_0(t-s)ds \tag{48}$$

$$= \int_{t_0}^t \frac{\eta}{2}e^{i\xi(s)}ds\, e^{-\frac{i}{2}[\xi(t)+\xi(t_0)]} \tag{49}$$

$$= \tilde{q}e^{-\frac{i}{2}[\xi(t)+\xi(t_0)]}, \tag{50}$$

where $\eta = i\delta - \epsilon$. The phase of the expression does not influence the magnitude of q_1 and the approximate value of the projection of the spin on the z''' axis is

$$\chi^\dagger \sigma_z \chi \approx 1 - 2\left|\int_{t_0}^{t} \frac{\eta}{2} e^{i\xi(s)} ds\right|^2 . \tag{51}$$

Finally, we evaluate the depolarization

$$D = \frac{1}{2}\left|\int_{-\infty}^{+\infty} \eta e^{i\xi(s)} ds\right|^2 \tag{52}$$

for a specific case. Let the field be

$$\vec{B} = B_0 \hat{x} + \frac{dB}{dz} vt\hat{z}. \tag{53}$$

This configuration of fields is relevant to two situations that we encounter in the design of the experiment. First polarized neutrons must make the transition through the zero in the vertical component of the spectrometer magnet. We plan to apply a horizontal field in order that the spin can adiabatically pass through the zero. Second, we will flip the neutron spin using an adiabatic radio-frequency spin flipper. In such a device, the vertical field has a small gradient. The radio frequency is applied horizontally at a frequency that matches the Larmor frequency at some point along the neutron trajectory. In the Larmor frame, the neutron spin adiabatically follows the combination of radio frequency and vertical field. Evaluating the quantities above yields

$$\epsilon(s) = \frac{\mu B_0}{2\hbar}\left[\frac{s}{\tau}\sqrt{1+\frac{s^2}{\tau^2}} + \sinh^{-1}(s/\tau)\right], \tag{54}$$

$$\eta(s) = \frac{\tau}{\tau^2 + s^2}, \tag{55}$$

where

$$2\tau = \frac{2B_0}{\frac{dB}{dz} v} \tag{56}$$

is the time to pass through the transition region. The depolarization has the asymptotic form

$$D = \frac{\pi}{6} e^{\frac{4}{3} - \frac{\pi\lambda}{2}}, \tag{57}$$

where the adiabaticity parameter

$$\lambda = \frac{\mu B_0^2}{2\hbar \frac{dB}{dz} v}, \tag{58}$$

$$= \frac{\omega_1 B_0^2}{2\hbar \frac{dB}{dz} v}, \tag{59}$$

where $\omega_1 = 1.8 \times 10^4$ rad/s/G is the angular precession rate of the neutron. The asymptotic expansion was obtained using the method of steepest descent and is compared with a numerical calculation of the depolarization in Figure 36.

The gradient in the vertical field for our magnet design is $\sim 2 \times 10^3$ G/cm. A 10 meV neutron has a velocity of $\sim 1.4 \times 10^5$ cm/s. Solving for $\lambda = 6$, corresponding to $D = 1.6 \times 10^{-4}$, gives $B_0 = 0.43$ kG for a horizontal guide field in the neighborhood of the vertical field zero. A practical radio frequency field strength is a few Gauss. For $B = 5$ G, we obtain a field gradient of $\frac{dB}{dZ} = 0.27$ G/cm. Neither of these numbers presents difficulty.

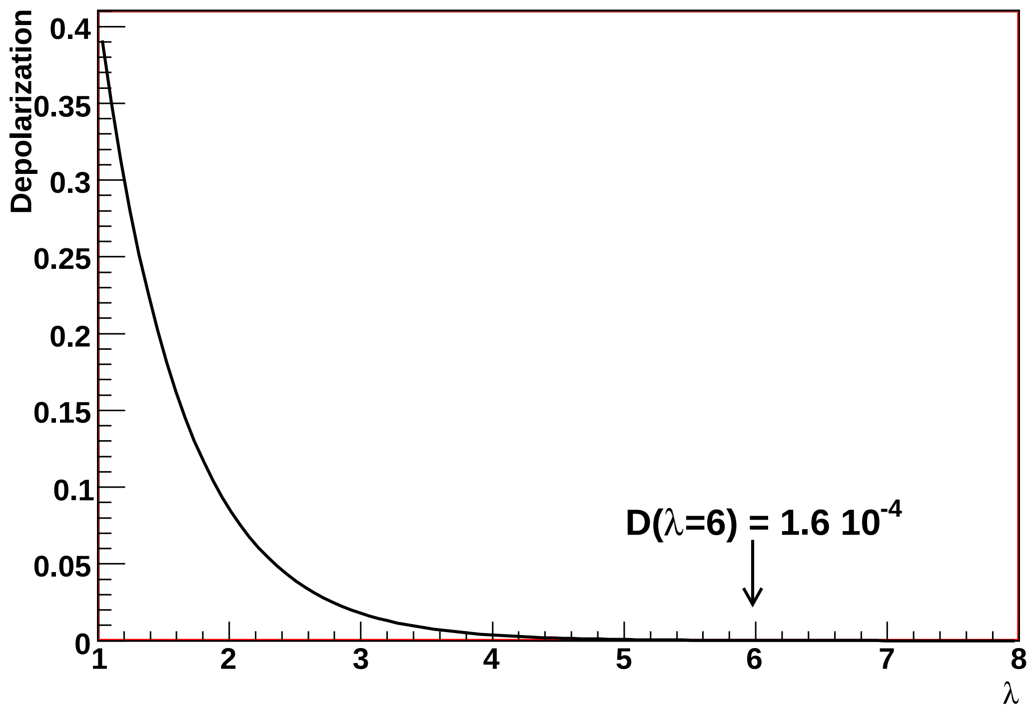

Figure 36: The asymptotic form of neutron depolarization's dependence on adiabaticity parameter λ. The depolarization is less than 2×10^{-4} for λ greater than 6.

4.2.2 Neutron Depolarization in Windows

The glass in the ^{3}He cell contains nuclei that have non-zero spin. Interaction with these spins can flip the neutron spin and lead to depolarization of the neutron beam. We estimate the depolarization and show that it is negligible small.

The chemical composition glass type GE180 by weight percent and the incoherent scattering cross sections are given below in Table 4.

Component	Fraction (% wt/wt)	σ_{inc} (mb)	P (ppm)
SiO_2	60.3	9	45
BaO	18.2	210	124
Al_2O_3	14.3	9.8	14
CaO	6.5	25	14
TiO_2	0.21	2750	36
Fe_2O_3	0.030	380	0.7
SrO	0.025	60	0.08
ZrO_2	0.025	150	0.15
MgO	0.020	46	0.1
Na_2O	0.020	1550	5
K_2O	0.012	370	0.5
Li_2O	0.001	250	.008
PbO	< 0.004	3	0.0002

Table 4: Fraction by weight, incoherent neutron scattering cross section, and spin-flip probability for a 3 mm thickness for the components of GE180 glass.

The density of the glass is 2.5 gm/cm^3. The spin-flip cross section is 2/3 of the incoherent cross section. We assume that the exit window is 3 mm thick. The spin-flip probabilities for the metallic components in ppm for a 3 mm exit window are given in the table. There are 2.1×10^{-3} moles/cm^3 of oxygen. The upper limit for the incoherent cross section is 8 mb giving a spin flip probability of less than 64 ppm for a 3 mm window. The estimated total spin-flip probability is 305 ppm. However, the neutrons are scattered into 4π and the solid angle of the decay volume is $\sim 10^{-3}$ of 4π. The depolarization is $\sim 3 \times 10^{-7}$ and is negligible.

The Fe_2O_3 component of the glass can depolarize the neutron beam by spin-flip scattering by the unpaired electrons. The total cross section for spin flip scattering is $\sim 4\pi(\gamma e^2/mc^2)^2 = 3.6$ b. The spin flip scattering probability is then $\sim 6 \times 10^{-6}$. The fraction of neutrons scattered into the decay volume is $\sim 6 \times 10^{-9}$ and the beam depolarization by electron scattering is negligible.

4.2.3 Neutron Pulse Width

The relationship between neutron time-of-flight (TOF) and energy is modified by a non-zero pulse width of the neutrons produced in the spallation target. The neutron polarization determination must be corrected for this effect, and a systematic uncertainty is introduced through imperfect knowledge of this correction. Obviously, the width of the incident proton, 1 μs for the SNS, contributes to this effect. A larger contribution, however, arises from the moderation time of the neutrons. A simplified model that treats each neutron energy as a Maxwell-Boltzmann TOF distribution [76], estimates a pulse width of approximately 250 μs with a 600 μs $1/E$ tail. This estimate leads to a first-order correction to the neutron polarization determination of 2×10^{-3}. The actual TOF profile of the FNPB will be measured by using a neutron monochromator. Measurement of this distribution to 5% accuracy will result in an uncertainty on the neutron polarization of approximately 1×10^{-4}.

4.2.4 Beta-Delayed Neutrons

The beam polarization determination relies on accurate neutron energy measurement through TOF which in turn is based on the fact that the neutrons, prompt neutrons, in the spallation source are produced almost at the same moment by a 1 μs long proton pulse. In the moderation process which takes about 250 μs, the neutrons will end up with different energies and after propagating through a 18 m long flight path, the neutrons with different energies arrive to the experiment in significantly different times, thus allowing an accurate neutron energy determination through TOF measurement. This TOF neutron energy dependence is diluted for other than the prompt neutrons, such as β-delayed neutrons and neutrons from photo production.

Spallation reactions are known to be accompanied by sub-threshold fission and, therefore, delayed neutrons with half-lifes up to minutes are observed to be produced by β-decaying fission products between prompt pulses. These neutrons can constitute a source of background in some experiments, as shown at the IPNS source studies in Argonne [77]. Small angle neutron scattering and precision neutron polarimetry with a broad energy spectrum are examples of experiments at SNS where such a background can potentially limit the accuracy of the experiment.

The delayed neutron fraction f_{d} depends strongly on the target material of the spallation source. We obtained an estimate of 10^{-5} for the delayed neutron fraction for the SNS Hg-target from the Z^2/A systematics of the fission cross section [78], assuming that the neutron- and proton-induced fission of mercury up to 1 GeV energy are the dominating production processes for β-delayed neutrons, and using the IPNS measured value of 4.4×10^{-3} for ^{238}U. Our estimate is well in agreement with a preliminary result from the MCNPX/CINDER'90 calculations [79].

There is a proposal to measure the delayed neutron fraction of the SNS neutron source. A measurement of f_{d} at the FnPB, which is viewing onto the SNS cold hydrogen moderator, relies on the fact that the delayed neutrons that are produced continuously in the source, are moderated in the same way as the prompt neutrons. By measuring the ratio of the delayed neutron yield to the total neutron yield in a neutron pulse, the delayed neutron fraction f_{d} is obtained. There are a few options for a practical implementation of such a measurement depending on the choice of the neutron detector and the use of neutron absorbers in the beam.

Recently, two such measurements were performed at LANSCE to determine the β-delayed neutron fraction at the LANSCE pulsed spallation neutron source, which uses a tungsten target which is expected to have a factor 5–10 larger f_{d} than in the Hg target. In the first measurement a known thickness of ^{3}He was installed in the FP12 beam to fully absorb the low energy part of the prompt neutron spectrum and then the partially attenuated delayed neutrons in this energy range were measured in transmission. The value for the delayed neutron fraction could not be determined by this measurement because of backgrounds but an upper limit of less than 10^{-4} was obtained. The second measurement used the SPEAR reflectometer on 1FP09 to remove the backgrounds and reflect and count partially attenuated delayed neutrons in the energy range where the prompt neutrons were absorbed by the ^{3}He. The preliminary result of this measurement gives $f_{\mathrm{d}} = 1 \times 10^{-4}$ [80]. At SNS we expect this value to be $f_{\mathrm{d}} = 1 - 2 \times 10^{-5}$.

A measured β-delayed neutron fraction of a few times 10^{-5} at the FnPB introduces the uncertainty less than 10^{-5} to the correlations.

4.2.5 Magnetic Field Inhomogeneities

The magnetic field that defines the spin direction and the charged particle trajectories decreases in the z direction.

If the particle starts below the mid plane of the decay volume then it encounters an increasing field magnitude. As a result the particle may be reflected in the field pinch.

The resulting changes in the yields of particles into the up and down detectors may lead to systematic errors. In this section we evaluate these changes and estimate the corresponding systematic uncertainties. The systematic uncertainties in the correlations are shown to be $\sim 10^{-3}$.

The Fierz interference coefficient depends on the shape of the electron spectrum and is not changed if the charged particles are reflected. The electron-spin A, the neutrino-spin B, and the electron-neutrino a coefficients are changed. We work out the change in A and give the results for B and a. The charged particles spiral around magnetic field lines and the magnetic flux contained within the orbit is an adiabatic invariant. The field is strong and nearly constant in the decay volume and the adiabaticity condition

$$\omega >> \frac{1}{|\vec{B}|}\left|\frac{d\vec{B}}{dt}\right|, \tag{60}$$

is well satisfied. Let p_0 be the magnitude of the momentum of the electron (proton) and p and q be the components along and perpendicular to the field direction. The electric field is negligible in the vicinity of the decay volume and the magnitude of the momentum vector is conserved

$$p_0^2 = p^2 + q^2. \tag{61}$$

The adiabaticity condition is

$$q^2 = p_0^2 \sin^2\left(\theta\frac{B}{B_i}\right), \tag{62}$$

where ξ is the initial angle between the field direction and the momentum direction and B_i and B are the initial and subsequent field strengths. The adiabaticity condition gives p^2 as a function of the field strength

$$p^2 = p_0^2\left[1 - \sin^2\left(\xi\frac{B}{B_i}\right)\right]. \tag{63}$$

The particle is reflected if $p^2 = 0$, which occurs if $B_i/B_0 \leq \sin^2\theta$, where B_0 is the maximum field strength. Express the field strength about the maximum (at $z = 0$) as

$$B(z) = B_0\left[1 - \alpha\left(\frac{z}{z_0}\right)\right], \tag{64}$$

where the beam extends from $-z_0$ to $+z_0$ and the homogeneity of the field is $\alpha = 10^{-2}$. If a particle starts at $z > 0$ and is going toward negative z ($\theta > \pi/2$), it will be reflected if $\theta - \pi/2 < \sqrt{\alpha}z/z_0$. All particles for which $\theta - \pi/2 < \sqrt{\alpha}z/z_0$ reach the up detector and those for which $\theta - \pi/2 > \sqrt{\alpha}z/z_0$ reach the down detector.

The electron-spin asymmetry is defined by

$$\frac{dY}{d\cos\theta} = \frac{1 + P_n A \cos\theta}{2}, \tag{65}$$

where Y is the yield and P_n is the neutron polarization. For neutrons that decay at z with $P_n < 0$, the yield in the up detector is

$$\begin{aligned}
Y_{\mathrm{up}} &= \int_0^{\frac{\pi}{2}+\sqrt{\alpha}\frac{z}{z_0}} \left(\frac{1 + |P_n|A}{2}\right) \sin\theta \, d\theta & (66)\\
&= \frac{1}{2}\left\{1 - \sin\left(\sqrt{\alpha}\frac{z}{z_0}\right) + \frac{|P_n|A}{2}\left[1 - \sin^2\left(\sqrt{\alpha}\frac{z}{z_0}\right)\right]\right\} & (67)\\
&\approx \frac{1}{2}\left[1 - \sqrt{\alpha}\frac{z}{z_0} + \frac{|P_n|A}{2}\left(1 - \alpha\frac{z^2}{z_0^2}\right)\right]. & (68)
\end{aligned}$$

The yield has a first-order dependence on the position of the decay. However if we reverse the polarization and add the yield in the up detector with polarization up and the down detector with polarization down, the first order dependence cancels

$$Y_{u+} + Y_{d-} = 1 + \frac{|P_n|A}{2}\left(1 + \alpha\frac{z^2}{z_0^2}.\right) \tag{69}$$

The position is not observed, and the above expression must be averaged over z to obtain the experimental yield

$$\Delta Y = 1 + \frac{|P_n|A}{2}\left(1 + \frac{\alpha}{3}\right) \tag{70}$$

for a uniform beam. For $\alpha = 10^{-2}$, the correction is 3 parts in 10^3 and is known to 10%.

The correlations B and a can be treated in the same way. For B, forming the polarization sum removes the first order dependence and gives a known correction close to 1 for B. The electron-neutrino correlation a does not involve polarization. The coefficient a will be determined by measuring the fraction of the decays for which the electron and proton go into the same detector. The sum,

$$Y_{uu} + Y_{dd} = u(r) + a\left(1 + \frac{\alpha}{3}\right) v(r), \tag{71}$$

where $u(r)$ and $v(r)$ are known functions of the ratio of the neutrino and electron momenta r. Again, the correction to a is close to 1. We have demonstrated that, by forming appropriate sums of yields, we can make the corrections to asymmetries arising from inhomogeneities in the magnetic field negligible.

4.2.6 Electric Field Inhomogeneities

The geometry of the decay spectrometer will produce a maximum in the electrostatic potential at the center of the HV electrode (see Section 3.3). This effect will introduce a systematic effect in the determination of the correlation parameter a because a decay proton created above or below the center, with longitudinal velocity in the direction of the center, would be reversed if its kinetic energy is not enough to overcome the potential barrier.

In order to measure a to a precision of $\Delta a \leq 10^{-4}$, it is necessary to ensure that the fraction of decay protons that are reversed is less than 10^{-4}, which in terms of the velocity distribution implies that the inhomogeneity of the electric field in the center of the decay volume should be small enough to warranty that protons with longitudinal velocity $v_z \geq 20$ m/s will not be reversed. To fulfill this requirement, the electric field needs to have an inhomogeneity of less than a few μV/cm. We believe that this inhomogeneity level is attainable in the decay volume since the distance to the metallic surfaces of the electrode is large enough to avoid local field variations related to the metallic grain size. Additionally, grain size effect can be reduced by coating the electrodes with colloidal gold or other similar materials. Homogeneous electric fields of less than 1 μV have been already attained with this technology.

4.2.7 Misalignment

One of the possible systematic effect which will affect our measurements of asymmetries are the geometric misalignments inside our spectrometer. The spectrometer has been designed to be perfectly symmetrical, both geometrically and field-wise. However any departures from the ideal symmetry will cause false asymmetries in our results. There are a number of possible ways in which misalignments can contribute to a systematic uncertainty:

- Offsets between neutron beam axis and magnetic field's axis of symmetry. Such an offset will not only cause different distances to the two detectors, but will also force electrons to experience an increasing magnetic field in one direction, possibly causing reflections in the opposite direction. To first order this effect can be neglected (due to the flipping of the neutron spin), however at higher precision there may still be a residual false asymmetry.
- Asymmetries in beam profile. This effect reduces to the previous one.
- Offsets between neutron beam axis and electric field's axis of symmetry. Among other effects, this may cause a difference in time-of-flight for protons that travel to the different ends of the spectrometer. As time-of-flight will be used for an approximate proton momentum reconstruction, this may result in a false asymmetry in proton's momentum. Just as in previous points, we believe that spin change of the neutron should cause this effect to mostly cancel, however if any parts of this process are of additive nature then it is possible that a residual false asymmetry may still remain.
- Offsets between neutron beam axis and the geometrical axis of symmetry of the spectrometer. This may cause different acceptances for the two detectors. Such an effect, however, can be verified and corrected for empirically, by observing the event rate at two detectors in single detection mode.

Preliminary estimates show that the effects of the above points on the asymmetry are of very small scale. However, a detailed Monte Carlo simulation, which will include measured maps of magnetic and electric fields, as well as a simulation of neutron beam profile, is needed in order to quantify the impact of misalignments more precisely. We are currently working on such simulations.

4.2.8 Electron Backscattering from Detectors

A source of systematic error in the measurement of a and A, and to a lesser extent B is the backscattering of electrons from the silicon detectors. For these three observables, we need to know which detector an electron hits first. It is possible that an electron will hit one detector first, depositing a small energy, and then deposit most of its energy in the opposite detector. If the relative timing of the two events can not be determined, the event is ambiguous. We have written a Monte Carlo code to track electrons through the silicon detector. The program simulates events that deposit arbitrary amounts of energy. From these results, we can estimate the effect of electron backscattering.

The basis for the approximation is that for small energy depositions the electrons don't go very deep into the silicon and multiple scattering is small. The electrons are back scattered by large angle Rutherford (elastic) scattering from the (screened) electric field of the nucleus. We make the approximation that the energy loss is continuous. This approximation is appropriate because charged particles lose energy due to their interaction with the atomic electrons. The total cross section for inelastic collisions is ~ 10 times larger than for elastic collisions.

The timing uncertainty for a an electron that deposits a small amount of energy in a silicon detector is proportional to $1/\Delta E$ (see Section 4.2.15). We estimate that the timing uncertainty for $\Delta E = 100$ keV to be 1 ns. The time difference for up-down versus down-up ordering is proportional to $1/V$ or $\sim 1/\sqrt{\Delta E}$. Thus for events below some threshold in ΔE we can not determine which detector was struck first from timing. We estimate this threshold to be 2. keV for 4 m separation between the detectors.

To get a feeling for the roles of inelastic and elastic scattering, consider the standard multiple scattering and ionization energy loss. Table 5 shows the probability of backscattering from silicon, with $\Delta E < 10$ keV, as a function of incident electron energy. Note that the scattering angle $\sigma = [(15 \text{ MeV})/PV]\sqrt{\Delta x/x_0}$ with $x_0 = 21.82 \text{ gm/cm}^2$. The probability of backscattering with small energy loss is small, less than 0.03. In addition, approximately 2/3 of the backscattered electrons will be reflected back to the initially struck detector by the magnetic field pinch. The fraction of events that need to be corrected will therefore be of order 0.01. The Rutherford cross section decreases as $1/Q^4$ for large scattering angles. Therefore the escape probability is dominated by scattering angles near $\pi/2$. For these events, the electron penetrates much less than Δx before it makes a hard scattering and the initial multiple scattering of the electron can be neglected. $\sigma/\sqrt{3}\Delta x$ estimates the transverse diffusion after the hard scattering. For energies less than 200 keV, the approximation that $s/\sqrt{3} << 1$ is poor and the estimate is qualitative. Since the estimated backscattering probability increases as the electron energy decreases, the probability $P(E)$ is approximately constant. We will

E_e (MeV)	dE/dx (MeV/gm/cm^2)	$\Delta x(\Delta E = 0.01 \text{ MeV})$ (gm/cm^2)	$\sigma/\sqrt{3}$ (deg.)	$P(\Delta E < 0.01 \text{ MeV})$
0.050	4.867	0.0021	0.84	0.027
0.100	3.074	0.0032	0.55	.011
0.200	2.112	0.0047	0.36	0.0040
0.500	1.557	0.0064	0.19	0.00088
1.000	1.443	0.0069	0.11	0.00026

Table 5: Probability $P(\Delta E < 0.01 \text{ MeV})$ of electron backscattering from silicon with an energy loss of less than 10 keV, as a function of incident energy.

have to make small corrections to the measured A and a for backscattering. These corrections will be most important for small electron energies. A strategy for carrying out these corrections is to measure A and a as a function of the electron threshold (10 and 20 keV for example), perform the corrections and demonstrate that the corrected A and a don't depend on the threshold.

4.2.9 Proton Back Scattering from Detectors

The loss of events due to proton back scattering does not affect the asymmetry because the probability is small and all protons have nearly the same probability of back scattering. The probability of proton backscattering is much smaller than for electrons because the protons have less energy and their mass is larger than for electrons. Protons may be backscattered as they enter the detector. All protons reach the detector with approximately the same energy, the sum of their initial kinetic energy (0 to 0.8 keV) and the accelerating potential (30 keV). The stopping power (range) of a 30 keV proton in Si is 500 MeV/gm/cm^2 (1.0×10^{-5} gm/cm^2) [81]. The protons lose 5.0 keV in the 1.0×10^{-5} gm/cm^2 inert layer. The probability, P, of a proton scattering by an angle of more than $\pi/2$ before losing 5 keV can be estimated using the screened Rutherford scattering cross section [82]. Nico *et al.* [35] discuss proton back scattering in their report on the measurement of the neutron lifetime by integrating the Rutherford formula and comparing to data for a gold surface barrier detector, as used in the NIST neutron lifetime experiment. They find

$$P = N_a \sigma \tag{72}$$

where

$$\sigma = \frac{\pi}{4} Z^2 r_e^2 \left(\frac{mc^2}{E} \right)^2 \tag{73}$$

with r_e being the classical electron radius, Z the charge of the target material and N_A the number of target atoms per cm^2. For 30 keV protons we get $\sigma = 3.5 \times 10^{-21}$ cm^2 and $N_A = 2.1 \times 10^{17}$ atoms/cm^2. The estimated probability of backscattering in the inert layer then becomes $P = 7.3 \times 10^{-4}$. We therefore expect proton back scattering to be very small. We plan to measure the probability of proton back scattering during detector tests and characterization.

4.2.10 Proton Time-of-Flight

The trigger for the experiment will be a coincidence between an electron and a proton each above ~ 5 keV. The electrons have much shorter flight times than the protons, and the distribution of time differences T between electron and proton arrival times will be dominated by the proton time-of-flight. We demonstrate that a time-of-flight gate having a width of $T_{\text{cut}} = 50$ μs will capture $\sim 99.9\%$ of decay events. The protons are non-relativistic with a TOF for the most energetic ones of 5 μs. At the low energy end of the spectrum the proton momentum distribution $Q(p)$ goes as $Q(p)dp \propto p^2$. Furthermore, at these momenta, $p \propto 1/T$, where T is the TOF. $U(T)dT$, is related to $Q(p)$ by

$$\begin{aligned} U(T)dT &= Q(p)\frac{dp}{dT}dT && (74) \\ &= \frac{1}{T^2}\frac{1}{T^2}dT && (75) \end{aligned}$$

so that the probability of losing an event is given by

$$P_{\text{loss}} = \frac{\int_{T_{\text{cut}}}^{\infty} 1/T^4 dT}{\int_{5\mu s}^{\infty} 1/T^4 dT} \quad (76)$$

$$= \left(\frac{5\mu s}{T_{\text{cut}}}\right)^3 . \quad (77)$$

therefore the loss is $P_{\text{loss}} = 0.1\%$ for $T_{\text{cut}} = 50\ \mu$s.

Furthermore, we can study the behavior of the dependence of the different correlations on T_{cut} by analyzing the each correlations for different values of T_{cut} and extrapolating to $T_{\text{cut}} = \infty$.

4.2.11 Detector Rate Effects

Systematic effects due to count rates in the detectors include false coincidences and pulse pileup. The time-averaged integral count decay rate is estimated in Section 4.1 to be of order 100 Hz. This rate is spread over approximately 20 pixels for each of the two detectors. The peak rate is approximately twice the time-averaged rate, giving a peak per-pixel signal rate of 10 Hz, including the fact that each neutron decay produces two charged particles. The background rate is harder to estimate. For this, we take the experience of the NIST cold-beam neutron lifetime experiment [35], where the background rate was approximately equal to the signal rate. Since the silicon detector in the NIST experiment was much closer to potential sources of background, such as collimation, than for this experiment, a background rate of 10 Hz per pixel is conservative.

Coincidences can occur when a proton is observed in one pixel and an electron is observed in that pixel, the six surrounding pixels, or the corresponding seven pixels of the opposing detector. In calculating the false coincidence rate, the singles rates in these 14 pixels must be considered. Taking the total peak per pixel rate to be 20 Hz and assuming a coincidence window of 50 μs gives a false coincidence rate of 14 mHz. The corrrection then applied to the observed decay rate is then $14 \times 10^{-3}/20 = 7 \times 10^{-4}$. Since the correction to the observed asymmetry depends upon the difference in rates between the two detectors, it is further reduced by the value of $A \sim -0.1$ to 7×10^{-5}.

Pileup occurs when two uncorrelated hits occur in the same pixel within a time too short to resolve them as separate events. Since the signals are transient digitized, this minimum time to resolve the energies deposited by the two pulses depends upon the sophistication of the analysis software, as well as intrinsic hardware limitations. As a reasonable estimate, we take this resolving time to be 2 μs. This gives a pileup probability of 4×10^{-5}, which can be neglected.

4.2.12 Neutron Polarization Uncertainty

The polarization of the neutrons at the moment of the decay needs to be known with high precision (better than 0.1%) in order to avoid systematic effects in the determination of the correlation parameters A and B. In the experiment, neutrons will be polarized by the passage through a ^{3}He spin filter (Section 3.7). This technique to polarize neutrons has already been tested and used in numerous experiments like NPDGamma [49]. Neutron polarization is determined by the measurement of the relative transmission through the polarized and unpolarized ^{3}He spin filter cell (Section 3.7). There are several factors that limit the precision to which the neutron polarization can be determined with these methods. At LANSCE, we have initiated a program to establish techniques and find the upper limit for the neutron polarization accuracy. Up-to-date, a first measurement consisting of a polarizer and two neutron monitors for determination of the relative transmission rate, as well as a RF resonant spin-flipper followed by an analyzer cell and a third monitor (see Figure 37) has been completed. In the measurement the neutron beam was collimated to 2.5 cm diameter. The main goal of this experiment was to reduce detector backgrounds compared to backgrounds observed by the NPDGamma, by increasing the distances between the detectors and the other elements in the apparatus so that the flux of scattered neutrons is reduced. The use of the RF resonant spin-flipper and the analyzer cell, in combination with the third monitor, provides an independent measurement of the neutron polarization [67]. The level of agreement of the polarization value obtained with this method and that obtained from the relative transmission between the first two monitors is an indication of the accuracy of the transmission method that is planned to be used in the abBA experiment.

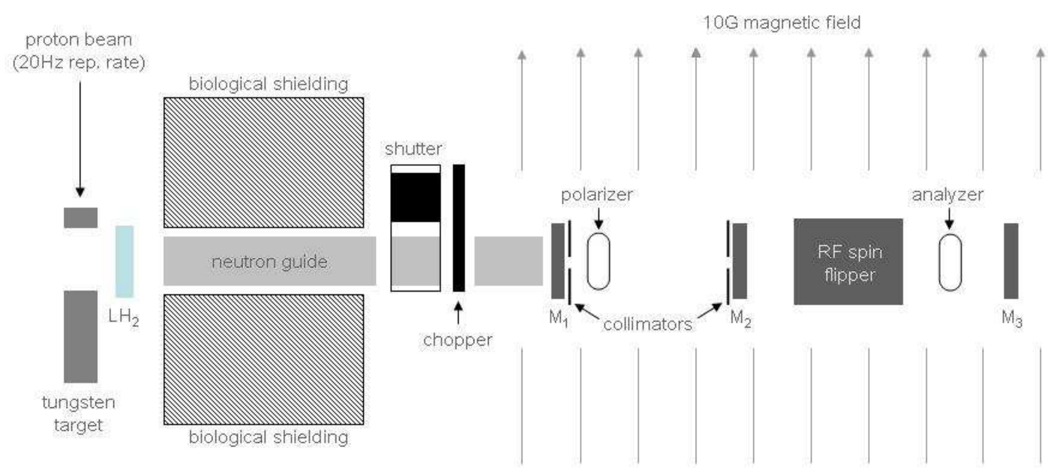

Figure 37: Setup of the first precision polarimetry experiment performed in 1FP12 at LANL in 2007.

The analysis of the data from the first precision polarimetry run is in progress, however, preliminary results indicate that neutron polarization was determined to a statistical precision of 0.7%. In the abBA experiment, statistics will not be a limitant for the neutron polarization determination. If we scale the 0.7% statistical error in relative transmission measurement at LANSCE with 2.5 cm collimator to what we would have in the experiment at the FnPB (10 cm collimation and factor 10 times higher beam flux), we will have statistical errors of 0.06% in the abBA.

The precision of polarization is determined by systematic effects listed below (some or them are also discussed in [68]).

1. Use of the relative transmission measurement in the determination of the beam polarization is based on the accurate knowledge of the n-^{3}He absorption cross section as a function of the neutron energy, which is known to follow $1/v$ law with 10^{-4} level.

2. Beam related systematic effects:

- Neutron pulse width (see discussion in Section 4.2.3).
- Neutrons have different flight path lengths in the beam guide.

3. Beta-delayed neutrons (see Section 4.2.4).
4. Precision in the determination of the flight path length, which can be very accurately measured using the Bragg edge transmission method in Berylium [83].
5. Backgrounds in beam monitors and drifts that can distort the monitor signals and the M1/M2 ratio, producing an error in the determination of τ.
6. Depolarization during the neutron spin transport from polarizer to the decay volume (discussed in Section 4.2.1).
7. Stern-Gerlach steering, depending on the sign of $\vec{\mu_{\rm n}} \cdot \vec{B_0}$, deflects the beam along or opposite to the spectrometer field direction in less than 10^{-4} cm. Stern-Gerlach steering has no effect on the beam polarization determination with the TOF dependence of relative transmission method or spin flipper and analyzer method, however for beam polarization determination using the TOF dependance of the measured B correlation asymmetry, the Stern-Gerlach steering may introduce a small uncertainty.
8. Neutron velocity change by the field gradient has an effect only on the beam polarization determination using TOF dependence of the measured B correlation asymmetry (discussed in Section 4.2.18).
9. Spin flipper efficiency, which is 99.98% for the adiabaticity parameter λ=6 (see Section 4.2.13).
10. Imperfect ^{3}He spin filter cell;
    - The two beam windows of the cell are not perfectly parallel causing different ^{3}He path length for neutrons.
    - Varying ^{3}He polarization as a function of time. If the 8-step spin sequence is used and spin is reversed at 60 Hz and the polarization changes at the rate of 1% per hour, then a change in beam polarization over an 8-step spin sequence is at the level of 10^{-5}.

The total estimated uncertainty in beam polarization due to the aforementioned systematic effects is 4×10^{-4}, and the combined statistical and systematic uncertainty is 5×10^{-4}, which is below the 10^{-3} (0.1%) level that is needed for the abBA experiment. The next precision polarimetry experiment at LANSCE, where the goal precision of 0.1% is expected to be achieved, will take place in the summer of 2008. The experiment will study the systematic uncertainties and also MC simulations will be performed that can be reliably verified.

4.2.13 Spin Flipper Efficiency

The spin flipper has two states on and off. During the on-state the RF field is on and the beam polarization direction is adiabatically reversed with efficiency close to unity. In the off-state the RF field is off, the neutron polarization direction is not changed and no significant depolarization takes place in the spin flipper if the adiabaticity parameter λ has been properly selected.

During the spin reversal when the spin flipper is on, the spin flip efficiency is limited by depolarization; the polarization is not following the rotation of the effective magnetic field. In section 4.2.1 for the design flipper depolarization is estimated to be 1.6×10^{-4} for $\lambda = 6$ and at neutron energy of 10 meV. This depolarization gives the spin flip efficiency $1 - 1.6 \times 10^{-4} = 0.99984\%$ i.e. the uncertainty in the polarization is less than 1.6×10^{-4}. We need to be able to measure the spin flip efficiency with this accuracy.

4.2.14 Detector Efficiency

Silicon detectors have inherently high eficiency for detecting charged particles that reach the active area of the detector. We are concerned in particular about the effective efficiency for detecting both proton and electron from a neutron decay event in coincidence. Effects that can reduce the efficiency from unity are:

- Backscattering of either charged particle from the detector with sub-threshold energy deposition,
- Arrival time difference between the two particles that is outside the allowed coincidence window,
- Stopping of the proton by the detector grid, and
- Energy loss by the proton in the detector grid.

The first two effects are covered in Sections 4.2.8 and 4.2.9.

The front face of the detector is covered by an aluminum grid with lines 10 μm wide and 400 nm thick, with a spacing of 4 mm. The aluminum is thick enough to stop the 30 keV protons, resulting in a 5×10^{-3} loss in efficiency. A second effect occurs due to partial energy loss by the proton due to the detector grid. Since the aluminum grid is deposited by vacuum evaporation techniques using a semiconductor mask, the sides of the grid a not perfectly normal to the detector surface. The will add a low-energy tail to the proton distribution due to protons that pass through a partial thickness of aluminum. If we conservatively assume instead an angle of 45° to the detector surface and integrate this tail down to 1/2 the full energy peak, the result is 5×10^{-5}.

These efficiency effects are uniform across the detector, independent of neutron spin, and (because the protons have been accelerated to a nearly mono-energetic 30 keV), independent of the decay kinematics. The effects are then an overall reduction is detection efficiency that do not cause a correction to the observed asymmetries.

4.2.15 Detector Timing Resolution

Detector noise timing resolution. The timing resolution determines how low in energy we can go in reconstructing events in which the electron deposits energy in both detectors. In general, the noise in silicon detector systems includes contributions from several sources, including detector leakage current, Johnson noise in the feedback components, and noise from the first stage transistor. In our case, the detector and feedback components are cooled, reducing the first two contributions to negligible levels. The final term, due to noise in the FET used as a first stage amplifier, dominates.

At room temperature, the FET noise density, referred to the gate, is approximately 1 nV/$\sqrt{\text{Hz}}$. Cooling the FET to the detector operating temperature (approximately 120 K) reduces the noise density to approximately 0.5 nV/$\sqrt{\text{Hz}}$. This noise appears at the preamplifier output multiplied by the noise gain factor C_i/C_f, where C_i is the input capacitance from the detector pixel, FET gate, and electrical connection between the two, and C_f is the preamplifier feedback capacitance. Reasonable values are $C_i \sim 20$ pF and $C_f \sim 1$ pF, giving a noise gain of 20 and a noise density at the preamplifier output of 10 nV/$\sqrt{\text{Hz}}$. Assuming an effective integration time of 5 ns gives a total noise of approximately 140 μV at the preamplifier output.

The signal size at the preamplifier output is inversely proportional to C_f, 44 mV/MeV for $C_f = 1$ pF. Since the signal rise time t_r is approximately fixed regardless of the signal size V_0 (energy deposited E_0, the time resolution can be related to the voltage noise ΔV (energy noise ΔE) by

$$\begin{aligned} \Delta t &= \frac{\Delta V}{V_0} t_r, \\ &= \frac{\Delta E}{E_0} t_r. \end{aligned} \tag{78}$$

The detector rise time is ideally 20 ns, but we assume 30 ns for this estimate. This gives a time resolution of approximately 100 ns for a 1 keV signal.

Events in which an electron reflects from one detector, depositing some energy, and then stops in the opposing detector, depositing its remaining energy present a timing challenge to determine the initial electron direction. If the energy deposited in the detectors is E_1 and E_2 at times t_1 and t_2, two scenarios are possible. The electron could have struck detector 1 first at t_1, depositing E_1 and then traveling the distance between the two detectors with a velocity corresponding to E_2, or the converse. The difference in time between these two scenarios is given by

$$\Delta T = \frac{L}{c}\left(\frac{1}{\beta_1} + \frac{1}{\beta_2}\right), \tag{79}$$

where L is the distance between detectors and β_1 and β_2 are the relativistic velocities normalized to c. For this estimate, the electric field is ignored and the electron momentum is taken to be parallel to the magnetic field for both trajectories.

Figure 38 shows ΔT for a normalized detector separation of 1 m for various initial electron energies as a function of the energy deposited in one detector. From this plot, it is clear that the minimum ΔT occurs for the case where energy is shared equally between the two detectors, and for the maximum energy electron. When we fold in the detector timing resolution, however, the worst case is quite different, due to the variation in timing resolution with deposited energy. Figure 39 shows the ratio $\Delta T/\delta t$ of timing difference to timing resolution, normalized to 1 m detector separation, 1 ns rise time, and 1 keV energy noise. Since the timing resolutions of the two detectors must be added in quadrature, the case where little energy is deposited in one detector becomes the limiting one. In this limit, the initial electron energy does not matter. If we require $\Delta T/\delta t > 3$ to reconstruct the event, a minimum energy deposit of 2 keV is required, assuming a detector separation of 4 m, rise time of 30 ns, and energy noise of 3.2 keV. A detailed simulation of the interaction of electrons in the detectors is required to accurately estimate the size of this effect on the asymmetries.

In addition, the effect can be studied *in situ* by studying the variation in A with an artificially imposed threshold. In this method, electron backscatter events are treated as if the detector threshold is higher than the actual detector threshold, so that energy deposits of less than this "artificial threshold" are ignored. The variation in A with this artificial threshold is extrapolated to zero energy, to determine the correction for events lost due the actual non-zero detector threshold.

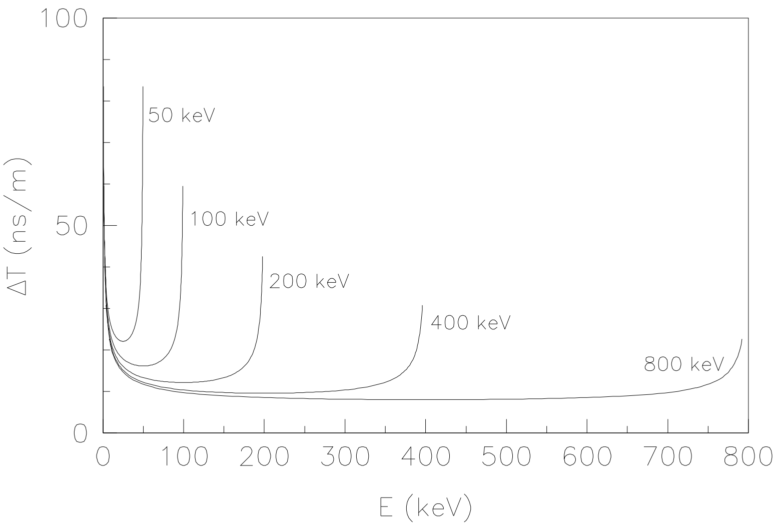

Figure 38: Timing difference between the two scenarios for an electron depositing energy in both detectors (detector-1 hit first, or detector-2 hit first) as a function of energy deposited in one detector. The curves represent different initial electron energies and are normalized to a 1 m detector separation.

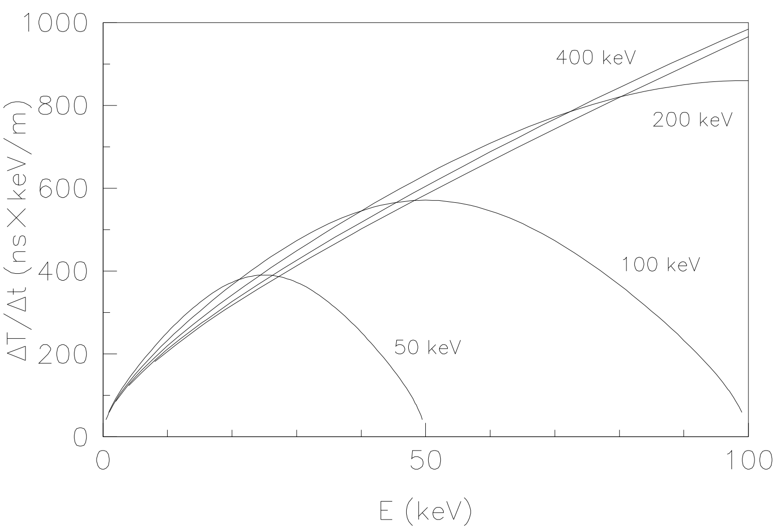

Figure 39: Ratio of timing difference to timing resolution as a function of energy deposited in one detector. The curves represent different initial electron energies and are normalized to a 1 m detector separation, 1 ns, and 1 keV energy noise.

4.2.16 Detector Energy Resolution

The detector energy resolution can be influenced by several factors. We have considered the following factors in estimating the detector energy resolution:

- detector leakage current,
- preamplifier noise,
- energy loss in the detector dead layer,
- detector Fano factor, and
- bremsstrahlung in the detector.

Detector leakage current is strongly temperature dependent and becomes negligible at the detector operating temperature. We have estimated the energy loss due to bremsstrahlung to be negligible. Energy loss in the dead layer is a few eV for electrons and can be ignored. For 30 keV protons, the energy loss in the dead layer is estimated to be approximately 10 keV. Statistical fluctuations in this loss can be expected to dominate the proton energy resolution with a contribution of as much as 5 keV.

Below approximately 20 keV, energy resolution for electrons is dominated by electronic noise in the preamplifier. As discussed in Section 4.2.15, the noise density at the preamplifier output is estimated to be 10 nV/$\sqrt{\text{Hz}}$. The effective integration time for measuring the energy of an event is approximately 1 μs, giving a total noise of 10 μV or 230 eV. Above 20 keV, electron energy resolution is dominated by the detector Fano factor [84], which characterizes fluctuations in electron-hole pair creation. This effect is proportional to $E^{1/2}$ and is approximately 1–2 keV at 800 keV.

Energy resolution affects the measurements in several ways. It sets a lower threshold for detection of events. This will be a few times the electronic noise level, giving a threshold of approximately 2 keV. Proton energy resolution can reduce the proton detection efficiency if the electron noise extends under the proton energy peak. With a noise threshold of 2 keV, a proton peak energy of 20 keV (after energy loss in the dead layer), and a resolution of 5 keV, this is not a concern. Finally, electron energy resolution can effect the accuracy of extracting the neutron decay parameters from the observed events, as they depend upon electron energy. This is directly true for b, as the electron spectrum shape directly determines this parameter. It is indirectly true for the other parameters, where a difference in threshold between the two detectors causes an error. Since both terms that dominate the electron energy resolution are statistical, averaging over the large number of events in each energy bin will allow determination of the average energy of the bin to high accuracy. The problem reduces to accurate energy calibration of the detectors, discussed in Section 4.3.

4.2.17 Residual Gas Scattering

The decay region and the detector set will be placed inside a 10^{-8} Torr vacuum. However, the long track lengths, resulting from a large magnetic field magnitude and low particle energies, combined with the high cross sections due to the low energies, make it important to understand the systematic effects of the residual gas on the electrons.

The track lengths of the particles depend strongly on the angle between their initial momentum vectors and the magnetic field direction. Using Geant4 simulations we have determined the mean track length of an electron to be 2.35 m (the spectrometer's total length is 4 m).

Knowing the residual gas density inside the spectrometer and the mean path of the electrons we can determine the scattering probability for a given electron. The target thickness is $a = l \cdot 10^{-11} \cdot 1.29\ \mathrm{mg/cm}^3 \cdot 6\ 10^{23}\mathrm{mol}^{-1}/A_{\mathrm{air}}$ where 10^{-11} term is the ratio of atmospheric and vacuum pressures, and $A_{\mathrm{air}} = 14.5\mathrm{g/mol}$ is air's average atomic weight. $l = 235$ cm is the mean track length. We get $a = 1.25 \times 10^{11}\ \mathrm{cm}^{-2}$.

For electrons in the energies of $\sim$ 40 keV the scattering cross section on atoms varies as $\sigma \approx A(\log E)/E$ (where A is the scattering form factor), and at 40 keV has the value of $3 \times 10^{-18}\ \mathrm{cm}^2$ [85]. Combining this with our previous result we find that the scattering probability for an average electron is $p \sim 3 \times 10^{-7}$. However, the energy loss of a given electron will be only a fraction of this number. From here we conclude that ionization on residual gas contributes negligibly to our systematic uncertainties.

In the case of the protons, the situation is more difficult. At an energy of 10 eV, the proton cross section is about $1 \times 10^{-14}\ \mathrm{cm}^2$, while at 100 eV, the cross section is $7 \times 10^{-15}\ \mathrm{cm}^2$. This would lead to a scattering probability of $p \sim 0.1\%$ and $p \sim 0.07\%$ under these conditions. However, since the process is very forward peaked (max of scattering angle is less than $.3^o$ for 100 eV and less than $.5^o$ for 10 eV), the momentum transfer for a 100 eV proton at this angle is about 1 keV, which leads to a shift in TOF of less than 25 ns. Going from this angle to 10 degrees, the cross section drops by almost two orders of magnitude, which would lead to a correction of .05 % . We are currently working on implementing a full Geant 4 simulation from Mendenhall and Weller [86], based on the model of Ziegler and Biersack[87].

4.2.18 Neutron Velocity and Stern-Gerlach Force

As the neutron enters the decay region, it experiences a force due to the Stern-Gerlach force ($\vec{\mu} \cdot \vec{B}$) interaction that changes sign when the neutron spin is flipped. The force has the form

$$\vec{F} = \mp\mu \left(\frac{\partial B}{\partial y}\hat{y} + \frac{\partial B}{\partial z}\hat{z} \right). \tag{80}$$

The first term changes the neutron velocity, while the second produces a vertical deflection.

The spin-dependent change in velocity causes a spin-dependent change in decay rate with

$$\begin{aligned} \frac{\Delta N}{N} &= -\frac{\Delta v}{v}, & (81) \\ &= \frac{\Delta E_n}{2E_n}, & (82) \\ &= \frac{\mu \Delta B}{2E_n}. & (83) \end{aligned}$$

For $\Delta B = 4$ T and $E_n = 4$ meV, $\Delta N/N = 3 \times 10^{-5}$.

The spin-dependent deflection is given by

$$\delta z = \mp \frac{\mu \Delta y^2}{4E_n}\frac{\partial B}{\partial z}. \tag{84}$$

To estimate the size of the deflection, we use $\partial B/\partial z = 800$ G/cm, $\Delta y = 50$ cm, and $E_n = 4$ meV. This gives a deflection of $\delta z = \mp 7.5\ \mu$m. If the beam extends 6 cm in z, a change in decay rate of $\Delta N/N = 2.5 \times 10^{-4}$ can be expected.

4.3 Energy Calibration

The measured beta asymmetry depends on the electron energy (see Equation 1). We have to understand our detector reponse to be able to extract the beta asymmetry from the measured data. The width of the detector response function is very small in our detector. Note that in many previous experiments (including PERKEO II), plastic scintillators were used, and there the detector response function has a width of typical 100 keV. Also, the low energy tail due to backscattered electrons which is usually a problem in low energy electron spectroscopy is strongly suppressed in our setup, as backscattered electrons are either reflected back to the detector being hit first due to a reflection from the strong magnetic field in the decay volume, or they hit the second detector. The sum of the measured energy in both detectors is close to the energy a single detector would count. The efficiency of the detector for detecting electrons is 99.9%. Therefore, we expect the uncertainty due to the shape of the detection function function to be negligible. We expect the detector to have a nearly linear energy channel relationship. To determine it, we plan to use a set of radioactive calibration sources, which are backed by very thin ($10\,\mu\mathrm{g/cm}^2$) carbon foils and can be moved in the decay volume in the horizontal plane to reach every point in the detector. Six possible candidates for such calibration sources are identified in [28]. An uncertainty of 1% in the slope of the energy channel relation would cause an uncertainty of $\Delta A/A \sim 0.2\%$.

4.4 Particle Trapping

The decay volume and the surrounding area of our spectrometer form a deep Penning trap for electrons. This trap doesn't cause a problem for electrons above our energy threshold. The longitudinalization of the electron momentum due to the magnetic field allows all of them to escape and to reach the detector. But it can cause a fluctuating background and, in the worst case, high voltage breakdowns and discharges which are a danger for the detector. The filling time constant due to electrons from neutron decay is long and can be neglected, if not due to the residual gas level. Experience from other experiments (i.e. the NIST lifetime measurement [88] shows that typically a vacuum of 10^{-8} mbar has to be reached. There are strategies to remove the particles in a penning trap: Wire grids around the decay volume would do it, but cause systematic uncertainties. An electric field perpendicular to the magnetic field would remove particles, but would spoil the measurement of proton flight times [89]. If the filling time constant is slow enough, it can be sufficient to empty the trap from time to time, by swiping a wire through the trap, as it is planned in the neutrino mass spectrometer KATRIN [90], or by ramping down the high voltage.

Another, and typically much more severe problem are penning traps between the generally cylinder-shaped electrodes. A magnetic field line which connects two HV electrodes acting as cathodes and on which the electric potential has a minimum with a depth in the order of 1 kV can easily cause penning discharges, as the electrodes give rise to the well-known multiplication mechanism of a Penning discharge, which starts with a positive residual gas ion, which is accelerated towards the electrode. The impact produces several secondary electrons, which could be trapped. This happens if they collide with a residual gas atom or due to non-adiabatic process which prevents them from being reabsorbed at one of the cathodes. Then in turn, the trapped secondary electrons ionize residual gas atoms. Such a penning discharges has to be avoided, the remedy is a proper design of the electrodes which avoids these traps.

A Recoil and Radiative Corrections

In order to obtain the parameter V_{ud} from precise neutron decay data, one has to take into account all corrections for neutron decay with the appropriate accuracy. It is well known that recoil effects [91, 92] (see, also [93, 94]) and radiative corrections [95, 96, 97] essentially modify Eq.(1) and coefficients a, A, and B. These corrections became important at the level of few percents and should be carefully examined to produce the relevant background for the data analysis and to be able to search for new physics, because these corrections have the same order of magnitude as the expected deviations from the Standard Model. The main concern here is the completeness of the possible corrections and reliability of calculations up to the level of the best available experimental accuracy. For example, radiative corrections have been carefully calculated for Fermi transitions, however, neutron decay contains contributions from Gamow-Teller transitions as well. Another problem is related to the traditional procedure of separation of radiative corrections into "outer" and "inner" parts. The first part is a universal function of electron energy and is independent of the details of strong interactions. The second part, dominated by the large QCD short-distance term, contains nucleon structure-dependent contributions. Since "outer" corrections could be calculated precisely, they do not bring uncertainties into extraction of parameters from experimental data. The problems arise with estimations of the "inner" corrections: this is because a part of them is very dependent on hadron structure model, and another (main) part results from QCD loop calculations with very high momentum transfer based on a consideration of the nucleon as a system of free quarks. Moreover, the renormalization procedure [98] mixes the leading "outer" and small "inner" parts of corrections and, as a consequence, leads to even more uncertain results (in terms of reliability and control).

Let us consider, nucleon structure "independent" and "dependent" corrections. The independent ones were defined by eq.(20) in the paper [95] as

$$\begin{aligned} g(E,E_m) &= 3\ln\left(\frac{m_p}{m_e}\right) - \frac{3}{4} + 4\left[\frac{\tanh^{-1}\beta}{\beta} - 1\right] \times \\ &\times \left[\frac{E_m - E}{3E} - \frac{3}{2} + \ln\frac{2(E_m - E)}{m_e}\right] + \frac{4}{\beta} L\left(\frac{2\beta}{1+\beta}\right) \\ &+ \frac{1}{\beta}\tanh^{-1}\beta\left[2(1+\beta^2) + \frac{(E_m - E)^2}{6E^2} - 4\tanh^{-1}\beta\right], \end{aligned} \tag{85}$$

where $L(x)$ is the Spence function:

$$L(x) = \int_0^x \frac{dt}{t}\ln(1-t), \tag{86}$$

where E, E_m, and β is the energy, the maximum energy, and velocity of the electron, respectively.

The contribution of strong interactions dependent radiative corrections can be written as [95, 98]

$$\Delta^{str}_{O(\alpha)} = \frac{\alpha}{2\pi}\left[4\ln(m_Z/m_p) + \ln(m_p M/M_A) + 2C + A_g\right], \tag{87}$$

where the $4\ln(m_Z/m_p)$ term represents the dominant model-independent short-distance contribution , whereas $\ln(m_p/M_A) + 2C$ are axial-current induced contributions. $M_A(\sim 1$ GeV) is a low-energy cutoff characterizing the short-distance part of the γW box diagram, while C represents the long-distance correction. Numerically, the contributions of the short-distance and long-distance parts are comparable, each contributing about 0.001 (see, e.g. ref.[99]). Finally, A_g is a perturbative QCD correction, which turns out to be very small.

It should be noted that in the first order of approximation of the standard approach for calculations of radiative corrections, one cannot obtain experimental restriction on the strong interaction dependent parts of radiative corrections from neutron decay experimental data,and, it is impossible to obtain the non-renormalized parameter λ from neutron decay experimental data [100]. These results have been obtained in the first order of the approximation. In the next order, when measuring neutron decay process with higher accuracy, it is possible to separate contributions from vector and axial-vector corrections and even to obtain restrictions on their values. Unfortunately, this approach does not look realistic for the current proposal because the energy dependance of hadronic structure corrections arising in the second order of approximation is extremely small – about $10^{-5} - 10^{-6}$. Another possibility to restrict the model-dependent parts of the corrections related to the comparison of precise experimental data of neutron decay experiments with elementary processes which are dominated by Fermi transitions (for example, π-meson decay) and Gamow-Teller transitions (neutrino deuteron reactions). Unfortunately, for both cases the accuracy must be better than the one currently available.

Therefore one should be careful in application of calculations of the hadronic model dependent parts of radiative corrections both for vector and axial-vector currents. The corrections for vector coupling constant are necessary for obtaining the CKM matrix element and for search for the possible manifestations of new physics. The axial-vector corrections became important for study neutrino nuclear interactions. The knowledge of the parameter λ with very good accuracy is in high demand from neutrino astrophysics. For example, the analysis of recent results from SNO experiment[101] needs precise calculations[102, 103, 104] of neutrino deuteron cross sections which are dominated by Gamow-Teller transitions.

There is another theoretical approach with the possibility of avoiding hadronic model dependent contributions which are present in the conventional QCD based approach. It is related to applications of the effective field theory (EFT), where the unknown high energy behavior can be integrated out and replaced by the set of low energy constants in the effective Lagrangian. The payment for this is a number of unknown parameters (counter terms) that can be extracted from a set of independent experiments. The first result of calculations of the radiative corrections for neutron decay using EFT is presented in the paper [105]. The differential neutron decay rate including recoil effects is found to be:

$$\begin{aligned}\frac{d\Gamma}{dE_e d\Omega_{\hat{p}_e} d\Omega_{\hat{p}_\nu}} &= \frac{(G_F V_{ud})^2}{(2\pi)^5}|\vec{p}_e|E_e(E_e^{max}-E_e)^2 \\ &\times\left\{C_0(E_e)+\frac{\vec{p}_e\cdot\vec{p}_\nu}{E_eE_\nu}C_1(E_e)+\left[\left(\frac{\vec{p}_e\cdot\vec{p}_\nu}{E_eE_\nu}\right)^2-\frac{\beta^2}{3}\right]C_2(E_e)\right. \\ &\left.+\frac{\hat{n}\cdot\vec{p}_e}{E_e}C_3(E_e)+\frac{\hat{n}\cdot\vec{p}_e}{E_e}\frac{\vec{p}_e\cdot\vec{p}_\nu}{E_eE_\nu}C_4(E_e)+\frac{\hat{n}\cdot\vec{p}_\nu}{E_\nu}C_5(E_e)+\frac{\hat{n}\cdot\vec{p}_\nu}{E_\nu}\frac{\vec{p}_e\cdot\vec{p}_\nu}{E_eE_\nu}C_6(E_e)\right\}, \qquad (88)\end{aligned}$$

where the angular correlation coefficients are:

$$
\begin{aligned}
C_0(E_e) &= (1+3\lambda^2)\left(1+\frac{\alpha}{2\pi}\delta_\alpha^{(Coul)}+\frac{\alpha}{2\pi}\delta_\alpha^{(1)}+\frac{\alpha}{2\pi}\;e_V^R\right) \\
&\quad -\frac{2}{m_N}\left[\lambda(\mu_V+\lambda)\frac{m_e^2}{E_e}+\lambda(\mu_V+\lambda)E_e^{max}-(1+2\lambda\mu_V+5\lambda^2)E_e\right], \qquad (89)\\
C_1(E_e) &= (1-\lambda^2)\left(1+\frac{\alpha}{2\pi}\delta_\alpha^{(Coul)}+\frac{\alpha}{2\pi}(\delta_\alpha^{(1)}+\delta_\alpha^{(2)})+\frac{\alpha}{2\pi}\;e_V^R\right) \\
&\quad +\frac{1}{m_N}\left[2\lambda(\mu_V+\lambda)E_e^{max}-4\lambda(\mu_V+3\lambda)E_e\right], \qquad (90)\\
C_2(E_e) &= -\frac{3}{m_N}(1-\lambda^2)E_e, \qquad (91)\\
C_3(E_e) &= (-2\lambda^2+2\lambda)\left(1+\frac{\alpha}{2\pi}\delta_\alpha^{(Coul)}+\frac{\alpha}{2\pi}(\delta_\alpha^{(1)}+\delta_\alpha^{(2)})+\frac{\alpha}{2\pi}\;e_V^R\right) \\
&\quad +\frac{1}{m_N}\left[(\mu_V+\lambda)(\lambda-1)E_e^{max}+(-3\lambda\mu_V+\mu_V-5\lambda^2+7\lambda)E_e\right], \qquad (92)\\
C_4(E_e) &= \frac{1}{m_N}(\mu_V+5\lambda)(\lambda-1)E_e, \qquad (93)\\
C_5(E_e) &= (2\lambda^2+2\lambda)\left(1+\frac{\alpha}{2\pi}\delta_\alpha^{(Coul)}+\frac{\alpha}{2\pi}\delta_\alpha^{(1)}+\frac{\alpha}{2\pi}\;e_V^R\right) \\
&\quad +\frac{1}{m_N}\left[-(\mu_V+\lambda)(\lambda+1)\frac{m_e^2}{E_e}-2\lambda(\mu_V+\lambda)E_e^{max}\right.\\
&\quad \left.+(3\mu_V\lambda+\mu_V+7\lambda^2+5\lambda)E_e\right], \qquad (94)\\
C_6(E_e) &= \frac{1}{m_N}\left[(\mu_V+\lambda)(\lambda+1)E_e^{max}-(\mu_V+7\lambda)(\lambda+1)E_e\right]\;. \qquad (95)
\end{aligned}
$$

Here e_V^R is the finite LEC corresponds to the "inner" radiative corrections due to the strong interactions in the standard QCD approach. $\delta_\alpha^{(Coul)} = 2\pi^2/\beta$ is the Coulomb correction to be absorbed into the standard Fermi function, $F(Z,E_e)\simeq 1+\alpha\pi/\beta$, and the functions $\delta_\alpha^{(1)}$ and $\delta_\alpha^{(2)}$ are:

$$
\begin{aligned}
\delta_\alpha^{(1)} &= \frac{1}{2}+\frac{1+\beta^2}{\beta}\ln\left(\frac{1+\beta}{1-\beta}\right)-\frac{1}{\beta}\ln^2\left(\frac{1+\beta}{1-\beta}\right)+\frac{4}{\beta}L\left(\frac{2\beta}{1+\beta}\right) \\
&\quad +4\left[\frac{1}{2\beta}\ln\left(\frac{1+\beta}{1-\beta}\right)-1\right]\left[\ln\left(\frac{2(E_e^{max}-E_e)}{m_e}\right)+\frac{1}{3}\left(\frac{E_e^{max}-E_e}{E_e}\right)-\frac{3}{2}\right] \\
&\quad +\left(\frac{E_e^{max}-E_e}{E_e}\right)^2\frac{1}{12\beta}\ln\left(\frac{1+\beta}{1-\beta}\right)\;. \qquad (96)\\
\delta_\alpha^{(2)} &= \frac{1-\beta^2}{\beta}\ln\left(\frac{1+\beta}{1-\beta}\right)+\left(\frac{E_e^{max}-E_e}{E_e}\right)\frac{4(1-\beta^2)}{3\beta^2}\left[\frac{1}{2\beta}\ln\left(\frac{1+\beta}{1-\beta}\right)-1\right] \\
&\quad +\left(\frac{E_e^{max}-E_e}{E_e}\right)^2\frac{1}{6\beta^2}\left[\frac{1-\beta^2}{2\beta}\ln\left(\frac{1+\beta}{1-\beta}\right)-1\right]\;. \qquad (97)
\end{aligned}
$$

In Eq.(88) the custom of expanding the nucleon recoil correction of the three-body phase space has been used. These corrections are included in the coefficients C_i, $i=1,\cdots,6$ defined in the partial decay rate expression, Eq.(88). It should be noted that the expression for C_2 is an exclusive three-body phase space recoil correction, whereas all other C_i, $i=1,3,\cdots,6$ contain a mixture of regular and phase space ($1/m_N$) corrections. The C_4 and C_6 corrections coefficients do not contain any Coulomb (radiative correction) terms due to our assumption that the α and the Q/m_N corrections are of the same order.

B Previous Work

B.1 History of Polarized Correlation Coefficient (A and B) Measurements

The first experiment in polarized neutron decay which achieved better than $\sim$ 20% accuracy was performed by Burgy *et al.* [106] at Argonne using a polarized thermal neutron beam from a reactor. Later experiments at Argonne followed [107, 108, 109]. Here we will concentrate on their measurements of A and B. The beam was polarized to about 80% by reflection from a magnetized mirror and was measured by reflection from a magnetized mirror analyzer. Although the mirror reflection of the thermal beam eliminated line-of-sight to the fast neutrons and gammas from the reactor core, the low count rate ($\sim$ 0.1 Hz) and the high background conditions close to the reactor were substantial, so the experimenters chose to use electron-proton coincidence to reduce backgrounds. As is common today, the neutron beam was polarized transverse to its momentum. The decay region was viewed along the neutron polarization axis by a plastic scintillator for the electrons and an electron multiplier system to gather secondary electrons from a silver-magnesium cathode for the protons. High voltage grids just outside of the beam accelerated the protons. Alternatively, or the proton detector was held at high voltage. To reduce the need for knowledge of the detector acceptances, the direction of the neutron polarization was flipped periodically so that the correlation coefficients could be determined by ratios of detector rates. This is an extremely important point, for although it is conceptually simpler to think of these asymmetry experiments as being based on the determination of rates in opposite detectors, Burgy *et. al.* realized that a much preferred way to measure the correlation is to use one detector and flip the spin. (We note, that this is the philosophy in most modern experiments. Even those that have two (opposite) detectors rely upon a spin flip to insure that they are relatively insensitive to differences in detector efficiencies. A relatively fast spin flip is particularly desirable to minimize systematic effects due to possible efficiency and/or gain drifts). In the measurement of the B coefficient, the high voltage grids were removed and the difference in the energy spectra of the recoil protons emitted opposite to the electron detector upon neutron spin reversal was measured. The detection of the (faster) electron provided the start signal. All neutrino emission angles were accepted by the spectrometer. A was measured by comparing the rates in the electron detector for opposite directions of the neutron spin. The need to use coincidence detection to suppress the background introduced possible systematic effects in the A measurement due to the nonzero B coefficient, which causes a spin-correlated change in the energy and angular distributions of the protons. The Argonne group used Monte Carlo simulations to correct for this effect.

Measurements of similar accuracy for A and B were performed in the same period at the Kurchatov Institute by Erozolimsky *et al.* [110, 111]. A polarized ($\sim$ 80%) neutron beam was obtained by placing a magnetized Co mirror close to the reactor core in a vertical channel. The polarization was measured by using the Stern-Gerlach effect to spatially separate the two spin components with a magnetic field gradient. As with the Argonne experiments backgrounds were reduced by using electron-proton coincidence, grids could accelerate the protons, and the count rate was comparable, but in this case a pair of opposed electron scintillator detectors and an orthogonal pair of opposed proton detectors (using secondary electrons generated in a CsI film) were used. The B coefficient was determined by measurement of the proton energy spectrum, as in the Argonne experiment. However, the Kurchatov group detected protons emitted normal to the electron detector axis and used an appropriately-arranged electrostatic field to restrict the phase space of the neutrino emission angles. The average cosine of the anti-neutrino emission direction was determined by Monte Carlo. For measurement of the A coefficient, an approach similar to the Argonne experiment was used with the improvement that the proton detector possessed an efficiency as close to unity as possible, through the use of electrostatic focusing grids. These same general methods were further refined by Erozolimsky *et al.* [112].

All of these measurements suffered from low counting rates, high backgrounds, ill-defined spectrometer acceptances, and challenging absolute polarization measurements. In the 1980's developments in neutron optics and superconducting magnets made possible new strategies for neutron beta decay measurements. Of critical importance at this time was the availability of neutron beams from cryogenic moderators at high flux reactors. Particularly notable was the facility at the Institut Laue Langevin, Grenoble. With the development of neutron guides for cold neutron beams, it was possible to locate the experimental apparatus ~ 100 m away from the reactor and to bend a relatively large neutron beam out of line-of-sight of the reactor, resulting in substantially reduced backgrounds, increased neutron beam intensity, and a well-defined phase space. Supermirror polarizers with high polarization (95–99%) across the entire beam phase space made neutron polarization measurement easier. These capabilities led to a new strategy for measuring A in which coincidence detection is sacrificed in exchange for relatively high-rate 4π detection of the electrons in a magnetic spectrometer. This was the basis of the original PERKEO experiment [22, 114, 115, 116]. The spectrometer consisted of a 2 m decay region immersed in a 1.6 T magnetic field coaxial with the (longitudinally polarized) neutron beam. Electrons from neutron decay were detected with essentially unit efficiency by magnetically deflecting the electrons out of the neutron beam and onto a pair of scintillator detectors outside the beam. Backscattered electrons from one detector were redirected onto the other detector. This decreased systematic effects due to backscattering and allowed for higher precision in electron spectroscopy by the addition of the energy deposition in both detectors. The first detector hit (obviously essential information for reconstructing the asymmetry) was determined by the relative timing of the signals in the fast scintillators. Careful collimation of the neutron beam using ^{6}Li-rich materials reduced gamma backgrounds.

The inhomogeneous magnetic field (required to limit the transit time of electrons in the spectrometer and reduce effects such as scattering from residual vacuum gas and synchrotron radiation that could modify the electron energy spectrum) had the disadvantage of repelling some electrons by the magnetic mirror effect into the *wrong* electron detector. A relatively large correction to the measured asymmetry had to be made for this mirror effect. Nevertheless, enough statistics were available to see for the first time in neutron decay the electron velocity dependence of the decay asymmetry and to detect the electron energy spectrum down to ~ 50 keV. Improvements in the neutron polarizers and analyzers using supermirrors allowed the neutron polarization measurement to be performed with higher accuracy.

In parallel with this effort, neutron beta decay asymmetries of comparable accuracy were performed at the Petersburg Institute of Nuclear Physics on a vertical polarized cold neutron guide that viewed a cold source in the center of a reactor core [117]. As in the group's previous work, coincidence detection was used. Knowledge of the spectrometer acceptance was significantly improved at the same time as the coincidence count rate was improved to ~ 3.5 Hz with ~ 1 Hz of background. The spectrometer design was chosen to minimize the dependence of the proton detection efficiency on the effects of the B coefficient on the proton energy and angular spectrum. The neutron polarization was measured by magnetic mirror reflection and calibrated by a Stern-Gerlach polarimeter. (Later the A coefficient result from this experiment was revised after a correction associated with the average value of the beam polarization over the neutron spectrum was taken into account [118]).

In the 1990's there were renewed attempts to improve the precision of neutron decay asymmetry measurements. One particularly interesting experiment tried a new method in which the polarized cold neutron beam was introduced into a 93% ^{4}He, 7% CO_2-filled drift chamber operated as a time projection chamber [119, 120]. In this experiment the tracks of the decay electrons were measured in the TPC and the electron energy in backing scintillators. The neutron beam was transversely polarized with a supermirror polarizer and was measured with a supermirror polarization analyzer and a spin flipper. The $\sim$ 10% background signal was dominated by gammas from the supermirror polarizer which scattered from the TPC gas into the electron detectors. The average value of the angle between the neutron spin and the direction of electron emission was determined by Monte Carlo simulations (the spatial resolution of the TPC was insufficient to be used for this purpose) and took into account effects such as the multiple scattering of the electrons in the gas etc. The fiducial volume of the decay region was determined by placing appropriate cuts on the spatial information from the TPC. This experiment was also able to see the electron velocity dependence of the asymmetry.

The next generation of the PERKEO program, PERKEO II, has been used in a series of measurements of ever-increasing precision and now reports the single most precise value of A [28, 17]. PERKEO II keeps the basic idea of the use of a 4π magnetic spectrometer. However, the size of the magnetic mirror correction in the experiment has been reduced by orienting the guiding magnetic field to be transverse to the neutron beam with a slowly decreasing magnitude, so that the size of the magnetic field gradients were reduced significantly. The plastic scintillators used for electron detection were located much farther from the beam to reduce backgrounds, but still the backgrounds were $\sim$ 10% of the signal in the lower energy part of the electron spectrum. The most recent published result from the PerkeoII collaboration, the most precise measurement of A to date, is $A = -0.1189 \pm 0.0007$.

The B coefficient has also been recently measured with significantly higher precision, first at PNPI [121] and then with improved accuracy with the same apparatus at the ILL [18]. An experimental setup similar to that used for the PNPI A correlation coefficient was used with electron-proton coincidence. Also recently a new measurement of the B coefficient has been performed using the Perkeo II apparatus [19].

Finally a different approach to the determination of λ was pursued which has the attractive feature that it is insensitive to the absolute value of the neutron polarization, which is one of the great challenges of the A and B asymmetry measurements. In this approach one effectively measures using the same apparatus the products P_nA and P_nB where P_n is the neutron polarization. Then combination of the results allows one to determine $\lambda = (A-B)/(A+B)$ without an absolute neutron polarization measurement [122].

B.2 History of a measurements

The first measurement of a in neutron decay by Grigoriev *et al.* [123] was performed at the Institute of Theoretical and Experimental Physics. Unlike the A and B coefficients, a does not require polarized neutrons but does require the measurement of either the protons energy distribution, which is very difficult given the low proton energies, or the proton direction, in order to reconstruct the neutrino direction and the neutrino momentum-electron momentum correlation. Coincidence counting was employed for background suppression. A double magnetic spectrometer was used for the energy spectrum of the decay electrons. The recoil proton energies were determined in a detector opposite the electron detector using the time-of-flight distribution from the decay region to an accelerating gap for detection by secondary electron emission. An ellipsoidal electrostatic mirror was used to increase the phase space acceptance for the protons without disturbing the energy spectrum. Triple coincidences among the proton detector, the electron detector, and a thin ΔE detector in the focus of the double magnetic spectrometer reduced backgrounds. Even with these means the ITEP experiment could only verify that a was nonzero and negative at the 2σ level.

The next measurement of a was performed in a fascinating experiment that used as a sample protons from neutron decays in a "through" hole in a small reactor [124, 16]. The high density of free neutrons in the reactor core provided a very high count rate. The protons emerging from the "through" hole were energy analyzed in an spherical electrostatic field. From this careful measurement of the proton energy spectrum, the slight shift in the shape of the proton spectrum due to $a \neq 0$ was determined. Ths led to a determination of a to about 5%.

Recently a has been measured again with comparable accuracy using the integrated proton energy spectrum as measured with a variable mirror potential in a Penning trap [125, 126, 15] . The use of the Penning trap allows 4π detection of the protons and the elimination of end effects through electrostatic variation of the size of the trap along the neutron beam. The protons move adiabatically in a magnetic field from the high-field region in which they decay to a low field region where they are detected. The sensitivity of this very sraightforward approach was limited by the fact that the method, in effect, measures only the energy associated with the axial component of the proton momentum. This experiment achieved a comparable sensitivity to a.

B.3 Experiments in Progress

There are several experiments ongoing or planned to measure A and a with a higher precision.

Since their last publication [17], Perkeo II collaboration have implemented some upgrades, including a new ballistic supermirror guide for a higher neutron flux [127] and a new crossed supermirror polarizers for a higher neutron polarization [24]. At the same time, a new experiment Perkeo III has been developed.

The UCNA experiment [29], currently being commissioned at Los Alamos National Laboratory, aims at a 0.2% measurement of A using ultracold neutrons (UCNs).

There are also efforts to improve the precision of a. The aCORN experiment, being prepared at NIST, aims to determine a to a statistical precision of 1% or less by performing coincidence detection of electrons and recoil protons and selecting two kinematic regions such that a comparison of the rates in the two regions directly yields a measurement of a [128]. The aSPECT experiment, currently being commissioned at Mainz, will measure the recoil proton energy spectrum using a magnetic spectrometer with electrostatic retardation potentials [129]. The expected precision is $\delta a/a = 0.25\%$.

Below we describe the UCNA experiment more in detail, which has a significantly different approaches, and therefore has significantly different systematic effects from previous experiments and the experiment proposed here. The UCNA experiment [29] plans to detect decay electrons from a sample of ultra-cold neutrons trapped in the spectrometer rather than from a cold neutron beam that traverses the detector. This novel technique is claimed to have two distinct advantages over previous methods:

1. Because the kinetic energy of UCN is less that to the magnetic dipole energy $\vec{\mu} \cdot \vec{B}$ for $B \sim$few

Telsa, it is, in principle, possible to totally reflect one neutron spin from a region of sufficiently different magnetic field. The neutrons which are not reflected can be of only one spin state and are thus 100% polarized. The UCNA experiment proposes to exploit this and thus avoid the necessity of a precision determination of the neutron polarization.

2. Because each neutron remains within the detector on the order of 10 s the relative probability of capture as opposed to decay is significantly less than for a cold neutron experiment where the time is typically < 1 ms. Since the dominant source of background is due to neutron capture, it is anticipated that the S/N for singles detection will be significantly more in the UCN experiment.

In addition the experiment will exploit a new technique for the production of UCN that, it is hoped, will produce significantly higher UCN densities than available at the best (and only) currently operating UCN source at the ILL.

The UCNA experiment offers the prospect of a significant improvement in our knowledge of A, in an apparatus that is subject to a set of systematic effect that is quite different than those in previous experiments. While it is beyond the scope of this proposal to evaluate the prospects for this promising new experiment, it is appropriate to make observe that UCNA faces a number of significant technical challenges. Perhaps most notable are:

- While very promising, to date, the novel UCN source technology has only been demonstrated in limited proof of principle tests. It has yet to provide UCN in a realistic experimental setting and to demonstrate the reliability required for a precision measurement such as UCNA.

- While the physics behind the hypothesis of 100% polarization is beyond dispute, there are details in it's realization require experimental confirmation. The neutrons interact with magnetic filed variations and with material walls. While the depolarization associated with these processes are small, they must be measured. The UCNA collaboration clearly understands this and has indeed measured this small depolarization [130] . However, a convincing, high accuracy measurement of A will likely require an *in situ* determination of the depolarization associated with the actual decay apparatus.

- The magnetic field in the decay volume of the UCNA experiment is inhomogeneous and created a magnetic mirror for decay electrons from decays at the ends of the apparatus. While this effect is expected to be small and is, in principal capable of being modeled, it will be difficult to directly measure. As noted earlier, it was just such an effect that led to the redesign of the original PERKEO experiment so as to insure that the magnetic field in the decay volume is uniform.

- Finally, in UCNA the "fill-time" as well as the "hold-time" of the "bottle" are expected to be ≥ 10 s. This implies that spin reversal modulation can only be performed with a period of 1 minute or more. Such a relatively slow modulation will require a high level of stability in the spectrometer. To minimize sensitivity to detector drifts, Previous experiments have opted for the fastest possible spin flip modulation, typically ~ 1 s. No previous experiment has depended on such a slow modulation.

Notwithstanding these challenges we look forward to a precise measurement of A by a technique that is significantly different than other measurements and is therefore subject to a quite different set of systematic effects. The physics at stake is sufficiently important that a set of complimentary experiments is extremely important.

C Managment Plan

The task of the abBA collaboration is to secure scientific approval and funding for the abBA experiment at the SNS and to subsequently design, construct and commission the system and to complete the physics program leading to the publication of the final results.

In order to achieve this task we envision a managment structure as outlined in Figure 40 and described in more detail below.

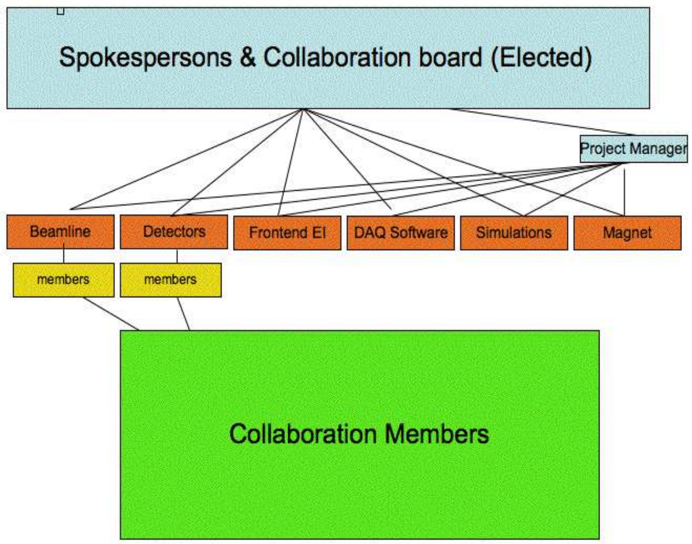

Figure 40: The abBA managment structure.

C.1 Spokespersons and Collaboration Board

The collaboration board (CB) will consists of spokespersons, elected members from the collaboration and the project manager. Each member of the CB has one vote and the elected members will serve for two year terms, with no more that two terms served consecutively. No more than one representative from one instituion can be elected to the CB simultaneously. In the construction phase the CB has overall responsibility for a timely devlivery of all the different components. In order to facilitate this, we forsee the position of a project manager (PM). The PM will be responsible for monitoring the progress of the construction, for following the financial committments and coordinating the different working groups especially during the time of installation. The PM is also a member of the collaboration board. The PM will also collect the Memorandum of Understandings (MOU), serve as the secretary of the CB and take notes of the CB meetings.

C.2 The Technical Working Groups

We plan to establish working groups, with each of them being responsible for part of the hardware and software ncessary for the experiment. Each of them will have a working group leader / work package manager, who will directly report to the CB and PM. These leadres will be selected from within the collaboration. Initially we plan to have six such groups:

1. Beamline group; responsible for all aspects of the neutron transport: i.e. polarizer, analyzer, spin-flipper, shielding ...
2. Detectors: Responsible for detector R&D, mounting hardware, preamps.
3. Frontend Electronics: Digitizers cabling issues, readout electronics
4. DAQ: This group will cover readout software and analysis code, esatblish criteria for computer requirements.
5. Simulations: Developing a realistic Monte Carlo simulation of the whole experiment.
6. Magnet: Responsible for the magnet and electric field design and fabrication.

It is immediately clear from the list that there is a lot of overlap between the different groups; for instance the development of a DAQ readout system has to be closely coordinated with the Frontend electronics group. We envision that people will be members of different groups thus enabling communication between the groups. In order to ensure a seamless integration of the different projects the PM together wih the CB will be of crucial importance.

C.3 The Collaboration Members

The abBA collaboration membership consists of scientists who have signed a Memorandum of Understanding (MOU) specifying the expected contributions within the scientific and/or technical objectives of the abBA collaboration. Such contributions may be defined as any component of hardware, software, or any aspect related to the scientific basis of the experiment, and which the collaboration deems important to the persuit of its objectives.

D Budget

Item	Unburdened Cost	Comments
beamline	**37,400**	
detectors	**221,400**	
detector electronics	**454,360**	
polarizer	**148000**	
spin flipper	**60500**	
guide field	**24,700**	
beam monitors	**10,000**	
neutron shielding	**41,000**	
electrostatic structure	**30,000**	
Subtotal	**1,595,860**	
TOTAL	**2,074,618**	30 % contingency

Table 6: An itemized summary of the experimental budget.

E Schedule

In Fig 41 we have outlined the schedule for this experiment. We foresee a R&D phase of two years. During this time we will finish the development work for the Silicon detectors in close collaboration with Micron,LTD in the UK. Furthermore, the final evaluation of the frontend electronics will happen and a decision on the DAQ hardware will be made, based on price and performance. We will also start the development of the analyzer/offline software in conjunction with a Monte Carlo simulation of the experiment. Once the Frontend hardware has been selected work on the DAQ readoutsystem will begin. During the R&D phase we will also design the polarizer, analyzer and spin flipper as well as the additional beam line components needed like monitors and shielding. We forsee that we will start with the procurement of the necessary equipment in 2009, so that we could begin with construction in late 2009. We estimate that the setup of the whole experiment will take a year, followed by a commissioning period during 2011. This will be followed by a two year data run starting in fall of 2011.

Figure 41: The proposed schedule for the abBA experiment

F Required Resources and Facility Interface

As discussed in Section 4.1, approximately 5000 hours of production running is required to achieve the statistical goal of the experiment, assuming 90% availability for the accelerator, and 90% operation of the experiment. In addition, substantial time will be required for commissioning the experiment and performing calibrations and systematic tests. At present, we do not have a detailed plan for these activities, but a full run cycle is a rough estimate of the time required. We are therefore requesting use of the FnPB for two consecutive run cycles of 5000 hours. An additional run cycle may be required for completion of data taking, depending upon operational efficiencies and actual counting rates. Allocation of non-consecutive blocks of beam time will also allow the experiment to achieve its goals, but at the cost of delaying the results and requiring additional time to change between experiments. Subject to timely funding and availability of the spectrometer magnet, the experiment will be ready to occupy the beam line in 2010.

In addition, we request the following resources be provided by the FNPB.

- Operation of the spectrometer magnet.
- Electrical power, both regular and isolated ground (requirements are not yet known, but less than NPDGamma).
- Cooling water, 4 gal/min.
- Neutron shielding, especially around the polarizer and neutron windows, as required to meet facility requirements.

The experiment will introduce some hazards into the facility.

- Class 4 lasers, operated in embedded class 1 mode.
- Electrical hazards, including high voltage for the electrodes and detectors.
- Chemical hazards, including standard solvents and small amounts of rubidium.
- Radiological hazards, including beam-activated components and radioactive sources.
- Powerfull magnetic fields.
- Cryogenic hazards and cold surfaces.

References

[1] P. Herczeg, Prog. Part. Nucl. Phys. 46, 413 (2001).

[2] A. Sirlin, Rev. Mod. Phys. 50, 573 (1978).

[3] J. D. Jackson, S. B. Treiman and H. W. Wyld, Jr.,Phys. Rev. **106**, 517 (1957).

[4] F. Liu, Int.J.Mod.Phys.A20,3600 (2005).

[5] B. G. Yerozolimsky, NIM A440, 491 (2000).

[6] Review of Particle Physics, J. Physics G 33, 1 (2006)

[7] M.J. Ramsey-Musolf, Phys. Rev. D **62**, 056009 (2000).

[8] A. Kurylov and M.J. Ramsey-Musolf, Phys. Rev. Lett. **88**, 071804 (2002).

[9] J. Erler, A. Kurylov, and M. J. Ramsey-Musolf, Phys.Rev. D **68**, 016006 (2003).

[10] M.J. Ramsey-Musolf and S. Su, hep-ph/0612057 (2006).

[11] V. Gudkov, G. L. Greene and J. R. Calarco, Phys. Rev. C **73**, 035501 (2006).

[12] I. S. Towner and J. C. Hardy, nucl-th/9809087 (1998); Physics Beyond the Standard Model, Proc. of 5th Int. WEIN Symposium, Eds. P. Herczeg, C. M. Hoffman and H. V. Kalapdor-Kleingrothaus, (World Scientific, 1999), p.338.

[13] J.Deutsch and P.Quin, *in Precision tests of the standard electroweak model*, ed. P. Langacker, (World Scientific, 1995) p.706.

[14] D. Pocanic, Proceedings of 2nd Workshop on the CKM Unitarity Triangle, Durham, England, 5-9 Apr 2003, p. WG606.

[15] G. Byrne *et al.*, J. Phys. G **28**, 1325 (2002).

[16] C. Stratowa, R. Dobrozemsky, P. Weinzierl, Phys. Rev. D **18**, 3970 (1978).

[17] H. Abele *et al.*, Phys. Rev. Lett. **88**, 211801 (2002).

[18] A. P. Serebrov *et al.*, JETP **86** 1074 (1998).

[19] M. Schumann, *et al.*, `0706.3788 [hep-ph]` (2007).

[20] P. Liaud *et al.*, Nucl. Phys. A **612**, 53 (1997).

[21] B. Yerozolimsky *et al.*, Phys. Lett. B **412**, 240 (1997).

[22] P. Bopp, *et al.*, Phys. Rev. Lett. **56**, 919 (1986).

[23] F. Mezei, Commun. Phys. **1**, 81 (1976).

[24] M. Kreuz, *et al.*, Nucl. Instrum. Methods Phys. Res. A **547** 583 (2005).

[25] A. P. Serebrov *et al.*, Nucl. Instrum. Methods Phys. Res. A **357**, 503 (1995).

[26] O. Zimmer *et al.*, Phys. Lett. B **455**, 62 (1999).

[27] B. G. Erozolimskii, *et al.*, Phys. Lett. B **263**, 33 (1991).

[28] H. Abele *et al.*, Phys. Lett. B **407**, 212 (1997).

[29] R. Carr *et al.* (UCNA Collaboration), A proposal for an accurate measurement of the neutron spin-electron angular correlation in polarized neutron beta-decay with ultracold neutrons, 2000.

[30] R. Alarcon, private communication.

[31] S. Baeβler, private communication (2007)

[32] R. Dobrozemsky, NIM 118, 1 (1974)

[33] E. Frlež, private communication.

[34] Micron Semiconductors Ltd., Lancing, Sussex, UK.

[35] J.S. Nico *et al.*, PRC 71, 055502 (2005).

[36] R.Grzywacz *et al.*, Nucl. Instrum. Methods **B** (2003) in press

[37] B. Hubbard-Nelson *et al.*, Nucl. Instrum. Methods **A422**, 411 (1999) and *http://www.xia.com.*

[38] M. Pfützner *et al.*, Eur. Phys. J. **A 14**,(2002) 279

[39] K. Miernik *et al.*, Phys. Rev. Lett. in press,

[40] M. Karny *et al.* Phys. Rev. Lett. **90**,(2003) 012502

[41] K.P. Rykaczewski *et al.*, AIP Conf. Proc. **638**,(2002) p. 149

[42] S. Liddick *et al.*, Phys. Rev. Lett. 97 (2006) 082501,

[43] A. Fallu-Labruyere at al. Nucl. Instrum. Methods **A579** (2007) 247

[44] P.-N. Seo *et al.*, NIM A 517, 285 (2004).

[45] T.E. Chupp *et al.*,"A large area polarized 3He neutron spin filter",Nucl. Instrum. Methods in Physics Research A574, 500 (2007).

[46] C. B. Crawford, R. Mahurin, unpublished technical note, "Opening angles for the SNS FnPB choppers", 2006-11-30. http://sns.phys.utk.edu/svn/npdg/trunk/simulations/sns/choppers/tex/choppers.pdf

[47] C. B. Crawford, technical note, to appear soon: "Opening angles for the SNS FnPB choppers", 2007-11, http://sns.phys.utk.edu/svn/npdg/trunk/simulations/sns/choppers/tex/abba_sim.pdf

[48] D. R. Rich *et al.*, Nucl. Instrum. Methods **A 481**,431 (2002).

[49] T. E. Chupp *et al.*, Nucl. Instrum. Methods **A 574**, 500 (2007).

[50] T. R. Gentile, W. C. Chen, G. L. Jones, E. Babcock, and T. G. Walker, J. Res. Natl. Inst. Stand. Technol. **110**, 299 (2005).

[51] P. Böni, private communication (2007).

[52] C. Keith *et al.*, *Phys. Rev.* C **69** 034005 (2004).

[53] S. F.Mughabghab, M. Divadeenam, and N.E. Holden, *"Neutron Resonance Parameters and Thermal Neutron Cross Sections"*, vol 1, of Neutron Cross Sections, Academic Press, New York (1981).

[54] J. Als-Nielsen and O. Dietrich, Phys. Rev. **133**, B925 (1964).

[55] R.E. Jacob, S.W. Morgan, B. Saam, and J.C. Leawoods, Phys. Rev. Lett. **87**, 143004 (2001).

[56] T. R. Gentile, private communication, 2007.

[57] M. Sharma *et al.*, Bulletin of American Phys. Soc. **52**, 41 (2007).

[58] T. E. Chupp, private communication (2007).

[59] K. Abe *et al.*, Phys. Lett. **B 452**, 194 (1999).

[60] X. Zheng *et al.*, Phys Rev. C **70**, 065207 (2004).

[61] I.C. Ruset, S. Ketel, and F.W. Hersman, Phys. Rev. Lett. **96**, 053002 (2006)

[62] K. H. Andersen *et al.*, Physica **B 356**, 103 (2005); E. Lelievre-Berna, Physica **B 397**, 162 (2007).

[63] W.C. Chen, T.R. Gentile, T.G. Walker, and E. Babcock, Phys. Rev.A **75**, 013416 (2007).

[64] E. Babcock, B. Chann, T.G. Walker, W.C. Chen, and T.R. Gentile, Phys. Rev. Lett. **96**, 083003 (2006).

[65] M. Dabaghyan, Ph.D. Thesis, 2007.

[66] B. G. Erozolimskii *et al.*, Phys. Lett. B **263**, 33 (1991).

[67] P.-N. Seo *et al.*, submitted to Phys. Rev. STAB (2007); arXiv:0710.2871v1 [nucl-ex].

[68] S.I. Penttila and J. D. Bowman, *J. Res. Natl. Inst. Stand. Technol.* **110**, 309 (2005).

[69] S. V. Grigoriev, A. I. Okorokov, and V. V. Runov, Nucl. Instrum. Methods A **384**, 451 (1997).

[70] S. V. Grigoriev *et al.*, Phys. Rev. **A64**, 013614 (2001).

[71] W. H. Kraan *et al.*, Nucl. Instrum. Methods A **510**, 334 (2003).

[72] S. Agostinelli et al.,Nucl. Instrum. Methods A 506 (2003) 250-303; J. Allison et al., IEEE Trans. Nucl. Sc. 53 No. 1 (2006) 270-278; www.cern.ch/geant4

[73] D. A. Dahl, Int. J. Mass Spectrom. 200 (2000) 3; www.simion.com

[74] www.vectorfields.com

[75] Rene Brun and Fons Rademakers, Proceedings AIHENP'96 Workshop, Lausanne, Sep. 1996;Nucl. Instrum. Methods in Phys. Res. A 389 (1997) 81-86; root.cern.ch

[76] S. I. Penttila and J. D. Bowman, "Precision Neutron Polarimetry for Neutron Beta Decay", *J. Res. Natl. Inst. Stand. Technol.* **110**, 309 (2005).

[77] J.E. Epperson, J.M. Carpenter, P. Thiyagarajan, and B. Heuser, Nucl. Instrum. Methods **A289**, 30 (1990).

[78] http://www.nea.fr/html/pt/docs/iem/madrid00/Proceedings/Paper36.pdf.

[79] P.D. Ferguson, W.B. Wilson, F.X. Gallmeier, and E.B.Iverson, in proceedings of the 16th meeting of the International Collaboration on Advanced Neutron Sources (ICANS-XVI) edited by G. Mank and H. Conrad (Forschungzentrum Jlich GmbH, Jlich, 2003).

[80] R. Mahurin *et al.*, private communication, to be published (2008).

[81] http://physics.nist.gov/cgi-bin/Star/ap_table.pl

[82] Yung-Su Tsai, Rev Mod. Phys 46 (1974) 815

[83] M. Dabaghyan, NPDGamma Technical Note No 27 (2006).

[84] U. Fano. Phys. Rev. **72** (1947) 26.

[85] B.H. Bransden and C.J. Joachain, "Physics of Atoms and Molecules", 2nd edition, (Prentice Hall, 2003), p.738.

[86] M. H. Mendenhall and R. A. Weller, Nucl. Instrum. Methods B227, 420 (2005)

[87] J.F. Ziegler, J.M Manoyan, "The stopping of ions in compounds," Nucl. Instr. Methods B35, 215 (1988).

[88] J. Nico, personal communication.

[89] F. Glück et al, EPJA 23, 135 (2005)

[90] J. Bonn, personal communication.

[91] S. M. Bilen'kii, R. M. Ryndin, Ya. Smorodinskii and Ho Tso-Hsiu, Sov. Phys. JEPT **37**, 1241 (1960).

[92] B. R. Holstein, Rev. Mod. Phys. **46**, 789 (1974).

[93] D. H. Wilkinson, Nucl. Phys. A**377**, 474 (1982).

[94] S. Gardner and C. Zhang, Phys. Rev. Lett. 86 (2001) 5666.

[95] A. Sirlin, Phys. Rev. **164**, 1767 (1967).

[96] A. Sirlin, Rev. Mod. Phys. **50**, 573 (1978).

[97] A. García and M. Maya, Phys. Rev. D 17 (1978) 1376.

[98] W. J. Marciano and A. Sirlin, Phys. Rev. Lett. **56**, 22 (1986).

[99] I. S. Towner and J. C. Hardy, nucl-th/9809087 (1998); Physics Beyond the Standard Model, Proc.of 5th Int. WEIN Symposium, Eds. P. Herczeg, C. m. Hoffman and H.

[100] V. Gudkov, in: Proc. of IPN2003 and UKJ2003, J. of Neutron Research 13, 39 (2005).

[101] SNO Collaboration, Q. R. Ahmad et al., Phys. Rev. Lett. 87 (2001) 071301; ibid 89 (2002) 011301; ibid 89 (2002) 011302.

[102] S. Nakamura, T. Sato, V. Gudkov, K. Kubodera, Phys. Rev. C 63 (2001) 034617; S. Nakamura, T. Sato, S. Ando, T.-S. Park, F. Myhrer, V. Gudkov, K. Kubodera, Nucl. Phys. A 707 (2002) 561.

[103] M. Butler, J.-W. Chen, Nucl. Phys. A 675 (2000) 575; M. Butler, J.-W. Chen, X. Kong, Phys. Rev. C 63 (2001) 035501.

[104] S. Ando, Y. H. Song, T.-S. Park, H. W. Fearing, K. Kubodera, Phys. Lett. B 555 (2003) 49.

[105] S. Ando, H. W. Fearing, V. Gudkov, K. Kubodera, F. Myhrer, S. Nakamura and T. Sato, Phys. Lett. **B595**, 250 (2004).

[106] M. Burgy *et al.*, Phys. Rev. **120**, 1829 (1960).

[107] C. Christensen, V. Krohn, and G. Ringo, Phys. Lett. **B28**, 411 (1969).

[108] C. Christensen, V. Krohn, and G. Ringo, Phys. Rev. C **1**, 1963 (1970).

[109] V. Krohn and G. Ringo, Phys. Lett. **B55**, 175 (1975).

[110] B. Erozolimsky *et al.*, Yad. Fiz. **12**, 323 (1970).

[111] B. Erozolimsky *et al.*, Zh. Eksp. Theor. Fiz. **13**, 356 (1971).

[112] B. Erozolimsky *et al.*, Yad. Fiz. **30**, 692 (1979).

[113] P. Bopp *et al.*, Phys. Rev. Lett. **56**, 919 (1986).

[114] E. Klemt *et al.* Z. Phys. C **37** 179 (1988).

[115] J. Dohner *et al.* Nucl. Instum. Methods Phys. Res. Sect. A **284**, 123 (1989).

[116] P. Bopp *et al.*, Nucl. Instrum. Methods Phys. Res. Sect. A **267**, 436 (1988).

[117] B. G. Erozolimskii, *et al.*, Phys. Lett. B **263**, 33 (1991).

[118] B. Yerozolimsky *et al.*, Phys. Lett. B **412**, 240 (1997).

[119] P. Liaud *et al.*, Nucl. Phys. A **612**, 53 (1997).

[120] K. Schreckenbach *et al.*, Phys. Lett. **B349**,427 (1995).

[121] I. Kuznetsov *et al.*, Phys. Rev. Lett. **75**,794 (1995).

[122] I. Kuznetsov and Y. Rudnev, Nucl. Instrum. Methods Phys. Res. Sect. A **440**, 539 (2000).

[123] V. Grigoriev *et al.*, Yad. Fiz. **6**, 329 (1968).

[124] R. Dobrezemski *et al.*, Phys. Rev. D **11**, 510 (1975).

[125] J. Byrne, *Neutrons, Nuclei, and Matter* (AIP Press, Woodbury, New York, 1994).

[126] P. Dawber, Nucl. Instrum. Methods Phys. Res. Sect. A **440**, 543 (2000).

[127] H. Häse, *et al.*, Nucl. Instrum. Methods Phys. Res. A **485**, 453 (2002).

[128] F. E. Wietfeldt, *et al.*, Nucl. Instrum. Methods Phys. Res. A **545**, 181 (2005).

[129] O. Zimmer, *et al.*, Nucl. Instrum. Methods Phys. Res. A **440**, 548 (2000).

[130] A. R. Young, (private communication).